



Journal of INNOVATIVE SCIENCE and ENGINEERING

Volume 8
Issue 1
Year 2024

E-ISSN: 2602-4217

www.jise.btu.edu.tr

Mathematical Modeling of the Transmission Dynamics of Monkeypox with the Impact of Quarantine and Public Enlightenment in Nigeria

Sefiu Onitilo¹ , Abiodun Ajani¹ , Deborah Daniel^{1*} , Ayobami Haruna¹ 

¹ Olabisi Onabanjo University, Department of Mathematical Sciences, 121103, Ago-Iwoye, Nigeria

Abstract

Monkeypox remains a public health concern in Nigeria, with periodic outbreaks reported. Despite efforts to control the disease, the number of reported cases continues to rise. Understanding the transmission dynamics of monkeypox and predicting its future spread can inform public health decision-making and guide the allocation of resources for control efforts. Hence, in this study, a deterministic model for the transmission dynamics of Monkeypox in the presence of quarantine and public enlightenment is presented. The model analysis involving the Disease Free Equilibrium (DFE) is established. Numerical simulations were used to better investigate the impact of quarantine and public enlightenment on human population. The results revealed that the effectiveness of the combined form of public awareness and quarantine produced more results followed by the effectiveness of public awareness alone, and then the result achieved when infected individuals were quarantined. If the measures were implemented with a greater degree of integration, there would be a significant reduction in the viral peak, thereby preventing its persistence within the human population.

Keywords: Monkeypox, Transmission Dynamics, Modelling, Quarantine, Public Enlightenment, Reproduction Number.

Cite this paper as: Sefiu O., Abiodun A., Deborah D. and Ayobami H. (2024). Mathematical Modeling of the Transmission Dynamics of Monkeypox with the Impact of Quarantine and Public Enlightenment in Nigeria, 8(1):1-17.

*Corresponding author: Deborah Daniel
E-mail: oludeboradaniel@gmail.com

Received Date: 18/08/2023
Accepted Date: 28/12/2023
© Copyright 2024 by
Bursa Technical University. Available
online at <http://jise.btu.edu.tr/>



The works published in the journal of Innovative Science and Engineering (JISE) are licensed under a Creative Commons Attribution-NonCommercial 4.0 International License.

1. Introduction

Monkeypox is an infectious illness caused by the monkeypox virus, which may affect both people and animals. The virus was first detected in Simians in the Democratic Republic of the Congo in 1958; however, it was not until 1970 that the first instance of human infection was officially documented. Subsequent to the aforementioned period, intermittent instances of outbreaks have transpired in many African nations, encompassing Cameroon, the Central African Republic, Ivory Coast, Liberia, Nigeria, Sierra Leone, and Sudan, along with some regions within the Americas and Europe. The virus exhibits endemicity in nations located in Central and West Africa, hence warranting attention as a significant public health issue, given its propensity to incite epidemics. The etiological agent of monkeypox is classified under the genus Orthopoxvirus, which encompasses other viruses such as those accountable for smallpox and vaccinia [6, 8, 9, 11, 22]. Although monkeypox is often less severe than smallpox, it may pose a significant risk to those with compromised immune systems, potentially leading to life-threatening outcomes. Monkeypox is classified as a zoonotic ailment, denoting its potential for inter-species transmission from animals to humans. The transmission of the virus mostly occurs through wild animals, including rodents, monkeys, squirrels, and primates, either via direct contact with these animals or by contact with their bodily fluids or infected animal products. Monkeypox has a variety of clinical presentations, including symptoms such as fever, headache, muscular pains, backache, enlarged lymph nodes, chills, and exhaustion. The appearance of a dermatological eruption becomes evident, often commencing in the face area and then spreading to diverse anatomical places.

The comprehensive comprehension of the natural history of the monkeypox virus remains enigmatic, requiring more inquiry to determine the specific reservoir(s) and the processes by which viral circulation is maintained in its natural habitat. One potential risk factor that has been identified in research is the consumption of undercooked meat and other animal-derived products acquired from animals that are infected [4]. In nations where the illness is non-endemic and instances have been detected, more endeavours are being undertaken within the realm of public health. These efforts include comprehensive investigations aimed at identifying patients, tracking contacts, doing laboratory analysis, managing clinical issues, and implementing isolation measures with adequate support. Genomic sequencing has been used to determine the particular viral clade(s) of monkeypox in the ongoing epidemic, if possible. Moreover, as stated in the reference [1], control techniques for respiratory illnesses include a variety of policies, such as quarantine protocols, infection control measures, identification and isolation of cases, and vaccination interventions.

The use of mathematical modeling presents a feasible methodology for examining the intricacies of infectious diseases, such as monkeypox. Mathematical models have the capacity to forecast the propagation of diseases, assess the efficacy of various intervention approaches, and provide valuable insights into the fundamental principles of disease transmission. Numerous scholars have used mathematical models to investigate the aetiology of diseases in diverse populations, and these models have shown their efficacy and utility (Malaria [15], HIV [3], Cholera [16], COVID-19 [5, 13–14, 17–18], Monkeypox [2, 6–11, 19–23]). Gaining insight into the transmission mechanisms of monkeypox and developing projections about its future dissemination might provide valuable information for public health decision-making and facilitate the effective allocation of resources towards control measures. A variety of models using different methodologies have been developed and analysed to improve comprehension of the transmission dynamics and control tactics of monkeypox.

The authors of [7] have created a deterministic mathematical model to describe the transmission dynamics of the monkeypox virus. The model includes a component representing the imperfect vaccination efficacy within the human subpopulation. The stability of the equilibrium states of the model equation was examined and obtained. A numerical simulation was conducted to emphasise the impact of several levels of immune system strength (weak, medium, and strong) on different epidemiological states. Additionally, the simulation examined the influence of infection and vaccination rates on the prevalence of the disease and the number of vulnerable individuals, respectively. The mathematical model of monkey-pox transmission was investigated by [10] using ordinary differential equations. The validity of the model's feasible area was confirmed, demonstrating the presence of positive solutions. The mathematical model of monkeypox viral transmission dynamics, including two interacting host populations, namely humans and rats, was investigated by [23]. The implementation of quarantine measures and public awareness campaigns serves as a mechanism for managing the transmission of the illness among the human population. The authors in reference [19] put out a deterministic mathematical model with the aim of examining the dynamics of the monkeypox virus among the human population. The results indicate that implementing measures to separate individuals who are infected from the broader community may effectively mitigate the spread of diseases. The researchers in this work [20] developed and analysed a deterministic mathematical model in order to investigate the dynamics of the monkeypox virus. This study establishes the conditions for determining the asymptotic stability of both disease-free and endemic equilibria, both at the local and global levels. The findings indicate that the use of strategies to separate individuals who are infected from the wider community may be an effective approach to reducing the transmission of illnesses.

Nevertheless, a dearth of comprehension persists about the determinants that propel the transmission and dissemination of the ailment within the Nigerian context. Nigeria, being the most populous nation in Africa, has a diversified population and varied topography, both of which may have a significant influence on the transmission patterns of infectious illnesses. The existence of this information gap hinders policymakers' capacity to formulate and implement effective control and preventive initiatives. Hence, it is essential to develop a mathematical model that may provide valuable insights into the transmission dynamics of monkeypox in Nigeria and facilitate informed decision-making on disease management strategies. Therefore, this study considered the rodent-human transmission route named SIQR-SEI model. This model enhances the classic SEIR and SIR framework by incorporating vaccination, transmission through rodents, quarantine phases, and unique interaction dynamics among different population groups. The process includes vaccination of individuals, a transmission route that involves interaction with infected rodents resulting in human illness, and a quarantine phase for observed individuals before recovery.

2. Material and Methods

2.1. Mathematical Formulation

The model takes into account two distinct populations, one consisting of humans and the other consisting of rodents. The human population may be classified into four distinct categories: susceptible, infected, quarantined, and recovered. The population of rodents is classified into three distinct categories, namely, susceptible, exposed, and infected.

Table 1. State Variable of the Model and their descriptions.

Variables	Description
$S_H(t)$	Susceptible human population at time (t)
$I_H(t)$	Infected human population at time (t)
$Q_H(t)$	Quarantined human population at time (t)
$R_H(t)$	Recovered human population at time (t)
$S_R(t)$	Susceptible rodent population at time (t)
$E_R(t)$	Exposed rodent population at time (t)
$I_R(t)$	Infected rodent population at time (t)

Table 2. Model parameters with their descriptions.

Parameters	Description
μ_H	Recruitment rate of human population
μ_R	Recruitment rate of rodent population
σ_1	Contact rate of rodent population
σ_2	Contact rate of human population
σ_3	Contact rate of rodent population
Φ_H	Natural death rate of human population
γ_H	Disease induced death rate of human population
ρ_H	Recovery rate of human population
η	Progression rate from infected to quarantine
Φ_R	Natural death rate of rodents population
γ_R	Disease induced death rate of rodent population
ξ	Effectiveness of quarantine and treatment
α	Effectiveness of public enlightenment and campaign

2.2. Model Assumptions

The model's derivation is based on the following assumptions: there is an absence of emigration from the overall population, and likewise, there is a lack of immigration into the population. During a certain period, a minute fraction of people experienced migration into or out of the population and subsequently received vaccination; maturation, also known as maturity, is defined as the interval between the time of infection and the onset of observable symptoms, often occurring within a timeframe of 14 to 21 days; the susceptible population is first exposed to a type of rodent that carries the infectious agent, resulting in their subsequent infection; and certain persons who have contracted the infection are sent to a designated facility where they undergo quarantine to conduct observational procedures. The process of recruiting individuals from the S_H class to the I_H class occurs via interactions with individuals from the I_R class within the rodent population. The process of recruiting individuals from the I_H class to the Q_H class occurs at a pace denoted by the symbol η . The recruitment of individuals from the Q_H class into the R_H class is contingent upon the efficacy of the quarantine and observation protocol, denoted by the rate ρ ; the occurrence of death is inherent in the model and it transpires uniformly across all classes at a constant

rate μ . However, it is worth noting that there is an increased mortality rate seen in the I_H and Q_H classes as a result of infection.

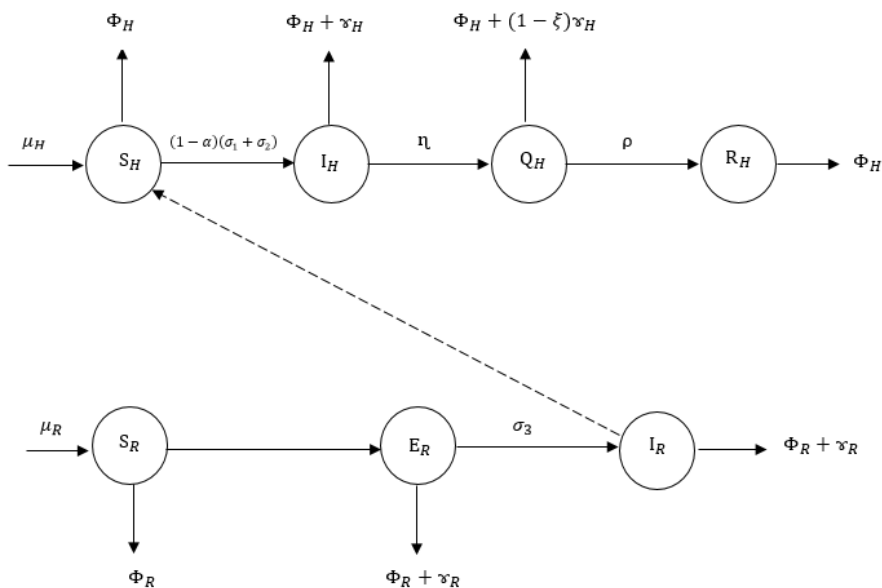


Figure 1. The flow diagram of the model.

2.3. The Model Equations

$$\frac{dS_H}{dt} = \mu_H - [(1 - \alpha)(\sigma_1 + \sigma_2)I_H - \Phi_H]S_H \tag{1}$$

$$\frac{dI_H}{dt} = (1 - \alpha)(\sigma_1 + \sigma_2)I_H S_H - [(\Phi_H + \varkappa_H) + \eta]I_H \tag{2}$$

$$\frac{dQ_H}{dt} = \eta I_H - [\Phi_H + (1 - \xi)\varkappa_H + \rho]Q_H \tag{3}$$

$$\frac{dR_H}{dt} = \rho Q_H - \Phi_H R_H \tag{4}$$

$$\frac{dS_R}{dt} = \mu_R - [\Phi_R + \sigma_3]S_R \tag{5}$$

$$\frac{dE_R}{dt} = \sigma_3 S_R - [(\Phi_R + \varkappa_R) + \sigma_3]E_R \tag{6}$$

$$\frac{dI_R}{dt} = \sigma_3 E_R - (\Phi_R + \varkappa_R)I_R \tag{7}$$

Such that

$$N_H(t) = S_H(t) + I_H(t) + Q_H(t) + R_H(t) \tag{8}$$

$$N_R(t) = S_R(t) + E_R(t) + I_R(t) \tag{9}$$

$$\frac{dN_H(t)}{dt} = \frac{dS_H(t)}{dt} + \frac{dI_H(t)}{dt} + \frac{dQ_H(t)}{dt} + \frac{dR_H(t)}{dt} \tag{10}$$

$$\frac{dN_R(t)}{dt} = \frac{dS_R(t)}{dt} + \frac{dE_R(t)}{dt} + \frac{dI_R(t)}{dt} \tag{11}$$

Such that

$$\frac{dN_H(t)}{dt} = \mu_H - [(1 - \alpha)(\sigma_1 + \sigma_2)I_H + \Phi_H]S_H + (1 - \alpha)(\sigma_1 + \sigma_2)I_H S_H - [(\Phi_H + \varkappa_H) + \eta]I_H + \eta I_H - \tag{12}$$

$$[\Phi_H + (1 - \xi)\varkappa_H + \rho]Q_H + \rho Q_H - \Phi_H R_H$$

$$\frac{dN_R(t)}{dt} = \mu_R - [\Phi_R + \sigma_3]S_R + \sigma_3 S_R - [(\Phi_R + \varkappa_R) + \sigma_3]E_R + \sigma_3 E_R - (\Phi_R + \varkappa_R)I_R \tag{13}$$

Let $S_h = \frac{S_H}{N_H}$ $I_h = \frac{I_H}{N_H}$ $Q_h = \frac{Q_H}{N_H}$ $R_h = \frac{R_H}{N_H}$ (14)

Also, $S_r = \frac{S_R}{N_R}$ $E_r = \frac{E_R}{N_R}$ $I_r = \frac{I_R}{N_R}$ (15)

Then the normalized system is as follows;

$$\frac{dS_h}{dt} = \frac{1}{N_H} \left[\frac{dS_H(t)}{dt} - S_h \frac{dN_H(t)}{dt} \right]$$

Substituting (1) and (10) using (14)

$$\frac{dS_h}{dt} = \frac{\mu_H(1-S_h)}{N_H} - (1 - \alpha)(\sigma_1 + \sigma_2)I_r S_h - \Phi_H S_h + (1 - \xi)\varkappa_H S_h q_h - I_r S_h S_h + \Phi_H S_h S_h + \Phi_H S_h I_h + \varkappa_H S_h I_h + \Phi_H S_h Q_h + \Phi_H S_h R_h \tag{16}$$

$$\frac{dI_h(t)}{dt} = \frac{1}{N_H} \left[\frac{dI_H(t)}{dt} - I_h \frac{dN_H(t)}{dt} \right]$$

$$\frac{dI_h(t)}{dt} = (1 - \alpha)(\sigma_1 + \sigma_2)I_r S_h - (\Phi_H + \varkappa_H)I_h - \eta I_h - \frac{\mu_H I_h}{N_H} + \Phi_H I_h S_h + \Phi_H I_h I_h + \varkappa_H I_h I_h - \Phi_H I_h Q_h + (1 - \xi)\varkappa_H I_h Q_h - \Phi_H I_h R_h \tag{17}$$

$$\frac{dQ_H(t)}{dt} = \frac{1}{N_H} \left[\frac{dQ_H(t)}{dt} - Q_h \frac{dN_H(t)}{dt} \right]$$

$$\frac{dQ_H(t)}{dt} = \eta I_h - \Phi_H Q_h - (1 - \xi)\varkappa_H Q_h - \rho Q_h - \frac{\mu_H Q_h}{N_H} - I_r S_h Q_h + \Phi_H Q_h S_h + \Phi_H Q_h I_h + \varkappa_H Q_h I_h + \Phi_H Q_h + (1 - \xi)\varkappa_H Q_h Q_h + \rho Q_h Q_h - \rho Q_h Q_h + \Phi_H Q_h R_h \tag{18}$$

$$\frac{dR_H(t)}{dt} = \frac{1}{N_R} \left[\frac{dR_H(t)}{dt} - R_h \frac{dN_H(t)}{dt} \right]$$

$$\frac{dR_H(t)}{dt} = \rho q_h - \Phi_H R_h - \frac{\mu_H R_h}{N_H} - I_r R_h S_h + \Phi_H R_h S_h + \Phi_H R_h R_h \tag{19}$$

$$\frac{dS_R(t)}{dt} = \frac{1}{N_R} \left[\frac{dS_R(t)}{dt} - S_r \frac{dN_R(t)}{dt} \right]$$

$$\frac{dS_R(t)}{dt} = \frac{\mu_R(1 - S_r)}{N_R} - (\Phi_R + \sigma_3)S_r + (\Phi_R + \sigma_3)S_r S_r - \sigma_3 S_r S_r + (\Phi_R + \varkappa_R)E_r S_r + \frac{(\Phi_R + \varkappa_R)S_r I_r}{N_R} \tag{20}$$

$$\frac{dE_R(t)}{dt} = \frac{1}{N_R} \left[\frac{dE_R(t)}{dt} - E_r \frac{dN_R(t)}{dt} \right]$$

$$\frac{dE_R(t)}{dt} = \sigma S_r - (\Phi_R + \varkappa_R)E_r - \sigma_3 E_r - \frac{\mu_R E_r}{N_R} + (\Phi_R + \sigma_3)E_r S_r - \sigma_3 E_r S_r + (\Phi_R + \varkappa_R)E_r E_r + (\Phi_R + \varkappa_R)E_r I_r \tag{21}$$

$$\frac{dI_R(t)}{dt} = \frac{1}{N_R} \left[\frac{dI_R(t)}{dt} - I_r \frac{dN_R(t)}{dt} \right]$$

$$\frac{dI_R(t)}{dt} = \sigma e_r - (\Phi_R + \varkappa_R)I_r - \frac{\mu_R I_r}{N_R} + (\Phi_R + \sigma_3)I_r S_r - \sigma_3 I_r S_r + (\Phi_R + \varkappa_R)E_r I_r + (\Phi_R + \varkappa_R)I_r I_r \tag{22}$$

However,

$$S_h + I_h + Q_h + R_h = 1 \quad \text{and also}$$

$$S_r + E_r + I_r = 1 \tag{23}$$

2.4. Existence and Uniqueness of Disease Free Equilibrium State E_0 of the Model

The disease free equilibrium state is both human and rodent hand side of equation (13) - (22) while setting the disease component $I_h = Q_h = R_h = 0, E_r = I_r = 0$

$$0 = \mu_H \frac{(1 - S_h)}{N_H} - S_h[(1 - \alpha)(\sigma_1 + \sigma_2) - I_r - \Phi_H - I_r S_h + \Phi_H S_h] \tag{24}$$

$$0 = (1 - \alpha)(\sigma_1 + \sigma_2)S_h \tag{25}$$

Let $\beta = (1 - \alpha)(\sigma_1 + \sigma_2)$

Hence,

$$0 = \beta S_h$$

$$S_h = 0 \tag{26}$$

Substituting (26) into (24)

$$0 = \frac{\mu_H}{N_H}$$

Hence,

$$0 = -S_h \beta + I_r S_h + \Phi_H S_h - I_r S_h^2 + \Phi_H S_h^2$$

Factorising S_h

$$0 = S_h[-\beta + I_r + \Phi_H] - S_h^2[I_r + \Phi_H]$$

Also,

$$0 = \mu_R \frac{(1 - S_r)}{N_R} - (\Phi_R + \sigma_3)S_r + (\Phi_R + \sigma_3)S_r^2 - \sigma_3 S_r^2 \tag{27}$$

$$0 = \sigma S_r - (\Phi_R + \gamma_R)E_r - \sigma_3 E_r - \frac{\mu_R E_r}{N_R} + (\Phi_R + \sigma_3)E_r S_r - \sigma_3 E_r S_r + (\Phi_R + \gamma_R)E_r E_r + (\Phi_R + \gamma_R)E_r I_r$$

$$0 = \sigma S_r \tag{28}$$

$$\text{Then } S_r = 0 \tag{29}$$

Substitute (29) into (27), we have

$$0 = \frac{\mu_R}{N_R} \tag{30}$$

2.5. The Disease Free Equilibrium

$$\text{Let } [S'_h, I'_h, Q'_h, R'_h, S'_r, E'_r, I'_r] = E_0 = [S^*_h, I^*_h, Q^*_h, R^*_h, S^*_r, E^*_r, I^*_r] \tag{31}$$

$$E_0 = \left[\frac{\mu_H}{\Phi_H}, 0, 0, 0, \frac{\mu_R}{\Phi_R}, 0, 0 \right] \tag{32}$$

At the disease free equilibrium $N_H^* = \frac{\mu_H}{\Phi_H} \qquad N_R^* = \frac{\mu_R}{\Phi_R}$

2.6. Stability Analysis of Disease Free Equilibrium State

To study the behavior of the system (16) – (22) around the disease free equilibrium state

$E_0 = \left[\frac{\mu_H}{\Phi_H}, 0, 0, 0, \frac{\mu_R}{\Phi_R}, 0, 0 \right]$, The linearized stability technique proposed in reference [17] is used, resulting in the derivation of a Jacobian transformation denoted as $J(E^0)$.

$$J(E_0) = \begin{bmatrix} -\left[\frac{\mu_H}{N_H} + (1 - \alpha)(\sigma_1 + \sigma_2) \right] & 0 & 0 & 0 & 0 & 0 & 0 \\ (1 - \alpha)(\sigma_1 + \sigma_2) & -((\Phi_H + \varkappa_H) + \eta) & 0 & 0 & 0 & 0 & 0 \\ 0 & \eta & -\rho & 0 & 0 & 0 & 0 \\ 0 & 0 & \rho & 0 & 0 & 0 & 0 \\ 0 & 0 & 0 & 0 & -\frac{\mu_R}{N_R} + (\Phi_R + \sigma_3) & 0 & 0 \\ 0 & 0 & 0 & 0 & \sigma & -((\Phi_R + \varkappa_R) + \sigma) & 0 \\ 0 & 0 & 0 & 0 & 0 & \sigma & -(\Phi_R + \varkappa_R) \end{bmatrix} \quad (33)$$

We now proceed to find the determinant of the Jacobian matrix $J E_0$. The determinant of a Jacobian matrix is given by the recursive definition for a 7 x 7 matrix.

$$Det [J(E_0)] = a_{11} \det[J(E_{0_{11}})] - a_{12} \det[J(E_{0_{12}})] + a_{13} \det[J(E_{0_{13}})] - a_{14} \det[J(E_{0_{14}})] + a_{15} \det[J(E_{0_{15}})] - a_{16} \det[J(E_{0_{16}})] + a_{17} \det[J(E_{0_{17}})]$$

From equation (33), $Det J(E_0) > 0$.

Likewise, by examining the trace of the Jacobian matrix $J[E_0]$ as shown in equation (33), it can be seen that

$$Trace J(E_0) = -\left[\frac{\mu_H}{N_H} + (1 - \alpha)(\sigma_1 + \sigma_2) \right] - [(\Phi_H + \varkappa_H) + \eta] - \rho - \left[\frac{\mu_R}{N_R} - \Phi_R + \sigma_3 \right] - [(\Phi_R + \varkappa_R) + \sigma] - (\Phi_R + \varkappa_R) \quad (34)$$

$Trace J(E_0)$ as shown above is < 0 .

Hence, $Trace J(E_0) < 0$

Since $Det [J(E_0)] > 0$ and $Trace J(E_0) < 0$ fulfill the predetermined threshold conditions according to Gerald (2012), the monkeypox virus disease free equilibrium $[E_0]$ also satisfies the requirements for a locally or globally asymptotic stability for the recovered population.

2.7. The Basic Reproductive Number (R_0) of the Model

The basic reproduction number, commonly represented as R_0 , is a fundamental measure in the field of epidemiology. The basic reproduction number (R_0) quantifies the contagiousness of a disease by indicating the average number of secondary infections induced by a single sick individual in a community that is entirely susceptible to the disease. In order to calculate the basic reproduction number (R_0) for the model (16-22), the methods outlined in reference [17] will be used, using the next generation matrix (NGM) method.

$$F = \begin{bmatrix} (1 - \alpha)\sigma_2 & (1 - \alpha)\sigma_1 \\ 0 & \sigma_3 \end{bmatrix} \quad (35)$$

$$V = \begin{bmatrix} \Phi_H + \varkappa_H + \eta & 0 \\ 0 & \Phi_R + \varkappa_R \end{bmatrix} \quad (36)$$

$$V^{-1} = \begin{bmatrix} -1 & 0 \\ \frac{1}{\Phi_H + \varkappa_H + \eta} & -1 \\ 0 & \frac{1}{\Phi_R + \varkappa_R} \end{bmatrix} \quad (37)$$

Where F represents the rate at which new infections occur and V represents the movement of persons across compartments via various ways. Then the next matrix denoted by FV^{-1} is given as

$$FV^{-1} = \begin{bmatrix} (1-\alpha)\sigma_2 & (1-\alpha)\sigma_1 \\ 0 & \sigma_3 \end{bmatrix} \begin{bmatrix} \frac{-1}{\Phi_H + \gamma_H + \eta} & 0 \\ 0 & \frac{-1}{\Phi_R + \gamma_R} \end{bmatrix} \tag{38}$$

$$FV^{-1} = \begin{bmatrix} \frac{-(1-\alpha)\sigma_2}{\Phi_H + \gamma_H + \eta} & \frac{-(1-\alpha)\sigma_1}{\Phi_R + \gamma_R} \\ 0 & \frac{-\sigma_3}{\Phi_R + \gamma_R} \end{bmatrix} \tag{39}$$

We find the Eigen values of FV^{-1} by setting the determinant $|FV^{-1} - \lambda I| = 0$, I is a unit matrix

$$\left| \begin{bmatrix} \frac{-(1-\alpha)\sigma_2}{\Phi_H + \gamma_H + \eta} & \frac{-(1-\alpha)\sigma_1}{\Phi_R + \gamma_R} \\ 0 & \frac{-\sigma_3}{\Phi_R + \gamma_R} \end{bmatrix} - \begin{bmatrix} \lambda & 0 \\ 0 & \lambda \end{bmatrix} \right| = 0 \tag{40}$$

$$\left| \begin{bmatrix} \frac{-(1-\alpha)\sigma_2}{\Phi_H + \gamma_H + \eta} - \lambda & \frac{-(1-\alpha)\sigma_1}{\Phi_R + \gamma_R} \\ 0 & \frac{-\sigma_3}{\Phi_R + \gamma_R} - \lambda \end{bmatrix} \right| = 0 \tag{41}$$

$$\left[\frac{-\sigma_3}{\Phi_R + \gamma_R} - \lambda \right] \left[\frac{-(1-\alpha)\sigma_2}{\Phi_H + \gamma_H + \eta} - \lambda \right] - 0 = 0 \tag{42}$$

From (42),

$$\frac{-\sigma}{\Phi_R + \gamma_R} = \lambda_1$$

$$\frac{-(1-\alpha)\sigma_2}{\Phi_H + \gamma_H + \eta} = \lambda_2$$

Since $\lambda_1 < 0$ and also $\lambda_2 < 0$ in which $0 < 1$, hence, $R_0 < 1$ which satisfies the threshold.

3. Results and Discussion

In this section, the effectiveness of public awareness and campaigns and the effectiveness of the infected quarantine on the spread of the monkeypox virus are examined. The numerical simulation of the monkeypox virus is analysed using the baseline values given in Table 3. The numerical simulations were done and plotted against time (months) using MATLAB, and the results are shown in Figures 2–13 to illustrate the effect of public awareness and campaigns and the effectiveness of getting the infected quarantined.

Table 3. Model parameters and values used in the simulation.

Parameters	Values	Source
μ_H	0.029	[3,21]
μ_R	0.2	[3,21]
σ_1	0.00006	[2,21]
σ_2	0.00025	[2,21]
σ_3	0.027	[2,21]
Φ_H	0.15	[2,21]
ψ_H	0.2	[12,21]
η	0.83	[3,21]
Φ_R	0.002	[2,21]
ψ_R	0.5	[21]
ρ	0.52	[21]

α	0 – 1	Control Parameter
ϵ	0 – 1	Control Parameter

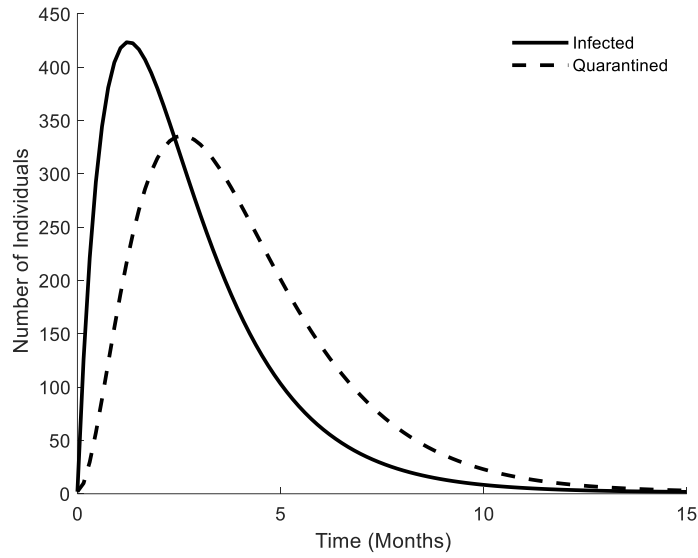


Figure 2. Numerical Simulation of the infected and quarantined population.

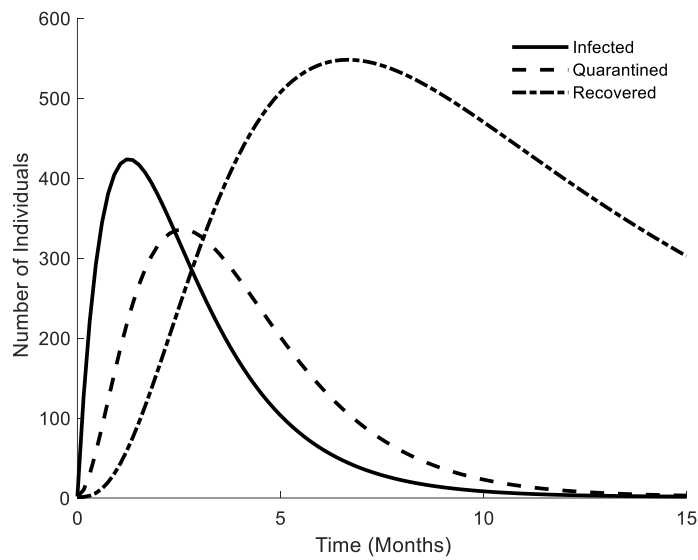


Figure 3. Numerical Simulation of the infected, quarantined and recovered population.

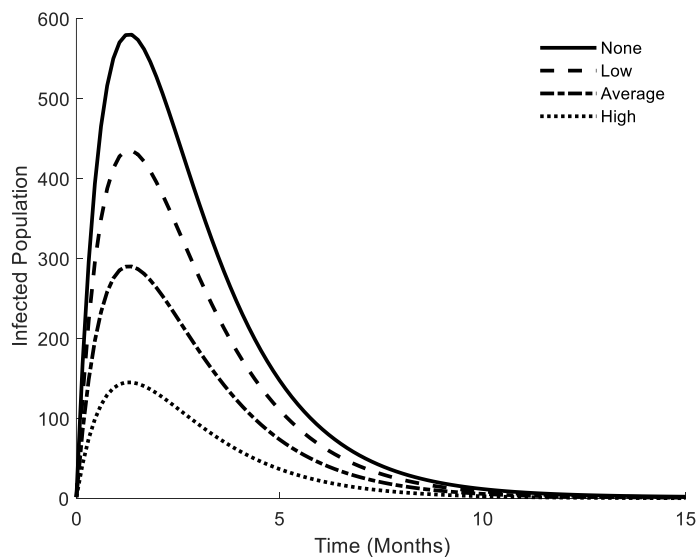


Figure 4. Variation in infected population for measuring the effectiveness of public enlightenment.

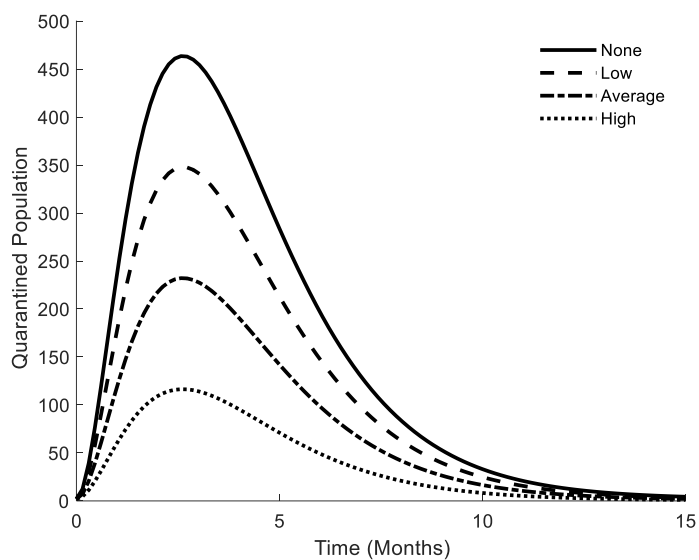


Figure 5. Variation in quarantined population for measuring the effectiveness of public enlightenment.

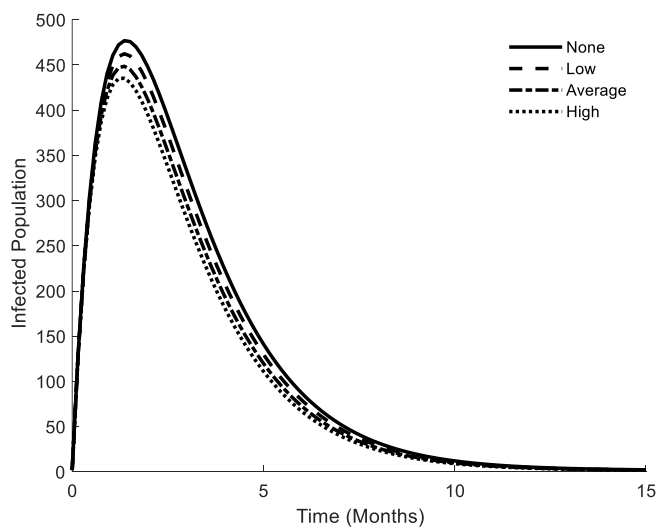


Figure 6. Variation in infected population for measuring the effectiveness of quarantined.

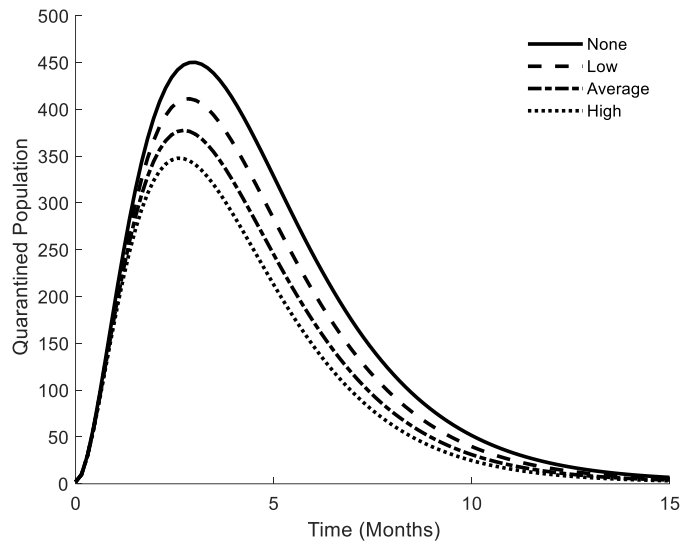


Figure 7. Variation in quarantined population for measuring the effectiveness of quarantined.

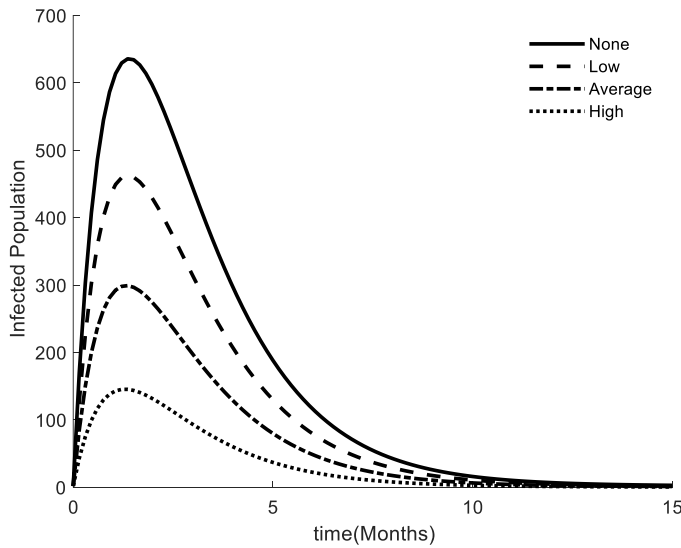


Figure 8. Variation in infected population for measuring the effectiveness of public enlightenment and rate of quarantined.

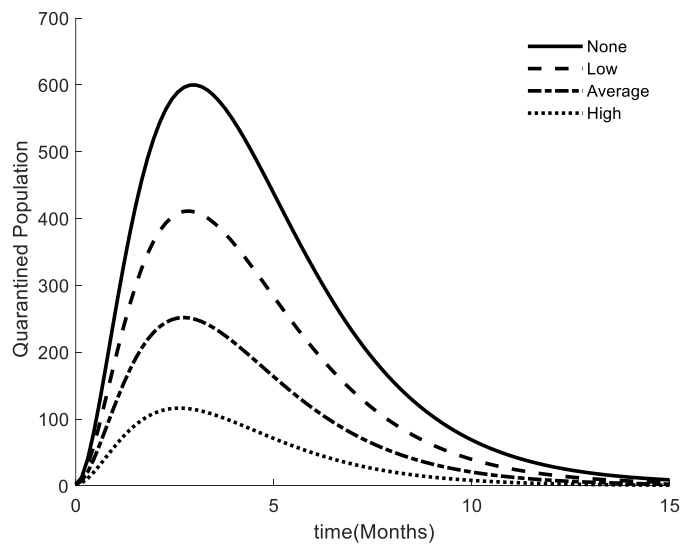


Figure 9. Variation in quarantined population for measuring the effectiveness of public enlightenment and the rate of

quarantined.

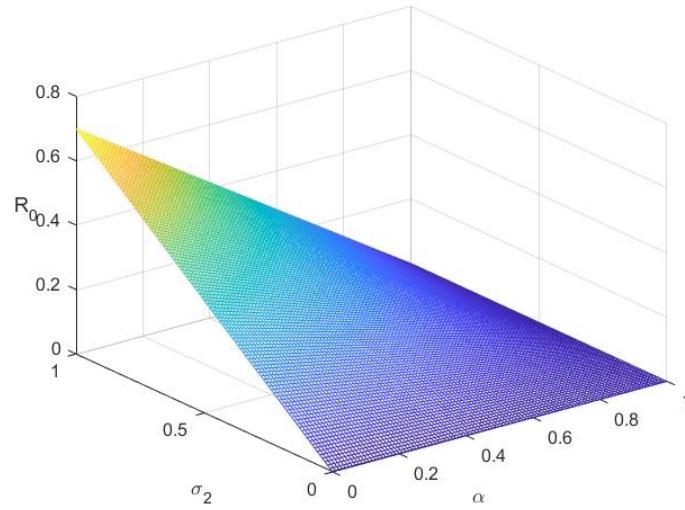


Figure 10. Surface plot showing the impact of α and σ_2 on R_0 .

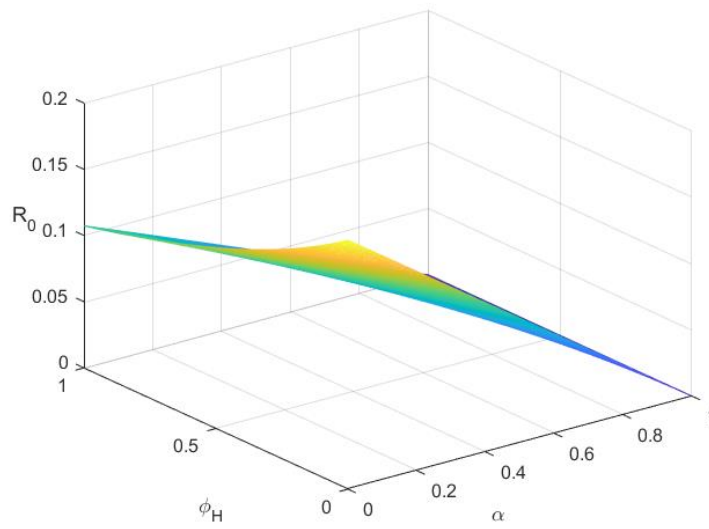


Figure 11. Surface plot showing the impact of α and ϕ_H on R_0 .

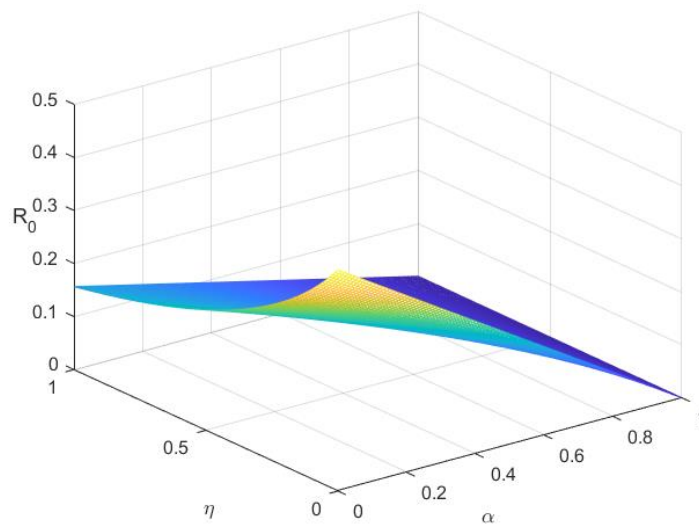


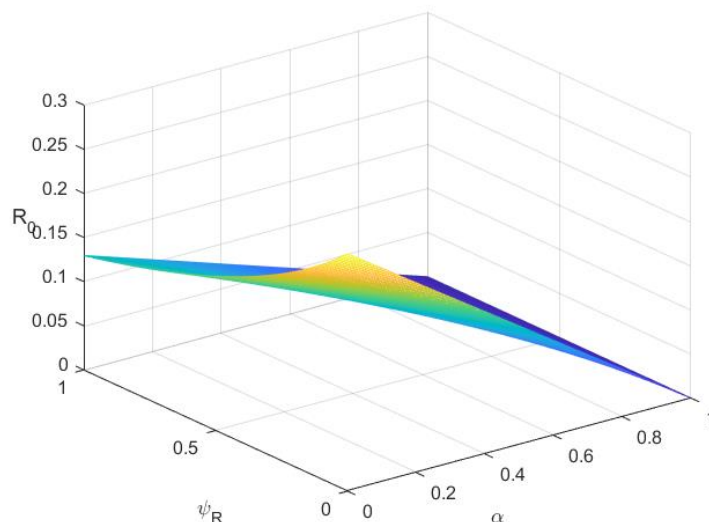
Figure 12. Surface plot showing the impact of α and η on R_0 enlightenment.**Figure 13.** Surface plot showing the impact of α and ψ_R on R_0 .

Figure 2 describes the numerical simulation of the infected and quarantined populations. The infected population is seen to have reached its peak before the quarantined population and then drastically reduced. Furthermore, the number of individuals in the infected population is seen to be higher than those in the quarantined population, which implies a high rate of infection at the start of the viruses. After a while, individuals then rush into the quarantined population owing to the different peak attained by the infected population and quarantined population. Figure 3 illustrates the numerical simulation of the infected, quarantined, and recovered populations. It is observed that as the number of individuals keeps increasing in the infected compartment and quarantined population, the population of the recovery compartment keeps increasing.

Figure 4 depicts the variation in the infected population for measuring the effectiveness of public enlightenment only. The control parameters used are: $\alpha = 0, 0.25, 0.5, 0.75$. With an increase in the parameter measuring the rate of effectiveness of public enlightenment and campaigns, the aftermath is a reduction in the infected population. This implies that if public awareness could be increased, the rate of infection would be reduced, thereby reducing the number of individuals that would be infected with monkeypox.

Figure 5 displays the variation in quarantined population for measuring the effectiveness of public enlightenment only. The control parameters used are: $\alpha = 0, 0.25, 0.5, 0.75$. It is noted that an increase in the parameter measuring the rate of effectiveness of public enlightenment and campaigns resulted in a reduction in the quarantined population. This implies that if public awareness could be increased, the rate of infection would be reduced, thereby reducing the number of individuals that would need to be quarantined with monkeypox.

Figure 6 shows the variation in the infected population for measuring the effectiveness of quarantining alone. The control parameters used are: $\epsilon = 0, 0.25, 0.5, 0.75$. As observed, with an increase in the parameter measuring the rate of effectiveness of individuals quarantined, the aftermath is a reduction in the infected population. This implies that if the number of infected populations could be increased, there would be assurance in the reduction of individuals that would be infected. However, the difference might be small, but it counts too. At least it would reduce the chances of a secondary infection of monkeypox.

Figure 7 demonstrates the variation in quarantined population for measuring the effectiveness of quarantined only. The control parameters used are: $\epsilon = 0, 0.25, 0.5, 0.75$. It is seen that the population of the quarantined compartment reduces with an increase in the rate at which individuals are quarantined.

The variation in the infected population for measuring the effectiveness of public enlightenment and the rate of quarantine is shown in Figure 8. The control parameters used are: $\alpha, \epsilon = 0, 0.25, 0.5, 0.75$. It is observed that the combined effort produces more results than the single measure. Increasing the rate of public awareness and the rate of quarantining produced greater results. This reduces the number of infections, thereby reducing the population of infected people.

The variation in quarantined population for measuring the effectiveness of public enlightenment and the rate of quarantine is described in Figure 9. The control parameters used are: $\alpha, \epsilon = 0, 0.25, 0.5, 0.75$. It is observed that the combined effort produces more results than the single measure. Increasing the rate of public awareness and the rate of quarantining produced greater results. This reduces the number of infections and, thereby, the population quarantined.

Figure 10 displays the surface plot showing the impact of α and σ_2 on R_0 . It has been found that if the rate of contact with the rodent could be reduced and the rate of awareness could be increased, then the virus would be wiped out of the human population. An increase in the contact rate of humans with a rodent would result in an increase in the reproduction number, which implies the virus would stay and the human population would soon go into extinction.

Figure 11 illustrates the surface plot showing the impact of α and ϕ_H on R_0 . Figure 11 illustrates the effectiveness of public awareness in the face of natural death. Public awareness plays a key role in reducing the reproduction number, which implies that if public awareness could be effectively imbibed, the reproduction number would reduce and stabilize.

The surface plot showing the impact of α and η on R_0 enlightenment is seen in Figure 12. It is found that if the number of infected individuals could be increased and the rate of awareness could be increased, then the virus would be wiped out in the human population.

The surface plot showing the impact of α and ψ_R on R_0 is displayed in Figure 13. It is found that if the virus death rate of rodents could be increased coupled with an increase in public awareness, the basic reproduction number would reduce drastically and the virus would be wiped out of the human population.

4. Conclusion

In this work, the dynamics of the monkeypox virus's transmission were described using a deterministic model made up of systems of ordinary differential equations. The establishment of the area in which the model is epidemiologically viable has been confirmed. The model is locally asymptotically stable when the reproduction number $R_0 < 1$, which implies that the monkeypox virus will eventually be eliminated from the population. But, unstable when $R_0 > 1$, which implies that the monkeypox virus would continue to be prevalent among us if control measures were neglected. Numerical simulations were conducted to further examine the effectiveness of public awareness and the rate at which individuals were quarantined. The study concludes that the effectiveness of the combined form of public awareness and quarantine produced more results, followed by the effectiveness of public awareness alone, and then the results achieved when infected individuals were quarantined. If the measures could

be combined at a higher rate, the virus peak would reduce greatly, and the virus would not persist among humans.

References

- [1] Babak, P., Lauren, A.M., Danuta, M.S., Mel, K., David, M.P. and Robert, C.B. (2005). Modeling Control Strategies of Respiratory Pathogens. *Emerging Infectious Diseases*, 11, 1249-1256.
- [2] Bhunu, C. P., and Mushayabasa, S. (2011). Modelling the transmission dynamics of pox-like infections. *IAENG International Journal*, 41(2):1–9.
- [3] Bhunu, C., Garira, W., and Magombedze, G. (2009). Mathematical analysis of a two strain hiv/aids model with antiretroviral treatment. *Acta Biotheoretica*, 57(3):361–381
- [4] Center for Disease Control (2022) Interim clinical guidance for the treatment of monkeypox. <https://www.cdc.gov/poxvirus/monkeypox/index.html>. Accessed 15 April 2023.
- [5] Daniel, D. O. (2020). Mathematical Model for the Transmission of Covid-19 with Nonlinear Forces of Infection and the Need for Prevention Measure in Nigeria. *Journal of Infectious Diseases and Epidemiology*, 6(5):158.
- [6] Durski, K. N. , McCollum, A. M., Nakazawa, Y., Petersen, B. W., Reynolds, M. G., Briand, S., Djingarey, M. H., Olson, V., Damon, I. K., Khalakdina, A. (2018) Emergence of monkeypox-west and central Africa, 1970–2017. *Morbidity and Mortality Weekly Report*, 67(10):306
- [7] Emeka, P., Ounorah, M., Eguda, F., Babangida, B. (2018). Mathematical model for monkeypox virus transmission dynamics. *Epidemiology: Open Access*, 8(3):1000348.
- [8] Grant, R., Nguyen, L-B. L., and Breban, R. (2020). Modelling human-to-human transmission of monkeypox. *Bulletin of the World Health Organization*, 98(9):638
- [9] Jezek, Z., Szczeniowski, M., Paluku, K., Mutombo, M., and Grab, B. (1988). Human monkeypox: confusion with chickenpox. *Acta Tropica*, 45(4):297–307.
- [10] Lasisi, N., Akinwande, N., and Oguntolu, F. (2020) Development and exploration of a mathematical model for transmission of monkeypox disease in humans. *Mathematical Models in Engineering*, 6(1):23–33
- [11] Leggiadro, R. J. (2018). Emergence of Monkeypox—West and Central Africa, 1970–2017. *Pediatric Infectious Disease Journal*, 37(7), 721–721.
- [12] Odom, M. R., Curtis, H. R, and Lefkowitz, E. J. (2009) Poxvirus protein evolution: family wide assessment of possible horizontal gene transfer events. *Virus Resolution*, 44:233–249.
- [13] Onitilo, S. A. and Daniel, D. O. (2022). Mathematical Modelling and Simulation of Coronavirus (COVID-19) in Lagos, Nigeria. *Cankaya University Journal of Science and Engineering*, 19(2):078-094.
- [14] Onitilo, S. A., Daniel, D. O. and Haruna, H. A. (2021). Modeling Analysis of Coronavirus Epidemic in Nigeria using Lyapunov functions. *FUW trends in Science and Technology Journal*, 6(2): 627-632.
- [15] Onitilo, S. A, Usman, M. A., Daniel, D. O., Odetunde, O. S., Ogunwobi, Z. O., Hamed, F. A., Olubanwo, O. O., Ajani, A. S., Sanusi, A. S., Haruna, A. H. (2022). Mathematical Modelling of the Transmission Mechanism of Plasmodium Falciparum. *Natural Sciences and Advanced Technology Education*, 31(5): 435-457.
- [16] Onitilo, S. A, Usman, M. A., Daniel, D. O., Odule, T. J., and Sanusi, A. S., (2023). Modelling the Transmission Dynamics of Cholera Disease with the Impact of Control Strategies in Nigeria. *Cankaya*

University Journal of Science and Engineering, 20(1):035-052.

- [17] Onitilo, S. A., Usman, M. A., Odetunde, S. O., Hammed, F. A., Ogunwobi, Z. O., Haruna, H. A. and Daniel, D. O. (2020a). Mathematical Modeling of 2019 Novel Coronavirus (2019 - nCoV) Pandemic and Reinfection in Nigeria using SEIAHQR model. *Bulgarian Journal of Science Education*, 29(3):398-413.
- [18] Onitilo, S. A., Usman, M. A., Taiwo, A. I. Dehinsilu, O. A., Adekola, M. A. and Daniel, D. O. (2020b). Mathematical modeling, prediction and control of COVID-19 in Nigeria as one of the Epicentre in Africa. *Africa Journal of Science and Nature*, 11:169-182. P-ISSN:2536-6904, E-ISSN: 2705-2761.
- [19] Peter, O. J., Kumar, S., Kumari, N., Oguntolu, F. A., Oshinubi, K., and Musa, R. (2021a) Transmission dynamics of monkeypox virus: a mathematical modelling approach. *Modeling Earth Systems and Environment*, 1–12
- [20] Peter, O. J., Kumar, S., Kumari, N., Oguntolu, F. A., Oshinubi, K., & Musa, R. (2021b). transmission dynamics of Monkeypox virus: a mathematical modelling approach. *Modeling Earth Systems and Environment*, 8(3), 3423–3434. <https://doi.org/10.1007/s40808-021-01313-2>
- [21] Peter, O. J., Kumar, S., Kumari, N., Oguntolu, F. A., Oshinubi, K., and Musa, R. (2022). Transmission dynamics of Monkeypox virus: a mathematical modelling approach. *Modeling Earth Systems and Environment*, 8:3423–3434.
- [22] Rezza, G. (2019). Emergence of human monkeypox in west Africa. *The Lancet Infectious Diseases*, 19(8), 797–799. [https://doi.org/10.1016/s1473-3099\(19\)30281-6](https://doi.org/10.1016/s1473-3099(19)30281-6)
- [23] Somma, S., Akinwande, N., Chado, U. (2019) A mathematical model of monkey pox virus transmission dynamics. *Ife Journal of Science*, 21(1):195–204.

Applications of Mohand Transform

Nihal ÖZDOĞAN ^{1*} 

¹ Bursa Technical University, Faculty of Science and Engineering, Department of Mathematics, Bursa, Turkey

Abstract

Investigating solutions of differential equations has been an important issue for scientists. Researchers around the world have talked about different methods to solve differential equations. The type and order of the differential equation enable us to decide the method that we can choose to find the solution of the equation. One of these methods is the integral transform, which is the conversion of a real or complex valued function into another function by some algebraic operations. Integral transforms are used to solve many problems in mathematics and engineering, such as differential equations and integral equations. Therefore, new types of integral transforms have been defined, and existing integral transforms have been improved. One of the solution methods of many physical problems as well as initial and boundary value problems are integral transforms. Integral transforms were introduced in the first half of the 19th century. The first historically known integral transforms are Laplace and Fourier transforms. Over the time, other transforms that are used in many fields have emerged. The aim of this article is to describe the Mohand transform and to make applications of linear ordinary differential equations with constant coefficients without any major mathematical calculations. This integral transform method is an alternative method to existing transforms such as Laplace transform and Kushare transform. When recent studies in the literature are examined, it can be said that Mohand transform is preferred because it is easy to apply.

Keywords: Differential equation, Integral transform, Laplace and Fourier transform.

Cite this paper as: Ozdogan N. (2024). Applications of Mohand Transform, 8(1):18-24.

*Corresponding author: Nihal ÖZDOĞAN
E-mail: nihal.ozdogan@btu.edu.tr

Received Date: 14/09/2023
Accepted Date: 24/01/2024
© Copyright 2024 by
Bursa Technical University. Available
online at <http://jise.btu.edu.tr/>



The works published in the journal of Innovative Science and Engineering (JISE) are licensed under a Creative Commons Attribution-NonCommercial 4.0 International License.

1. Introduction

Integral transforms [1-12] such as Laplace, Mohand, Aboodh, Anuj, Kamal, Kushare, Mahgoub, Ara, HY, Sadik etc. have assumed an important role to solve science, engineering, and real life problems. Researchers have been proposed these transforms to solve the problems including differential equations, telegraph differential equations, integral equations, integro-differential equations.

Attaweel and Almassry used Mohand transform, which they considered as a modified version of Laplace and Sumudu transforms to solve ordinary differential equations with variable coefficients [12]. Dehinsulu O.A [13] suggested the Mahgoub transform method to solve linear convection-diffusion problems with constant coefficients. When Dehinsulu compared the results obtained by this method to the exact solutions, he found an excellent agreement. Furthermore, in the year (2022), Abbas E.S. et al. [14] described Aboodh transform to solve some telegraph equations with specific initial conditions. Aggarwal S. et al. [15] used recently developed transform method called Rishi transform to acquire the analytical solution of linear volterra integral equation. Also, Kuffi E. et al. [16] introduced a new integral transform method named Emad-Falih transform to find the solutions of first-order and second-order ordinary differential equations. Gupta R. [17] proposed a novel transform method called Rohit transform to analyze boundary value problems. However, Chaudhary R. and Aggarwal S. [18] presented a comparative work of Laplace and Mohand transforms. Their results in application section demonstrated that both transforms are closely connected. In the year 2023, Musht and Kuffi [19] compared the Sadik transform and the complex Sadik transform to solve systems of ordinary differential equations. Integral transforms will continue to be used in many scientific researches because researchers argue that integral transforms give accurate solutions to many complex problems and are applicable in many different fields such as astronomy and mechanics.

2. Mohand Transforms Basic Definitions and Properties

2.1. Mohand transform definition [18, 20, 21]

Mohand transform is described for a function of exponential order in the A set as:

$$A = \left\{ f(t) : \exists M, k_1, k_2 > 0, |f(t)| < Me^{\frac{|t|}{k_j}}, \text{ if } t \in (-1)^j \times [0, \infty) \right\}$$

where $f(t)$ is a dedicated function in the set A , M is a finite number, and k_1, k_2 can be finite or infinite.

Mohand transform denoted by operator M is defined as:

$$M\{f(t)\} = K(v) = v^2 \int_0^\infty f(t)e^{-vt} dt, \quad t \geq 0, \quad k_1 \leq v \leq k_2.$$

2.2. Linearity feature of Mohand transform [18, 20]

Let $M\{f_1(t)\} = K_1(v)$ and $M\{f_2(t)\} = K_2(v)$. Then Mohand transform of $M\{af_1(t) + bf_2(t)\}$ is given as:

$$M\{af_1(t) + bf_2(t)\} = aK_1(v) + bK_2(v)$$

where a, b are arbitrary constants.

2.3. Scalar variation feature of Mohand transform [12, 18]

Let $M\{f(t)\} = K(v)$. Mohand transform of a function $f(at)$ is defined as:

$$M\{f(at)\} = aK\left(\frac{v}{a}\right).$$

2.4. Scrolling feature of Mohand transform [12, 18]

Let $M\{f(t)\} = K(v)$. Mohand transform of a function $e^{at}f(t)$ is defined as:

$$M\{e^{at}f(t)\} = \frac{v^2}{(v-a)^2}K(v-a).$$

2.5. Convolution theorem for Mohand transform [18, 21]

Let $M\{f_1(t)\} = K_1(v)$ and $M\{f_2(t)\} = K_2(v)$. Then Mohand transform of their convolution $f_1(t) * f_2(t)$ is given as:

$$M\{f_1(t) * f_2(t)\} = \frac{1}{v^2}M\{f_1(t)\}M\{f_2(t)\},$$

$$M\{f_1(t) * f_2(t)\} = \frac{1}{v^2}K_1(v)K_2(v),$$

where $f_1(t) * f_2(t)$ is described as:

$$f_1(t) * f_2(t) = \int_0^t f_1(t-x)f_2(x)dx = \int_0^t f_1(x)f_2(t-x)dx.$$

2.6. Mohand transform of the derivatives [18, 22]

Let $M\{f(t)\} = K(v)$. Mohand transforms of the derivatives of a function of $f(t)$ are given as:

- $M\{f'(t)\} = vK(v) - v^2f(0)$
- $M\{f''(t)\} = v^2K(v) - v^3f(0) - v^2f'(0)$
- $M\{f^{(n)}(t)\} = v^nK(v) - v^{n+1}f(0) - v^n f'(0) - \dots - v^2 f^{(n-1)}(0)$

2.7. Mohand transform of the integral [18, 22]

Let $M\{f(t)\} = K(v)$. Mohand transform of the integral of a function $f(t)$ is given as:

$$M\left\{\int_0^t f(t) dt\right\} = \frac{1}{v}K(v).$$

3. Mohand Transform and Inverse Mohand Transform of Some Elementary Functions [12, 20]

- $M\{1\} = v = K(v)$

Inversion formula: $M^{-1}\{v\} = 1 = f(t)$

- $M\{t^n\} = \frac{n!}{v^{n-1}} = K(v)$, $n \in N$

Inversion formula: $M^{-1}\left\{\frac{n!}{v^{n-1}}\right\} = t^n = f(t)$

- $M\{e^{at}\} = \frac{v^2}{v-a} = K(v)$

Inversion formula: $M^{-1}\left\{\frac{v^2}{v-a}\right\} = e^{at} = f(t)$

- $M\{\sin at\} = \frac{av^2}{v^2+a^2} = K(v)$

Inversion formula: $M^{-1}\left\{\frac{av^2}{v^2+a^2}\right\} = \sin at = f(t)$

- $M\{\cos at\} = \frac{v^3}{v^2+a^2} = K(v)$

Inversion formula: $M^{-1}\left\{\frac{v^3}{v^2+a^2}\right\} = \cos at = f(t)$

- $M\{\sin at\} = \frac{av^2}{v^2-a^2} = K(v)$

Inversion formula: $M^{-1}\left\{\frac{av^2}{v^2-a^2}\right\} = \sin at = f(t)$

- $M\{\cosh at\} = \frac{v^3}{v^2-a^2} = K(v)$

Inversion formula: $M^{-1}\left\{\frac{v^3}{v^2-a^2}\right\} = \cosh at = f(t)$

4. Applications of Ordinary Differential Equations of First and Second Order by Mohand Transform

Assume that the first-order ordinary differential equation with the initial condition $y(0) = a$ is given as

$$\frac{dy}{dt} + ky = g(t) \quad , \quad t > 0 \quad (1)$$

where Mohand transform of $g(t)$ as a function of “ t ” is denoted by $G(v)$ and a, k are constants.

Applying Mohand transform on both side in equation (1), we have

$$M\left\{\frac{dy}{dt}\right\} + kM(y) = M\{g(t)\}$$

$$vM(y) - v^2y(0) + kM(y) = G(v)$$

$$vM(y) + kM(y) = G(v) + av^2$$

$$M(y) = \frac{G(v)}{(v+k)} + \frac{av^2}{(v+k)}$$

Then we find the solution by applying the inverse Mohand transform in the step above.

Assume that the second-order ordinary differential equation with the initial conditions $y(0) = a, y'(0) = b$ is given as

$$\frac{d^2y}{dt^2} + k\frac{dy}{dt} + ly = g(t) \quad , \quad t > 0 \quad (2)$$

where Mohand transform of $g(t)$ as a function of “ t ” is

denoted by $G(v)$ and a, b, k, l are constants.

Applying Mohand transform on both side in equation (2), we have

$$M\left\{\frac{d^2y}{dt^2}\right\} + kM\left\{\frac{dy}{dt}\right\} + lM(y) = M\{g(t)\}$$

$$\{v^2M(y) - v^3y(0) - v^2y'(0)\} + k\{vM(y) - v^2y(0)\} + lM(y) = G(v)$$

$$M(y)(v^2 + kv + l) = G(v) + av^3 + v^2(b + ak)$$

$$M(y) = \frac{G(v)}{(v^2 + kv + l)} + \frac{av^3}{(v^2 + kv + l)} + \frac{v^2(b + ak)}{(v^2 + kv + l)}$$

Then we find the solution by applying the inverse Mohand transform in the step above.

Example. Assume that the first-order differential equation

$$y' + 27y = \cos 9t, \quad y(0) = 0 \quad (3)$$

Applying Mohand transform on both side in equation (3), we get

$$\begin{aligned} M\{y'\} + 27M(y) &= M\{\cos 9t\} \\ vM(y) - v^2y(0) + 27M(y) &= \frac{v^3}{v^2 + 81} \\ M(y) &= \frac{v^3}{(v^2 + 81)(v + 27)} \\ M(y) &= \frac{1}{30} \frac{v^3}{(v^2 + 81)} + \frac{1}{10} \frac{v^2}{(v^2 + 81)} - \frac{1}{30} \frac{v^2}{(v + 27)} \end{aligned}$$

The inverse Mohand transform of the equation above gives us the solution:

$$y(t) = \frac{1}{30} \cos 9t + \frac{1}{90} \sin 9t - \frac{1}{30} e^{-27t}$$

Example. Assume that the second-order differential equation

$$y'' + y = 0 \quad , \quad y(0) = y'(0) = 1 \quad (4)$$

Applying Mohand transform on both side in equation (4), we have

$$\begin{aligned} M\{y''\} + M(y) &= 0 \\ v^2M(y) - v^3y(0) - v^2y'(0) + M(y) &= 0 \\ (v^2 + 1)M(y) &= v^3 + v^2 \\ M(y) &= \frac{v^3}{v^2 + 1} + \frac{v^2}{v^2 + 1} \end{aligned}$$

The inverse Mohand transform of the equation above is simply obtained as:

$$y(t) = \cos t + \sin t$$

Example. Consider the following equation:

$$y' + 13y = e^{11t} \quad , \quad y(0) = 1 \quad (5)$$

Applying Mohand transform on both side in equation (5), we have

$$\begin{aligned} M\{y'\} + 13M(y) &= M\{e^{11t}\} \\ vM(y) - v^2y(0) + 13M(y) &= \frac{v^2}{v - 11} \\ (v + 13)M(y) &= \frac{v^2}{v - 11} + v^2 \\ M(y) &= \frac{v^2(v - 10)}{(v - 11)(v + 13)} \\ M(y) &= \frac{1}{24} \frac{v^2}{(v - 11)} + \frac{23}{24} \frac{v^2}{(v + 13)} \end{aligned}$$

The inverse Mohand transform of the equation above gives us the solution:

$$y(t) = \frac{1}{24} e^{11t} + \frac{23}{24} e^{-13t}$$

Example. Assume that the following equation

$$y'' - 3y' + 2y = 0 \quad , \quad y(0) = 1 \quad , \quad y'(0) = 4 \quad (6)$$

Applying Mohand transform on both side in equation (6), we have

$$M\{y''\} - 3M\{y'\} + 2M(y) = 0$$

$$v^2M(y) - v^3y(0) - v^2y'(0) - 3vM(y) + 3v^2y(0) + 2M(y) = 0$$

$$(v^2 - 3v + 2)M(y) = v^3 + v^2$$

$$M(y) = \frac{v^3 + v^2}{v^2 - 3v + 2}$$

$$M(y) = \frac{3v^2}{v-2} - \frac{2v^2}{v-1}$$

The inverse Mohand transform of the equation above gives us the solution:

$$y(t) = 3e^{2t} - 2e^t$$

5. Conclusions

In the present article, we have defined Mohand transform to solve linear ordinary differential equations with constant coefficients. We can say that the proposed transform method is, as an alternative approach, easy and understandable. Examples show that the method can be applied without longer calculations. The examples here can also be solved with other integral transforms available in the literature. We preferred this transform method because we think that not much work has been done on this subject. However, when the Mohand transform is compared with the Laplace transform, it can be seen that both methods work in the same way and give the exact solution of ordinary differential equations. This comparison will be the subject of our another study. I think that different useful integral transforms will also be mentioned by researchers in the future.

Acknowledgements

The authors gratefully thank to the referees for the constructive comments and recommendations which definitely help to improve the readability and quality of the paper.

References

- [1] Katre, N.T. and Katre, R.T. (2021). A comparative study of Laplace and Kamal transforms, International Conference on Research Frontiers in Sciences (ICRFS 2021), Nagpur, India, 5 th- 6 th February 2021.
- [2] Fadhil, R.A and Alkfari, B.H.A. (2023). Convolution HY transform for second kind of linear Volterra integral equation, Al-Kadhumi 2nd International Conference on Modern Applications of Information and Communication Technology, 29 March 2023, Volume 2591, Issue 1.
- [3] Mohmad, Z.S. and Sadikali, L.S. (2021). Sadik Transform, The generalization of All the transform Who's kernal is Of Exponential Form With The Application In Differential Equation With Variable Coefficients, Turkish Journal of Computer and Mathematics, 3264-3272.
- [4] Rashdi, H.Z. (2022). Using Anuj Transform to Solve Ordinary Differential Equations with Variable Coefficients, Scientific Journal for the Faculty of Scientific-Sirte University, Vol. 2, No. 1, 38-42.
- [5] Aggarwal, S. and Gupta, A.R. (2019). Dualities between Mohand Transform and Some Useful Integral Transforms. International Journal of Recent Tecnology and Engineering, 8 (3), 843-847.

- [6] Sornkaew, P. and Phollamat, K. (2021). Solution of Partial Differential Equations by Using Mohand Transforms, *Journal of Physics: Conference Series*, Vol. 1850, Iss. 1.
- [7] Saadeh, R. Qazza, A. and Burqan, A. (2020). A New Integral Transform: Ara Transform and Its Properties and Applications. *Symmetry*, 12 (6), 925.
- [8] Kushare, S.R., Patil, D.P. and Takate, A.M. (2021). The New Integral Transform “KUSHARE Transform”, *International Journal of Advances in Engineering and Management*. 3 (9), 1589-1592.
- [9] Johansyah, M.D., Supriatna, A.K., Rusyaman E. and Saputra, J. (2022). Solving Differential Equations of Fractional Order Using Combined Adomian Decomposition Method with Kamal Integral Transformation, *Mathematics and Statistics*, 10 (1), 187-194.
- [10] Patil, D.P. (2021). Aboodh and Mahgoub Transform in Boundary Value Problems. *Scientific Journal for of System of Ordinary Differential Equations. International Journal of Advanced Research in Science, Communication and Technology*, 6 (1), 67-75.
- [11] Aggarwal, S., Chauhan, R. and Sharma, N. (2018). Application of Aboodh Transform for Solving Linear Volterra Integro-Differential Equations of Secon Kind. *International Journal of Research in Advent Technology*, 6 (6), 1186-1190.
- [12] Attaweel, M.E. and Almassry, H. (2020). On the Mohand Transform and Ordinary Differential Equations with Variable Coefficients. *Al-Mukhtar Journal of Sciences*, 35 (1), 1-6.
- [13] Dehinsilu, O.A., Odentunde, O.S., Usman, M.A., Ogunyinka, P.I., Taiwo, A.I. and Onaneye, A.A. (2020). Solutions of Linear Convection-Diffusion Problems with Constant Coefficients Using Mahgoub Transform Method. *FUW Trends in Science and Technology Journal*, 5 (3), 891-894.
- [14] Abbas, E.S., Kuffi, E.A. and Abdllrasol, L.B. (2022). General Solution of Telegraph Equation Using Aboodh Transform. *Mathematical Statistician and Engineering Applications*, 71 (2), 267-271.
- [15] Aggarwal, S., Kumar, R. and Chandel, J. (2023). Solution of Linear Volterra Integral Equation of Second Kind via Rishi Transform. *Journal of Scientific Research*, 15 (1), 11-119.
- [16] Kuffi, E. and Maktoof, S.F. (2021). “Emad-Falih Transform” a new integral transform. *Journal of Interdisciplinary Mathematics*, 24 (8), 2381-2390.
- [17] Gupta, R. (2020). On Novel Integral Transform: Rohit Transform and Its Application to Boundary Value Problems. *ASIO Journal of Chemistry, Physics, Mathematics and Applied Sciences*, 4 (1), 08-12.
- [18] Aggarwal, S. and Chaudhary, R. (2019). A Comparative Study of Mohand and Laplace Transforms. *Journal of Emerging Technologies and Innovative Research*, 6 (2), 230-240.
- [19] Mushttt, I.Z., and Kuffi, E.A. (2023) Sadik and Complex Sadik Integral Transforms of System of Ordinary Differential Equations, *Iraqi Journal for Computer Science and Mathematics*, 4 (1), 181-190.
- [20] Mohand, M. and Mahgoub, A. (2017). The new integral transform “Mohand Transform”. *Advances in Theoretical and Applied Mathematics*, 12 (2), 113-120.
- [21] Aggarwal, S. and Chauhan, R. (2019). A Comparative Study of Mohand and Aboodh Transforms. *International Journal of Research in Advent Technology*, 7 (1), 520-529.
- [22] Kumar, P.S., Saranya, C., Gnanavel, M.G. and Viswanathan, A. (2018). Applications of Mohand transform for solving linear Volterra integral equations of first kind. *International Journal of Research in Advent Technology*, 6 (10), 2786-2789.

Turkish Classical Music Composition with LSTM Self-Attention

Ahmet KAŞİF ^{1*} , Selçuk SEVGEN ² 

¹ Bursa Technical University, Computer Engineering Department, Bursa, Turkey

² İstanbul University-Cerrahpaşa, Computer Engineering Department, İstanbul, Turkey

Abstract

Synthetic symbolic music generation, the process of creating new musical pieces using symbolic representations, has gained significant traction in the field of music informatics and computational creativity. It holds immense potential for various applications, ranging from music education and composition assistance to music therapy and personalized music recommendation systems. Classical Turkish music (CTM) exhibits distinct characteristics regarding Western Tonal Classical Music (WCTM) such as melodic organization, formation of rhythmic structure, or melodic expressions. This study tackles the challenge of symbolic music composition, focusing on CTM. Unlike its Western counterpart, CTM incorporates microtonal intervals. These intervals are smaller than the semitones in Western music, allowing for a more nuanced expression of pitch. This leads to a more diverse set of pitch ranges. The proposed method employs a combination of long-short term memory (LSTM) networks and self-attention encoding to capture long-term relational information and generate realistic CTM compositions. LSTMs effectively model sequential dependencies and improve local relations within musical structures, and self-attention improves the context vector, allowing the model to attend to different aspects of the musical context simultaneously. This combination enables the proposed method to generate compositions that are both musically coherent and stylistically consistent with distinct features of CTM. The proposed method was evaluated on two datasets, the SymbTr dataset and Classical Music Piano (CPM) dataset. The assessment of musical contents is evaluated through melodic similarity and stylistic consistency metrics. The results demonstrate that the proposed method is able to generate musical content that is coherent and to produce music that is pleasing-to-hear. Overall, the article presents a novel and effective approach to symbolic music composition, focusing on CTM.

Keywords: Music-Generation, Deep Learning, LSTM, Self-Attention, Music Information Retrieval, Turkish Classical Music.

Cite this paper as: Kasif A. and Sevgen S. (2024). Turkish Classical Music Composition with LSTM Self-Attention, 8(1):25-35.

*Corresponding author: Ahmet KAŞİF
E-mail: ahmet.kasif@btu.edu.tr

Received Date: 19/12/2023
Accepted Date: 01/02/2024
© Copyright 2024 by
Bursa Technical University. Available
online at <http://jise.btu.edu.tr/>



The works published in the journal of Innovative Science and Engineering (JISE) are licensed under a Creative Commons Attribution-NonCommercial 4.0 International License.

1. Introduction

The emergence of synthetically generated music has revolutionized the field of music informatics, offering unprecedented opportunities to expand musical diversity, enhance creativity, and personalize music experiences. However, generating music that adheres to the stylistic conventions and expressive nuances of a particular musical tradition remains a significant challenge. This study explores the intricate world of Classical Turkish Music (CTM), a rich musical heritage characterized by its unique microtonal ornamentation, intricate rhythmic patterns, and elaborate ornamental devices. Western classical tonal music (WCTM) gets the majority of attention in terms of generative musical analysis [1]. Yet, regional musical approaches such as CTM pose distinct possibilities and could provide major contributions to the musical world. While there are many similarities between these two musical approaches, some differences also exist. WCTM relies on half-steps as the primary melodic intervals while CTM embraces microtonal intervals, creating subtle pitch variations that add a distinctive flavour to its melodies [2-4]. Rhythmically, CTM showcases complex patterns with uneven subdivisions and syncopation, distinguishing it from the more predictable rhythmic structures of WCTM. Generating symbolic music that faithfully adheres to the rules and expressiveness of CTM presents several formidable challenges. Capturing the intricacies of microtonal intervals, accurately modelling complex rhythmic patterns, and incorporating the nuances of CTM's modal system are just a few of the hurdles that must be overcome. Additionally, ensuring stylistic consistency and achieving originality are crucial aspects of generating compelling CTM compositions. State-of-the-art methods in symbolic music generation have made significant progress, employing techniques such as recurrent neural networks (RNNs) and long short-term memory (LSTM) networks to capture long-term musical relationships and generate coherent compositions. However, these methods often struggle to fully capture the intricate details and expressive qualities of CTM. This study introduces the application of LSTM self-attention to symbolic music generation for CTM. Self-attention, a powerful technique in the field of natural language processing, enables the model to simultaneously attend to multiple aspects of the musical context, facilitating the capture of the subtle nuances and expressive details that characterize CTM. By incorporating self-attention, the proposed method aims to overcome the limitations of traditional symbolic music generation techniques and produce high-quality CTM compositions that accurately reflect the stylistic conventions and expressiveness of the tradition. To evaluate the effectiveness of the proposed method, two datasets are employed: the SymbTr dataset and the Classical Music Piano (CPM) dataset. The SymbTr dataset provides a comprehensive collection of CTM melodies annotated with microtonal intervals and rhythmic information [5]. The CPM dataset offers a diverse range of Western classical music pieces for comparison and evaluation [6]. The proposed algorithm holds significant promise for advancing the field of symbolic music generation and fostering a deeper appreciation for CTM. By generating high-quality CTM compositions, this research can contribute to the preservation and revitalization of this rich musical heritage, expanding the boundaries of musical creativity and enriching the musical landscape. The main contributions of this study are as follows:

- We demonstrate that LSTM-self-attention networks can effectively capture long-term relational information in classical Turkish symbolic musical sequences.
- We show that attentional networks can tackle the musical content generation problem on musical contents other than Western Tonal Music and provide new ways to integrate state-of-art knowledge on local musical approaches.

- We analyse the performance of attentional networks in different architectural configurations and provide a comparative study for future symbolic music generation research on CTM.

The rest of this study is organized as follows: section two provides a detailed analysis of the state of art in musical content generation and summarizes the methods with a comparative manner. Section three covers the presentation of the datasets, conducted input preprocessing steps and the experimental environment followed by the detailed expression of the proposed method and the evaluation metrics. Section four provides the results of assessment analysis. The study is concluded in section five with a discussion of the paper as well as future works.

2. Literature Review

With its distinct melodic structures called maqam as well as monophonic nature and unique rhythmic features, CTM presents a sonic realm distinct from its Western counterpart. This distinctiveness has posed a significant challenge for Music Information Retrieval (MIR) research, particularly in the domain of generative modelling. While numerous musical forms have served as fertile ground for MIR investigations, publicly available datasets dedicated to CTM have remained scarce. However, the emergence of SymbTr, boasting over two thousand MIDI-encoded pieces, marks a pivotal moment in facilitating comprehensive research endeavors [4]. This valuable resource has already fuelled explorations in areas such as music recommendation systems and maqam classification, demonstrating its potential to unlock further insights into the complexities of CTM [7, 8]. Still, the applications on generative domain for CTM is not properly analysed and lacks attention.

The current MIR research is conducted on two major fronts called signal domain and symbolic domain. The symbolic music research requires a high-level representation of musical features such as MIDI encoding to provide a more human-readable format to operate [1]. This representation provides a clear temporal structure. Noteworthy studies for symbolic music generation have highlighted that the use of RNNs and their variations such as LSTMs and Gated Recurrent Unit networks (GRU) produce satisfying results on modelling of short-term sequences but fail to accommodate their performance as the sequence length increases [9-11].

The advent of attention mechanisms marked a game-changer, initially demonstrating remarkable success in applications within Natural Language Processing (NLP) [12, 13]. This success has quickly been translated to other domains, including symbolic music research, where attentional networks have brought forth the possibility to improve modelling of the salient features within musical sequences, leading to significant advancements in tasks like maqam classification and sequence prediction [14, 15].

With the emergence of Deep Learning, significant research has been conducted to explore the characteristics of the Western Tonal Music. However, the distinct nature of CTM made it difficult to apply the gained knowledge to its domain. Thus, there has been only a handful of research in terms of generative modelling in Turkish Music, much less in CTM. Tanberk and Tukul proposed a combined CNN-LSTM network to generate Turkish pop music using a collected dataset which can provide style-specific content [16]. Aydingun et. al used a collected Classical Turkish Music dataset which again consists of 20 pieces to generate Turkish songs with lyrics [17]. Both studies use small-sized collected datasets and do not offer benchmark results for music generated musical content.

3. Materials and Methods

3.1. Dataset Description

SymbTr and CPM, two symbolic datasets, are employed in the proposed music synthesis analysis. Both datasets consist of MIDI-encoded files. The SymbTr dataset contains around two thousand pieces for Turkish maqam music, which is the focus of exploration for the study. The CPM dataset contains piano compositions for Western tonal music and contains around 200 musical files. Both datasets are parsed as monophonic music sheets. Chords are parsed as notes, using the base note of the chord as the pitch symbol. The CTM dataset yields less sequences for training than CPM counterpart dataset as the majority of pieces are shorter than pieces in CPM. The summary of features of both datasets are given in Table 1.

Table 1. Data Analysis for SymbTr and CPM datasets

Dataset	SymbTr	CPM
Number of Pieces	1931	221
Number of Unique Pieces	33	85
Number of Unique Durations	48	51
Number of Prepared Input Sequences	48.2k	300k
Average / Maximum Piece Length	325 / 1467	709 / 4312

The MIDI format includes valuable information but cannot be directly supplied to deep learning architecture as an input line. Therefore, the pieces in the datasets are preprocessed using "music21" music processing library into an array-type format [18]. Two features (pitch, duration) are extracted from the pieces. Pitch indicates the frequency class of the played sound and demonstrates a categorical feature. The second feature, duration, is the playing duration for the respective note and is a numerical feature.

3.2. Experimental Environment

The proposed model was developed using Python 3.9.7 and Tensorflow/Keras 2.11.0. A Grid-Search technique was used to optimize the hyperparameters on a computer cluster at the B.T.U High-Performance Clustering Laboratory (HPCLAB). The computers on the BTU-HPCLAB cluster have *Intel® Core™ i9-10900X* CPUs and Nvidia 3090 GPUs. We have employed the CPUs to prepare, preprocess, and analyze the data, and the GPUs to train the model. Two GPUs are utilized simultaneously to accelerate the training process.

3.3. Input Preprocessing

The mapping from MIDI files to a symbolic music dataset requires multi-step preprocessing, which includes the parsing of musical files, decoding temporal information, mapping the note-level data to symbols, and normalization and preparing sequences. We have used Music21 to parse and decode MIDI files. Music21 is a powerful open-source tool which can represent and process various musical formats including MIDI with rich set of musical analysis tools [19]. Pitch and octave values for a single note is then processed together into a pitch symbol, and duration is encoded as a numerical value with a four-digit precision. Temporal input sequences data is constructed from the array data containing symbolic pitch and numerical duration values. The availability of much larger sequences in the CTM dataset gets lower after sequence length threshold of 64, which would hinder the training and also generative performance of the framework. Thus, sequence length of 64 notes has been utilized. The values

for the duration feature have been normalized, using min-max normalization [20]. Min-Max normalization is a technique which maps a given array of numerical values. The minimum element is mapped to zero, and the maximum element is mapped to one.

3.4. Proposed Method

The proposed method consists of a recurrent layer to model temporal musical data as well as a self-attention layer to improve the context vector for longer sequences. The recurrent layer accepts the input features and provides an encoded context vector. The context vector is then supplied into a self-attention module where important relations between notes are emphasized. The proposed DL model architecture is depicted in Figure 1. Two input vectors (note, duration) are supplied to the framework which are embedded by using a dedicated embedding layer. Both embeddings are then concatenated into a one single vector. The combined vector is modelled in two consecutive LSTM layers to create a context vector. This vector is then employed in a self-attention layer to improve the range of relations as well as to weight the important relations. The proposed self-attention layer is the standard self-attention configuration.

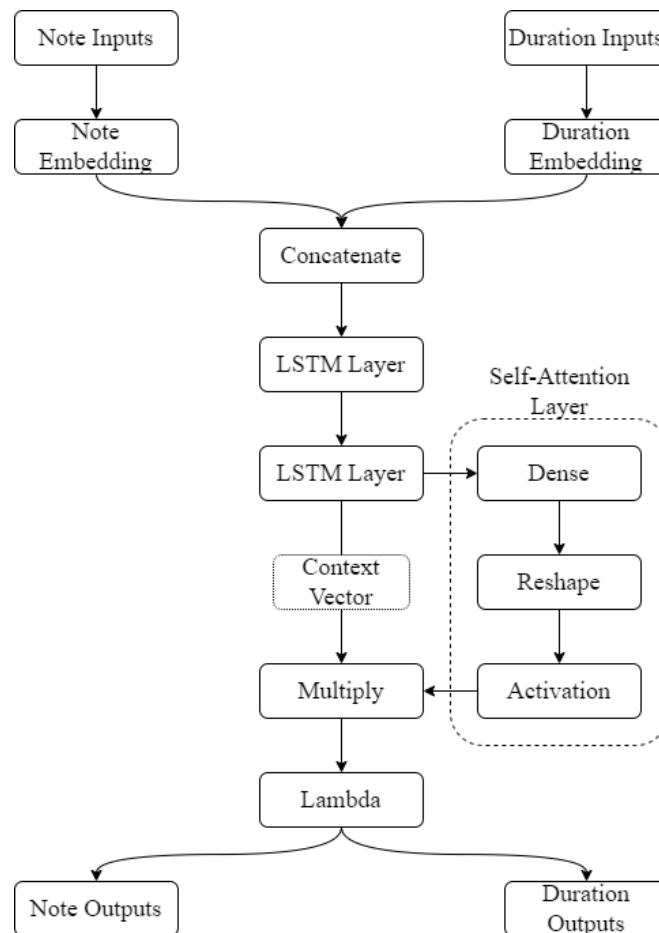


Figure 1. Proposed LSTM Self-Attention Model Architecture

3.5. LSTM Layer

LSTM networks are a type of RNNs with the addition of a memory cell. The most major concern of RNN is that while they are powerful in short sequences, the performance degrades as the length of sequence increases [21]. The cause of this is called vanishing gradients. The gradients fade as the information has to propagate through the temporal network. The LSTM cell improves the information flow through sequences and enables more accurate

representation of much longer sequences.

LSTM neurons consist of three gates and a cell state. Cell state is the memory unit of an LSTM neuron which runs information through an entire chain of LSTM layer. LSTM gates are responsible for data manipulation through cell states. The new information enters an LSTM neuron through input gate. The gate selectively adds new information to the cell state. The forget gate decides on the importance of information existing on cell state and discards if the information is found irrelevant. The output gate produces an output for the LSTM neuron based on cell state.

Self-attention networks improve the context vector of RNNs and provide stronger relations between more distant points in a sequence. The context vectors produced by RNN layers provide a relational information between notes, but this relational information weakens due to the mathematical nature of the function and yields a loss of gradients. This loss enlarges as the distance between notes get longer.

The self-attention employs 3 matrices (Q, K, V) to overcome the effect of loss of long-term dependencies and provide more direct relations between distant points in sequences. This mechanism has been one of the most important features in the success of Transformers architectures [22]. The vector Q stands for query vector, K stands for key vector, and V stands for value vector.

Query vectors represent the questions the model asks about each element in the input sequence. Key vectors represent the answers to the questions provided by the query vector and increase weights of attention from more related questions. Value vectors represent the actual information and are used to build the context-aware representation based on the attentive scores calculated by using query and key vectors.

The attention score is calculated with the help of the dot product of the query and key vectors as shown in equation 1. The scores are then normalized in equation 2, using a softmax function to create a probability distribution over the elements of the sequence. Finally, the normalized attention weights are employed to weight the value vectors and provide a weighted sum in equation 3. The produced output represents the context-aware encoding of the element with respect to the query.

$$\text{Attention Scores} = \frac{QK^T}{\sqrt{d_K}} \quad (1)$$

$$\text{Attention Weights} = \text{softmax} * \text{Attention Scores} \quad (2)$$

$$\text{Context} = \text{Attention Weights} * V \quad (3)$$

3.6. Evaluation Metrics

Throughout the deep learning (DL) algorithm's training phase, Root Mean Square Error (RMSE) metric is employed to assess the model's performance. The metric gauge distance-based approximation and has a track record of effectively refining mathematical problems. As shown in Equation 4, a smaller RMSE value denotes a closer match between the original and artificially generated content. Essentially, RMSE offer crucial insights into the DL algorithm's performance, enabling adjustments and enhancements to the model.

$$RMSE = \sqrt{\frac{1}{N} * \sum_{L=1}^N (Y_p - Y_c)^2} \quad (4)$$

4. Result and Discussion

Qualitative experiments are conducted through employment of proposed assessment metrics, and yielding model training scores are depicted in Table 2. The first three columns show the training loss values for CTM analysis, while the last three rows depict the training loss values for WCTM analysis. Hyper-parameters are fixed amongst compared methods for training phase. Both the baseline models and the proposed model were trained for 50 epochs, batch sizes were decided as 256, all methods employed two LSTM layers (RNN layers for the RNN-only architecture) with 128 neurons for each layer, optimizer was selected as RMSProp, and optimizer learning rate was set to 0,001. These hyperparameters were found to be yielding best results with minimal computational complexity. The hyperparameter search was conducted using Grid-Search method, which effectively looks up for all possible combinations of hyperparameters. The hyperparameter search space is given in Table 3.

The training loss analysis yields comparable results in case of both datasets. The duration loss contributes less to total loss compared to pitch loss as the duration loss is encoded using numerical representation. The total loss is calculated by using a weightless sum of pitch loss and duration loss. Evaluation of the proposed LSTM Self-Attention method against baseline methods in training phase results in better loss values in terms of all metrics. The baseline LSTM shows better overall performance against baseline RNN, but both baseline methods (RNN and LSTM) fall back against the proposed method in terms of loss metrics in training performance.

Table 2. Model performance regarding objective metrics, first 3 columns for CTM, last 3 columns for WCTM

Assessment Type	Methods	RMSE(Pitch)	RMSE(Duration)	RMSE (Total)
CTM Assessment	RNN	0.938	0.004	0.942
	LSTM	0.619	0.002	0.621
	LSTM Self-Attention	0.00022	0.00002	0.000024
WCTM Assessment	RNN	0.816	0.003	0.819
	LSTM	0.524	0.002	0.526
	LSTM Self-Attention	0.00024	0.00001	0.000025

Table 3. Hyperparameter search space

Hyperparameter	Search Space	Best Fit
Layer Neuron Count	[32, 64, 128, 256, 512]	128
Optimizer Selection	[RMSProp, Adam]	RMSProp
Optimizer Learn Rate	[0,01-0,0001]	0,001
Batch Size	[64, 128, 256, 512, 1024]	256

The feature-level loss curves for the total loss, pitch loss, and duration loss as well as all losses for CTM assessment are given in Figure 2. The loss curves show that the sharp decrease on the first epochs is supported with the continuous improvement over the remaining epochs, finally reaching a plateau. This behavior shows that the model has executed a healthy training process. Comparing the feature-wise loss curves, the pitch loss possesses the highest complexity and contributes the most to total loss as it is encoded as a categorical feature.

A musical piece generated by the proposed LSTM Self-Attention is depicted by using Western musical notation in Figure 3. The generated piece is 96 notes long. The piece shows a descending melodic line along with the use of perfect fourth, which is a common approach in many maqams of CTM. Also, the rhythmic development poses

characteristic features of CTM.

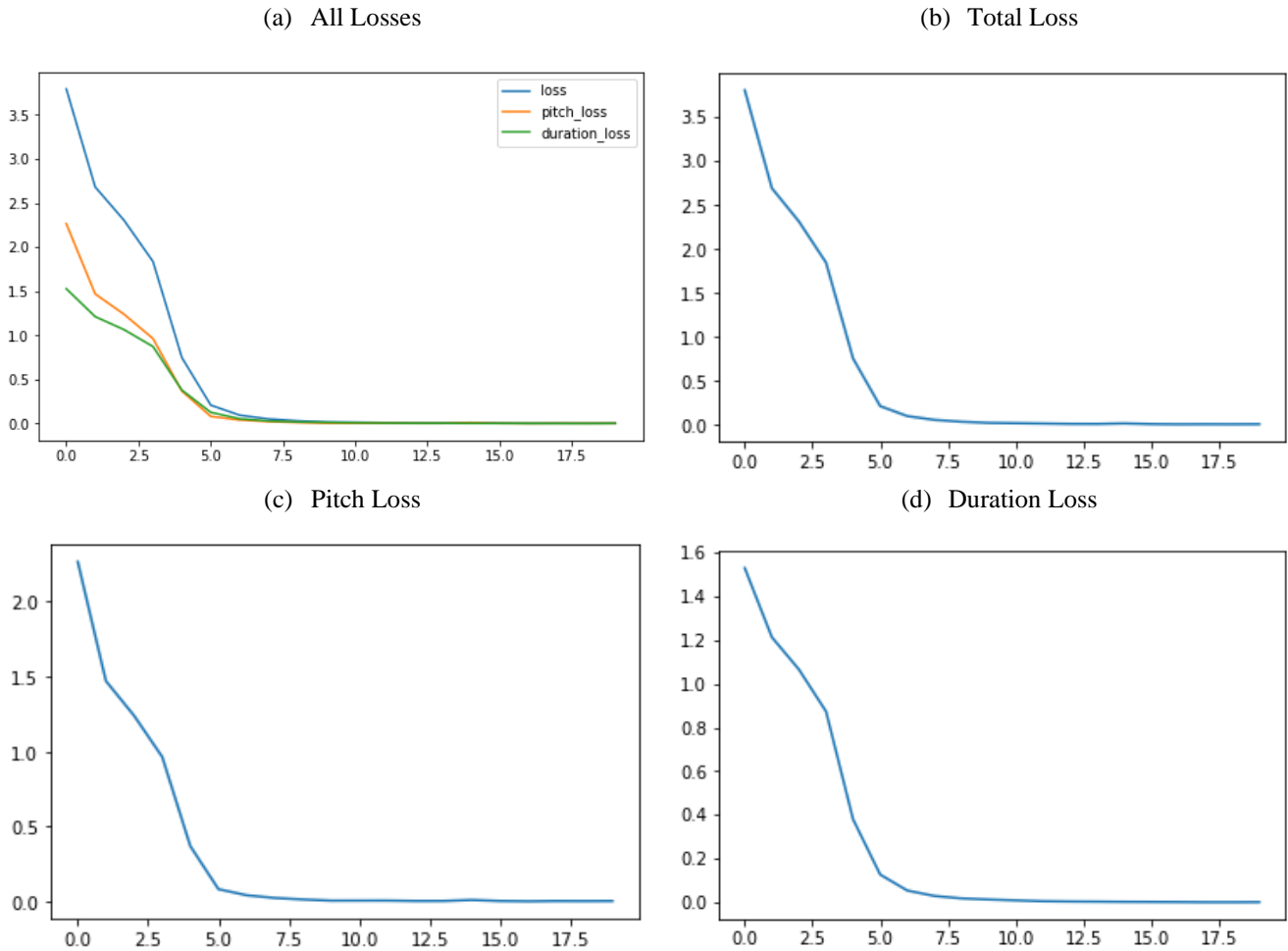


Figure 2. Proposed LSTM Self-Attention Model Training Loss Curves (a) All Losses, (b) Total Loss, (c) Pitch Loss, (d) Duration Loss

The melody starts with a quick flurry of notes in the first measure, followed by slower, sustained notes in the next two measures. This creates a sense of contrast and dynamism, but it is still a simple pattern compared to the intricate rhythmic interplay and layering often found in Turkish music. The representation of rhythmic features using a duration object provides a simple solution, yet it provides a room for improvement for future works. A more complex representation would be addressed to cope with the high-variational tempo characteristic of CTM.



Figure 3. Synthetic CTM piece generated with the proposed method of LSTM Self-Attention

5. Conclusion

Synthetic symbolic music generation has emerged as a promising avenue within music informatics and computational creativity, offering the promising prospect of emulating and potentially even surpassing human compositional capabilities. This study specifically delves into the realm of Classical Turkish Music (CTM), woven from intricate melodic structures, dynamic rhythmic tapestry, and a microtonal palette that expands the expressive boundaries of pitch. Unlike its Western Tonal Classical Music (WCTM) counterpart, CTM bends the rigidity of major and minor scales, instead embracing the fluidity of maqams with their unique modal configurations and expressive microtonal nuances. These maqams, with their intricate ornamentation and characteristic melodic contours, paint a sonic landscape with emotional depth and increased expressive potential. This interplay of maqams and rhythms creates a rich set of musical possibilities, demanding a model capable of capturing both the long-term melodic coherence and the nuanced rhythmic details that define CTM. To meet this challenge, we propose a novel approach that leverages the combined strengths of LSTM and self-attention networks. Self-attention mechanisms, inspired by recent advances in natural language processing, empower the model to "pay attention" to various musical elements within the sequence simultaneously, allowing it to grasp the subtle interplay between maqams, rhythms, and individual notes. LSTM networks, on the other hand, excel at capturing long-term dependencies within the musical sequence, ensuring the generated compositions exhibit a smooth flow and melodic coherence. The efficacy of this approach is evident in the generated CTM pieces, which showcase a remarkable level of musical coherence and stylistic consistency. Evaluated against established SymbTr and CPM datasets, our method not only demonstrates its ability to produce musically pleasing compositions, but also sticks to the stylistic nuances that define CTM. Quantitative metrics confirm that our generated compositions successfully capture the essence of CTM and resonate with the listener's expectations of this genre. The proposed method not only contributes to the field of music informatics by advancing the state of the art in symbolic music generation, but also

opens new doors for exploring the diversity and complexity of CTM. Future research can leverage this work as a springboard to delve deeper into the theoretical underpinnings of CTM and develop even more sophisticated models capable of capturing the full spectrum of its expressive potential. The effect of using musical features such as volume and tempo can be investigated to obtain richer representations. By doing so, we can not only preserve and celebrate this treasured musical heritage but also pave the way for exciting new artistic creations that draw inspiration from its rich and timeless beauty.

References

- [1] Briot, J. P., & Pachet, F. (2020). Deep learning for music generation: challenges and directions. *Neural Computing and Applications*, 32(4), 981-993.
- [2] Bozkurt, B., Gedik, A. C., & Karaosmanoglu, M. K. (2009, April). Music information retrieval for Turkish music: problems, solutions and tools. In *2009 IEEE 17th Signal Processing and Communications Applications Conference* (pp. 804-807). IEEE.
- [3] Kızrak, M. A., & Bolat, B. (2017). A musical information retrieval system for Classical Turkish Music makams. *Simulation*, 93(9), 749-757.
- [4] Karaosmanoğlu, M. K. (2012). A Turkish makam music symbolic database for music information retrieval: SymbTr. In *Proceedings of 13th International Society for Music Information Retrieval Conference; 2012 October 8-12; Porto, Portugal. Porto: ISMIR, 2012.* p. 223–228. International Society for Music Information Retrieval (ISMIR).
- [5] Krueger, B. Classical piano midi page (2016). URL: <http://www.piano-midi.de/>(Last accessed 28/11/2023).
- [6] Ay, G., & Akkal, L. B. (2009). İTÜ Türk Musikisi Devlet Konservatuvarı Türk müziğinde uygulama-Kuram sorunları ve çözümleri. *Uluslararası çağrılı kongre bildiriler kitabı*.
- [7] Öztürk, Ö., Özacar, T., & Abidin, D. (2018, September). KORAL: Türk Müziği için Makam Tabanlı Öneri Motoru Tasarımı. In *2018 International Conference on Artificial Intelligence and Data Processing (IDAP)* (pp. 1-4). IEEE.
- [8] Abidin, D., Öztürk, Ö., & Öztürk, T. Ö. (2017). Klasik Türk müziğinde makam tanıma için veri madenciliği kullanımı. *Gazi Üniversitesi Mühendislik Mimarlık Fakültesi Dergisi*, 32(4), 1221-1232.
- [9] Mangal, S., Modak, R., & Joshi, P. (2019). LSTM based music generation system. *arXiv preprint arXiv:1908.01080*.
- [10] Shah, F., Naik, T., & Vyas, N. (2019, December). LSTM based music generation. In *2019 International Conference on Machine Learning and Data Engineering (iCMLDE)* (pp. 48-53). IEEE.
- [11] Wu, J., Hu, C., Wang, Y., Hu, X., & Zhu, J. (2019). A hierarchical recurrent neural network for symbolic melody generation. *IEEE transactions on cybernetics*, 50(6), 2749-2757.
- [12] Vaswani, A., Shazeer, N., Parmar, N., Uszkoreit, J., Jones, L., Gomez, A. N., ... & Polosukhin, I. (2017). Attention is all you need. *Advances in neural information processing systems*, 30.
- [13] Niu, Z., Zhong, G., & Yu, H. (2021). A review on the attention mechanism of deep learning. *Neurocomputing*, 452, 48-62.
- [14] Wu, J., Liu, X., Hu, X., & Zhu, J. (2020). PopMNet: Generating structured pop music melodies using neural networks. *Artificial Intelligence*, 286, 103303.
- [15] Muhamed, A., Li, L., Shi, X., Yaddanapudi, S., Chi, W., Jackson, D., ... & Smola, A. J. (2021, May). Symbolic

- music generation with transformer-gans. In Proceedings of the AAAI conference on artificial intelligence (Vol. 35, No. 1, pp. 408-417).
- [16] Tanberk, S., & Tükel, D. B. (2021, January). Style-specific Turkish pop music composition with CNN and LSTM network. In 2021 IEEE 19th World Symposium on Applied Machine Intelligence and Informatics (SAMI) (pp. 000181-000185). IEEE.
- [17] Aydingün, A., Baglu, D., Canbaz, B., & Kökbıyık, A. Derin Öğrenme ile Türkçe Sarkı Besteleme Turkish Music Generation using Deep Learning.
- [18] Cuthbert MS, Ariza C (2010) music21: A toolkit for computer-aided musicology and symbolic music data. Proceedings of the 11th International Society for Music Information Retrieval Conference (ISMIR 2010).
- [19] Cuthbert, M. S., & Ariza, C. (2010). music21: A toolkit for computer-aided musicology and symbolic music data.
- [20] Patro, S.G.K, & Sahu, K. K. (2015). Normalization: A preprocessing stage. arXiv preprint arXiv:1503.06462.
- [21] Hochreiter, S. (1998). The vanishing gradient problem during learning recurrent neural nets and problem solutions. *International Journal of Uncertainty, Fuzziness and Knowledge-Based Systems*, 6(02), 107-116.
- [22] Lin, T., Wang, Y., Liu, X., & Qiu, X. (2022). A survey of transformers. *AI Open*.

Using Time Series Models in Product Based Order Forecasting

Fatih Yücalar^{1*} 

¹ Manisa Celal Bayar University, Hasan Ferdi Turgutlu Faculty of Technology, Software Engineering, Manisa, Türkiye

Abstract

Production systems play a vital role in maximizing consumer satisfaction by efficiently transforming inputs such as labour, raw materials, and capital into products or services aligned with consumer demands. An order-based production takes place in poultry meat and meat products production facilities, which face various difficulties in meeting changing customer demands and managing the supply of raw materials. To optimize production and increase customer loyalty, these facilities use strategic scheduling, considering their daily production capacity and fluctuating customer orders. In this study, estimating which customer and product type the future order quantities will come from for the relevant facilities, increasing customer satisfaction by facilitating order processes and minimizing storage costs are discussed. With this study, the number of orders was estimated, and it was aimed to meet the orders in the most accurate way. In the estimations, the order data of a poultry meat and meat products production facility between 2013 and 2021 were used. Since the order figures will change every year in cases such as the customer working with the facility, growing, or shrinking, better results have been tried to be obtained with the arrangements made on the data set used and three different data sets have been obtained. Estimation processes were performed for these three data sets using LSTM and Prophet algorithms. While the RMSE value was 7.07 in the LSTM model in experimental studies, this value was obtained as 10.96 for Prophet. In the results obtained, it was observed that the arrangements made on the data set positively affected the accuracy of the estimations and the LSTM algorithm produced better results than the Prophet algorithm.

Keywords: Production optimization, Poultry production system, Time Series, LSTM, Prophet.

Cite this paper as: Yücalar F.(2024). Using Time Series Models in Product Based Order Forecasting, 8(1):36-52.

*Corresponding author: Fatih Yücalar
E-mail: fatih.yucalar@cbu.edu.tr

Received Date: 18/01/2024
Accepted Date: 24/02/2024
© Copyright 2024 by
Bursa Technical University. Available
online at <http://jise.btu.edu.tr/>



The works published in the journal of Innovative Science and Engineering (JISE) are licensed under a Creative Commons Attribution-NonCommercial 4.0 International License.

1. Introduction

The change in the management approach of the enterprises has also caused a change in the structure of the companies. To meet their needs, companies must adopt different approaches in their structures and management styles, but they also must use the developing modern production systems. A system within the enterprise may have many subsystems. However, this system can also constitute a subsystem of a larger-scale system. While marketing, management, accounting and finance, sales and human resources constitute the sub-systems within an enterprise, the enterprise constitutes the sub-system of the country's economy. In summary, production systems, which constitute the whole of activities that create value for the environment, constitute the subsystem of an enterprise.

Production systems are one of the important subsystems within a business or organization. A production system is a system in which products or services are produced by going through a certain transformation process of various inputs such as labour, raw materials, data, energy, and capital [1]. The main purpose of these systems is to maximize consumer satisfaction by providing the production of products or services in accordance with consumer demands. Production systems are classified into four different types: continuous, intermittent, mixed, and project-based [2]. In order-based production systems, which are a subclass of discrete production systems, the characteristics and quantity of the products to be produced are determined by order in line with the demands of the customers. From this point of view, order-based production is carried out in poultry meat and meat products production facilities. In these facilities, it is of great importance to meet the demands of the customers completely. However, to meet these demands, difficulties are encountered such as meeting the daily raw material supply from the poultry grown and obtaining only a certain amount of raw material from each product. Another challenge for poultry meat and meat products production facilities is that the animals that have reached sufficient maturity come to the slaughter and the sizes of the incoming creatures are not always the same. However, only certain products are obtained from each poultry in certain proportions. The density of orders from customers varies according to the day, and it can be a product that can be obtained at low rates from a poultry creature. To meet all incoming orders, the number of products that need to be stored in poultry meat and meat products production facilities will also increase. Due to the short shelf life of poultry products and the costly storage processes, poultry meat and meat products production facilities aim to meet the incoming orders in a way that the minimum level of products from the poultry that come to the slaughter is in stock.

Poultry meat and meat products production facilities have a certain daily production capacity. Due to the production capacity, restrictions are placed on the order days of the customers by the poultry meat and meat products production facilities. These restrictions may provide changes in cases such as the increase in the capacity of the poultry meat and meat products production facility, periodic changes, and increase in the number of customers. While meeting all the products ordered by the customer is an important factor, on the manufacturer's side, this means that the orders are balanced, and the product left over from the use of raw materials is the least. For this reason, an optimization process is applied by comparing the products ordered by the customer daily with the amount and kilograms of future poultry and making cuts to customer loyalty.

In the study, it is aimed to forecast customer orders daily with time series models with product breakdown, and to evaluate the orders coming to the poultry meat and meat products production facility earlier thanks to these estimations, and to meet more balanced and larger orders with the help of early actions. The customer and product

information in the order for every day plays a major role in the cuts and measures to be made. In order optimization studies, future order quantity estimation for a product is provided. In the study, customer and product breakdown estimations were made. In these estimations, the order days of each customer were determined, and their habits were monitored; the increase in the production capacity of the poultry meat and meat products production facility and the restrictions that the facility will bring to the customer side were evaluated and historical data was organized. In the literature reviews, it has been determined that there are not many case studies related to product-based order estimation from poultry. In a study conducted by Kozaklı *et al.* [3], it was observed that the monthly production amounts for 2021 were modelled by the time series method by using the monthly broiler production numbers obtained from the Turkish Statistical Institute. As a result of the modelling, it was estimated that 1353245283 broiler chickens should be produced for 2021 [3]. Another study showed that Thailand Industry made predictions for cooked chicken products exported to Japan using a Recurrent Neural Network (RNN) model [4]. Studies on forecasts for different sectors using Facebook Prophet [5] and Long Short-Term Memory (LSTM) [6] models were checked, their similarities and differences were determined, and they were adapted for this study. In the literature review, it has been seen that the relevant models are discussed in different areas such as order estimation of companies [7], estimating the electricity requirement of a country [8], vehicle spare part requirement estimation [9].

When the literature is reviewed, it is observed that there are many different studies on customer order forecasting. However, these studies are inadequate for poultry meat and meat products production facilities. The most important contribution of this study is to enable the prediction of daily customer orders and the fulfillment of incoming orders using product-specific time series models such as LSTM and Prophet for poultry meat and meat products production facilities.

2. Production Planning

Product planning incorporates all the decisions, steps, and tasks oriented internally that are essential for creating a successful product. In other words, it encompasses all actions that directly impact the product itself. On the other hand, go-to-market planning involves all the external steps taken to promote and market your product to the public. Production planning can be defined as a model that shows the production capacity of the company, the workforce, the optimum use of tools and equipment, and the amount and method of producing the desired product according to the possibilities and when [1]. In other words, production planning can be defined as “deciding in advance which product will be produced, when, how, where and by whom”. The main purpose of production planning is to plan and control the inputs and outputs of the enterprise, together with the optimum profit return, in line with the objectives of the companies. At this point, a structure is created that keeps elements such as production planning, customer demands, financing situations, production capacity under control [1]. Planning gives the firm the ability to think systematically and to make and implement decisions. The main reason for many problems is due to an unplanned management approach. Planning is the basic measure to prevent such problems from occurring. Production planning provides high efficiency in production targets. The high efficiency obtained enables to produce the demanded products at the desired time and with the lowest cost.

Production planning is a guide for factors such as quantity, duration, value, according to the goals and objectives of the company's production activities. For this reason, since it draws the attention of production managers to these

targets, it prevents waste of parameters such as labour and time and ensures that production is measured. The expected benefits from production planning can be listed as follows:

- to evaluate the factors of production according to appropriate criteria,
- to prevent production pauses and idle capacity,
- to reduce stock costs and prevent their increase by determining stock planning,
- to determine the balance between the production volume of the enterprise and customer demands,
- to determine production costs,
- to ensure that all the facilities of the company are used in line with the determined purposes.

3. Poultry Production System

An order-based mass production is applied in poultry production systems. The raw material obtained daily is provided from the animals grown. The height and size of these grown animals can vary. In production planning, it is not enough for poultry meat and meat products production facilities to have basic information about the poultry that will come to the daily slaughter, such as live maintenance and air temperature. Deaths experienced during the shipment of poultry to be slaughtered affect the number of raw materials to be included in the production planning and cause a decrease in the order fulfilment rate. Meeting the raw material needs in poultry production systems is provided from the poultry houses with which the poultry meat and meat products production facility is contracted. In the event that the chicks transferred to the relevant poultry houses reach certain maturity, the living creatures are sent to the poultry meat and meat products production facility and slaughtered for product production. After the transfer of poultry to the disinfected poultry houses of the producers, slaughter planning preparations begin. The slaughter planning process aims to meet the daily product need by transporting the chicks to the poultry meat and meat products production facility by vehicles after they reach a certain age.

The time for a normal poultry to reach sufficient maturity and size has been determined as 45 days [10]. In the feed policy supervised by the Ministry of Agriculture, the poultry that come to the slaughter must be fed the last three days before slaughter, which is called the finishing feed [11]. These poultry, which are sent to slaughter, are examined daily by veterinarians approved by the Ministry of Agriculture, and their Average Live Weight (ALW), ammonia burn [12], and hygiene information are collected. This collected information is then transmitted to the poultry meat and meat products production facility. ALW gives theoretical information about whether the poultry weighs enough for the product to be produced. Ammonia burn is the information that is caused by hygiene and affects the meat quality of the poultry. In case of high ammonia burn, the relevant poultry cannot be used in the production of some products and can be used for second-class products called B quality.

In production processes of poultry products, stocking time is limited due to shelf life [13]. Daily cuts are determined by live cut planning processes. Order needs are tried to be met according to the dimensions of the slaughtered poultry. Customer-based demands may differ on a daily or periodic basis. By giving different days to each customer, order restriction is ensured, and this need is tried to be met with planned cutting records. While raw material can be used as a product in poultry production, different products can be obtained by breaking the raw material. The products obtained from the crushed raw material were calculated proportionally from the poultry. Poultry shredding rates are given in Table 1.

Table 1. Poultry Shredding Rates

Type	Percentage
Chicken Breast	%48,36
Chicken Legs Hip	%39,97
Chicken Wings	%10,47
Other	%1,2

The stocking cost of the remaining products is high, and if they are not consumed from the stocks within two days, processed products (salami, sausage, doner, etc.) are obtained in the further processing factories. The main purpose in poultry meat and meat products production facilities is to use all poultry slaughtered during the day as product within the order and to leave the least product on the stock side. However, the products requested in the orders from the customers may cause an imbalance in different products. The case of an imbalance may cause excess products to remain in stocks. For this reason, incoming orders are evaluated, and cut-off processes are applied in a way that they can be met at the maximum level and that the least product is left in stock. In the optimization made to eliminate the imbalance and leave the least product in stock, the demanded products are brought to the balance by applying deduction processes according to customer loyalty. The graphics in Figure 1 and Figure 2 show the monthly incoming order quantities according to the product groups of the poultry meat and meat products production facility and the poultry kg information needed for these order quantities.

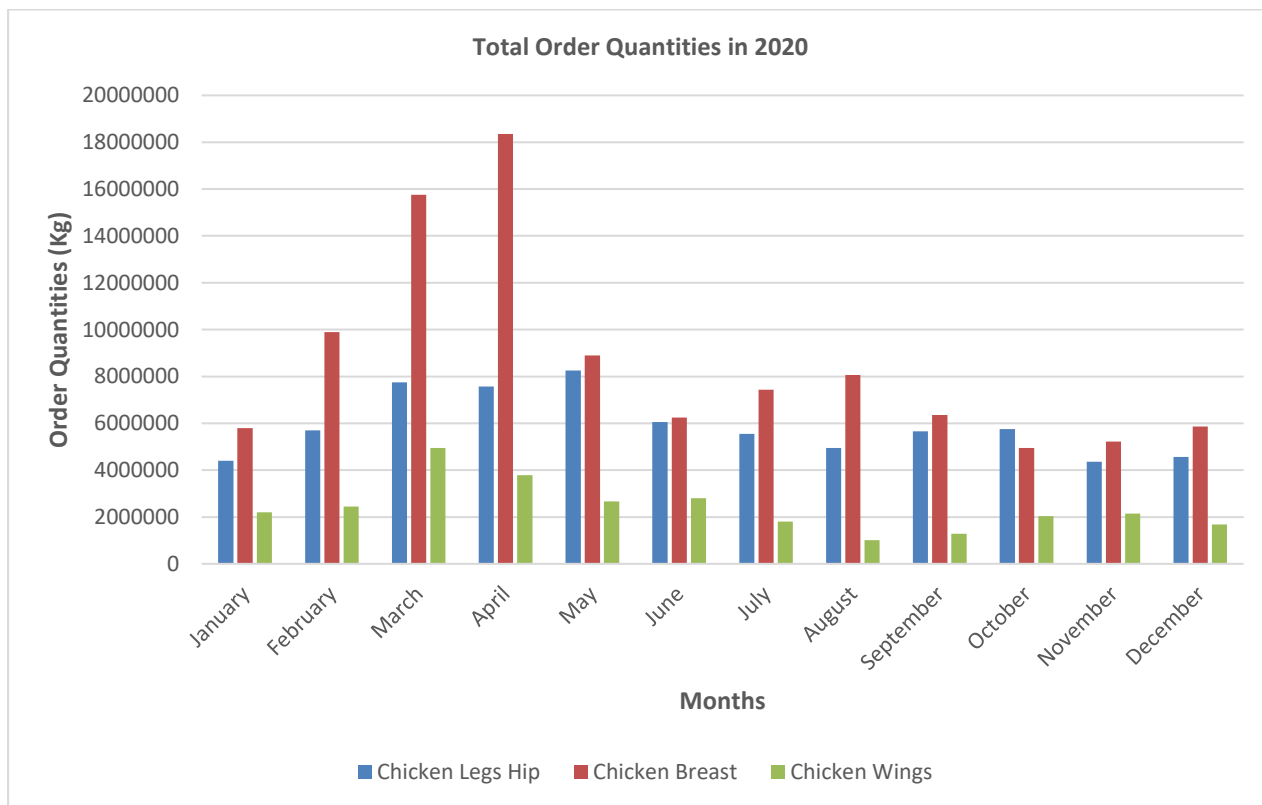


Figure 1. Total Order Quantities in 2020

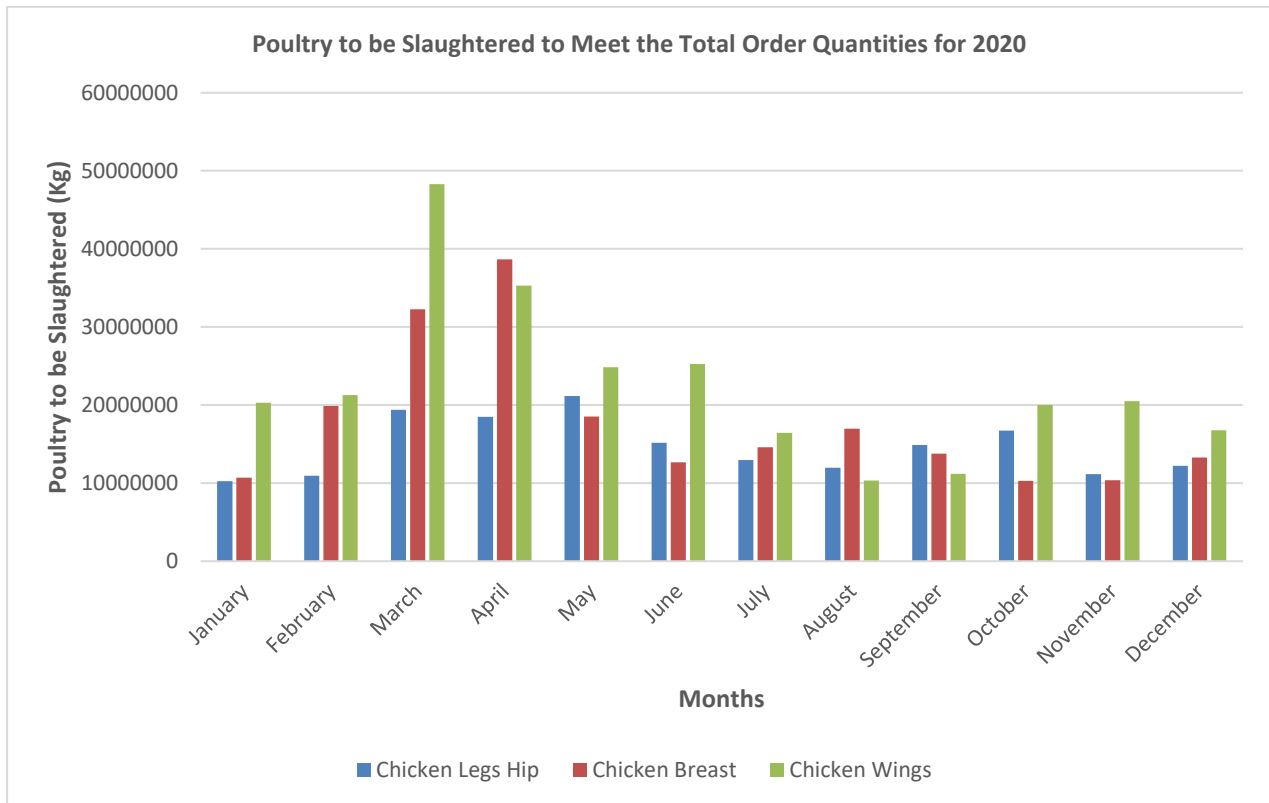


Figure 2. Poultry to be Slaughtered to Meet the Total Order Quantities for 2020 (Kg)

The ordered products change periodically, and if the products with the lowest shredding rate are ordered more, there are difficulties in meeting the orders.

3.1. Determination of Raw Material Requirement Quantity for an Order and Deduction Procedures

The raw material needed to produce an ordered product is obtained by dividing the ordered quantity by the ratio of the product type and completing it one hundred percent. In the event of fulfilling the order, the remaining raw materials can be used to fulfill orders in different product groups. However, if the density of the ordered products belongs to a single product group, it means that the products in the other product group cannot be used, and this is called an unbalanced order. The amount of raw material needed to meet the order is as much as the raw material of the product that will need the rawest material from the products in the order list. Calculation of raw material required quantity (RMRQ) is given in Equation (1).

$$RMRQ = \frac{Order\ Quantity\ (Kg) * 100}{Poultry\ Shredding\ Rate} \tag{1}$$

To give an example of this process, let the orders given by a customer be as in Table 2:

Table 2. Order Example

Product Group	Quantity
Chicken Legs Hip	100 Kg
Chicken Breast	50 Kg
Chicken Wings	50 Kg

According to the orders given in Table 2, in the preparation of the orders given by the customer:

- Chicken Legs Hip: $\frac{100*100}{39,97} = \sim 250 \text{ kg}$
- Chicken Breast: $\frac{50*100}{48,36} = \sim 103 \text{ kg}$
- Chicken Wings: $\frac{50*100}{10,97} = \sim 477 \text{ kg}$

Considering the maximum value among the obtained values, the amount of raw material required to meet the order will be determined. However, if this order is fulfilled, there will be a surplus for some product groups.

- $477 * \frac{48,36}{100} = \sim 230 \text{ kg Chicken Breast}$
Increased Chicken Breast: 230 kg – 50 kg = 180 kg
- $477 * \frac{39,97}{100} = \sim 190 \text{ kg Chicken Legs Hip}$
Increased Chicken Legs Hip: 190 kg – 100 kg = 90 kg

As a result, 180 kg of chicken breast and 90 kg of chicken legs hip will remain in excess. In case we make a 40% cut in the chicken wings order to optimize the order:

- Chicken Legs Hip: $\frac{100*100}{39,97} = \sim 250 \text{ kg}$
- Chicken Breast: $\frac{50*100}{48,36} = \sim 103 \text{ kg}$
- Chicken Wings (Amount of Deduction 40%): $\frac{50*100}{10,97} = \sim 273 \text{ kg}$

With the deduction for the chicken wing order:

- $273 * \frac{48,36}{100} = \sim 132 \text{ kg Chicken Breast}$
Increased Chicken Breast: 132 kg – 50 kg = 82 kg
- $273 * \frac{39,97}{100} = \sim 109 \text{ kg Chicken Legs Hip}$
Increased Chicken Legs Hip: 109 kg – 100 kg = 9 kg

As a result of the 40% cut for the chicken wing order, 82 kilograms of chicken breast and 9 kilograms of chicken legs hip increased. The less the amount of meat increased, the less the product remaining in the stock of the producer will be reduced, and the cost will also be reduced.

4. Methods and Tools

Daily order estimation was performed as a cumulative sum by querying separately for each customer and product information that has the right to order. Time series models are used for order forecasting processes. Time series forecasting stands as an extensively employed data science technique in sectors such as business, finance, supply chain management, production, and inventory planning [14]. Many estimation problems involve a temporal element, necessitating the estimation of time series data. Time series prediction is also a crucial domain in machine learning and can be approached as a supervised learning problem. Machine learning techniques like regression, neural networks, and support vector machines are applicable for time series predictions [15]. Time series

forecasting aims to predict future value over a given period of time [16]. It is used to guide future strategic decisions by developing models based on previous data and making observations with these models [17]. LSTM and Facebook Prophet are the most preferred models for order forecasting processes.

4.1. Long Short-Term Memory Algorithms

Long Short-Term Memory (LSTM) Networks are an artificial Recurrent Neural Network (RNN) architecture used to predict time series data [18, 19]. LSTM has the ability to retain long-term time-dependent information and the optimal hyperparameters of the network [20]. In the RNN, LSTM utilizes the memory cell to resolve long-term dependencies between data blocks of time series provided in the dataset. LSTM endeavours to overcome the difficulties by acquiring an accurate forecasting model and giving consideration to the intrinsic properties of the time series model. Also, one of the main advantages of LSTM is its ability to capture nonlinear patterns in time series data. At the data cleaning point, the LSTM algorithm focuses on replacing the missing values using appropriate techniques to correct the data string that is noisy and contains missing values. LSTM's have feedback links. In addition to image data, they can process all data sequences such as speaking or video. A standard LSTM network comprises distinct memory blocks called cells [21]. Two states, namely the cell state and hidden state, are transmitted to the subsequent cell. These memory blocks are responsible for retaining information. There are three main mechanisms in the LSTM structure: input gate, output gate and forget gate [22]. Figure 3 shows the LSTM structure [23].

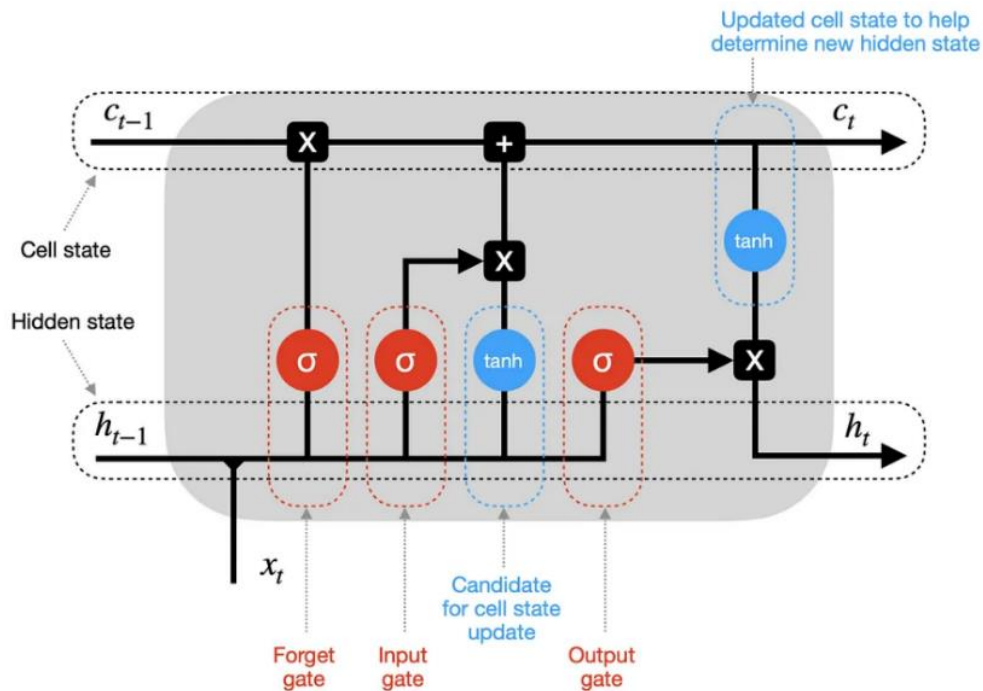


Figure 3. Structure of LSTM

In equations related to LSTM, these gates are i , o , and f ; the operational memories of the network are denoted by the terms C and \tilde{C} . The cell remembers the values in the memory blocks, and these three gates regulate the flow of information entering and leaving the cell [24]. The LSTM estimation processes, which include the terms in Table 3, are explained in three steps.

Table 3. LSTM terms

Term	Definition
σ	Sigmoid function
h_{t-1}	Previous hidden state vector
c_{t-1}	Previous cell state vector
x_t	Input vector to the LSTM unit
c_t	Cell state vector
h_t	Hidden state vector

Step 1 – Forgetting doors that are not needed: Each input is associated with its respective weighted LSTM unit. In nonlinear transformations, the sigmoid activation function takes a value between 0 and 1. Information after processing, information in the storage memory unit is processed by c_{t-1} . The input operation regulates the transfer of information from the previous period in the storage memory unit. It outputs x_t of the current state and h_{t-1} of the previous state and analyses the historical output to decide which partitions to delete. For instance, in the case of an entry such as “Arya has a baby,” the name “Zeynep” may be forgotten since the subject is Arya. The gate is referred to as the forget gate f_t and the gate output is determined as $f_t \times f_{t-1}$ [6].

Step 2 – Identifying and saving the newly entered x_t entry in the memory unit: By utilizing the sigmoid function, the decision to update or ignore new entries is made. Using the tanh function, new values are inputted, and the input updated to create vectors of all possible values. This new entry is added to the previous cell state vector (c_{t-1}) to obtain the cell state vector (c_t) [6].

Step 3 – Determining the output content: The memory unit computes all potential values through the tanh function, after which the matrix gets multiplied by the output of the *sigmoid* function. The hyperbolic tangent function is applied to non-linearly transform the updated value, and then the dot product determines whether the value will be smoothly output after the control calculation. For instance, when predicting blank words, the model leverages the names associated with "teacher" in memory, enabling it to promptly respond to the word "teach". It does not give a direct answer to the model but provides long-term learning outcomes [6].

LSTM alleviates the vanishing gradient problem stemming from the hindrance of backpropagation in RNNs [22, 29]. LSTM networks use gated mechanisms that enable continuous error flow to overcome the vanishing gradient problem encountered by RNNs. Thanks to its ability to learn long-term dependencies and maintain long-term memory in complex multivariate time series containing patterns of varying lengths, it eliminates the need for a predefined time window. The LSTM networks, formed as a result of stacking recurrent hidden layers sequentially, enable the processing of time series data at different time scales and the acquisition of a richer set of temporal features.

4.2. Facebook Prophet Algorithms

Prophet is an open-source algorithm introduced by Facebook in February 2017 for generating time series models [25]. Prophet was designed to tackle common challenges at Facebook, such as predicting user activity across different parts of their application or prioritizing feature development. This algorithm enables data analysts and data scientists to perform fast, powerful, and accessible time series modelling. It is well suited for scheduling forecasting challenges for extended events (longer events like school holidays) or special events (one-day events

like Black Friday) [26].

When compared to certain traditional time series methods, Prophet is known for being simpler and more user-friendly. Because it covers the Python and R language interfaces, a Python predictive analysis environment can be easily created for time series analysis [25]. These benefits that Prophet has provided illustrate why it is popular with data scientists who actually work on demand forecasting. The time series model in Equation (2) basically consists of the sum of three-time functions (growth: $g(t)$, seasonality: $s(t)$, holidays: $h(t)$) and a noise term (ε_t).

$$y(t) = g(t) + s(t) + h(t) + \varepsilon_t \tag{2}$$

The growth function is used to model the overall trend of the data. The growth trend in the data can be present at all points or modified at change points. The seasonality function, weekly, monthly etc. is a simple Fourier Series used as a function of time to represent periodic changes. The holiday function allows to make time estimations for changes related to special reasons such as holidays and festivals. Finally, ε_t represents the noise term [25].

$$g(t) = \frac{c}{1 + e^{(-k(t-b))}} \tag{3}$$

In Equation 3, $g(t)$ is a logical function; where c representing the capacity of the model, k representing the growth rate and b representing the offset [25].

$$s(t) = \sum_{n=1}^N \left(a_n \cos \frac{2\pi n t}{T} + b_n \sin \frac{2\pi n t}{T} \right) \tag{4}$$

In Equation 4, $s(t)$ denotes the periodic term that uses the Fourier series to estimate the periodic component. In this equation, T is the period and $2n$ is the expected number of cycles to be used in the model [25].

$$h(t) = \sum_{i=1}^L K_i 1(t \in D_i) \tag{5}$$

$$Z(t) = [1(t \in D_1), \wedge, 1(t \in D_2)] \tag{6}$$

$$h(t) = Z(t)\kappa, \kappa \sim Normal(0, v) \tag{7}$$

$h(t)$ allows a time estimation to be made, considering the probability that a holiday or an event will change in the future. In Equation 5, K_i denotes the effect of holidays in the period on the predicted value and D_i stands for the fourth dummy variable. If the time variable t belongs to the dummy variable, the dummy variable takes a value of 1; otherwise, it takes a value of 0. i represents the holiday, D_i represents the time t included in the window [25]. The working principle of the forecasting process used in Facebook Prophet is given in Figure 4.

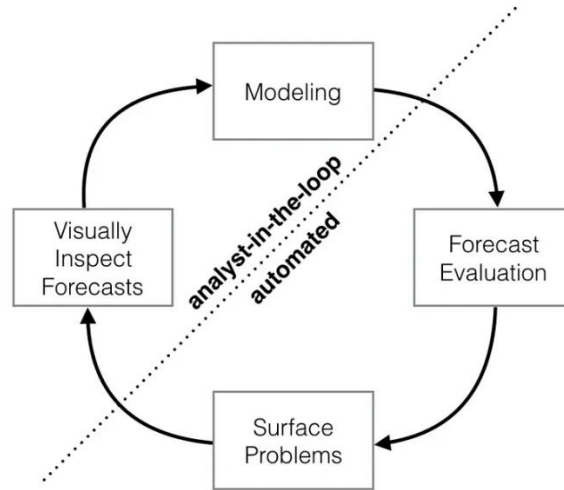


Figure 4. Forecasting Process in Facebook Prophet

4.3. Performance Evaluation Metrics

Mean Absolute Error (MAE), Mean Absolute Percentage Error (MAPE) and Root Mean Square Error (RMSE) are the metrics that are commonly used to check the accuracy of the predictions made. The smaller the values obtained from the calculations for these three metrics, the smaller the estimation error [27].

Mean Absolute Error (MAE): It is a measure of the errors between the estimate and the actual value of each data. The MAE method sums the absolute values of each data error and then calculates the mean error with the formula in Equation (8) [27, 28].

$$MAE = \frac{1}{k} \sum_{t=1}^k (y_t - \bar{f}_t)^2 \tag{8}$$

Mean Absolute Percentage Error (MAPE): It is a metric employed to assess the accuracy of a forecasting method, typically expressing forecast accuracy as a percentage. When the MAPE value is less than 10, it indicates the model's high accuracy. When the MAPE falls between 10 and 20, the model serves as a good estimator. A MAPE value between 20 and 50 suggests the model is a reasonable estimator. However, if the MAPE value is greater than 50, the model fails to produce correct results [27, 28]. The calculation of MAPE is demonstrated in Equation 9.

$$MAPE = \frac{1}{k} \sum_{t=1}^k \left| \frac{y_t - \bar{f}_t}{y_t} \right| * 100 \tag{9}$$

Root Mean Square Error (RMSE): It is a metric utilized to assess the mean difference between the predicted values and the true values of a statistical model [28]. RMSE is calculated with the help of the formula in Equation 10.

$$RMSE = \sqrt{\frac{1}{k} \sum_{t=1}^k (y_t - \bar{f}_t)^2} \tag{10}$$

5. Data Preparation

Historical order data from a poultry meat and meat products production facility were used for the estimations. This data includes order information from 2012 to 2021. The studies carried out to clean and organize the data are handled in the form of preparing customer-product-based data and arranging previous orders in case of an increase or decrease in customer demands.

5.1. Customer-Product Based Data Preparation

Customer order data includes different products from different product groups. Estimates made are based on customer product group. To carry out these transactions, existing orders are grouped according to order date, customer, and product categories. In addition, the order quantities for each product category were obtained. There are cancelled or repeated records in the data. For such records, elimination processes were carried out by looking at the order date-time, quantity, and product information. Elimination of cancelled or repetitive orders is also provided for each new order.

5.2. Arrangement of Past Orders According to Increase or Decrease in Customer Demands

A customer ordering a poultry meat and meat products production facility may increase or decrease in order quantities over time. In such cases, some adjustments are made to the previous order quantities for the estimations to be made. With these regulations, it is aimed to process the orders given in the past and today with the correct coefficient and to increase the accuracy of the estimations made. This process is achieved by obtaining a coefficient value by proportioning the orders made by the customer from the relevant product group and multiplying all orders with this coefficient value. Orders have been evaluated in 3-month seasonal periods for the arrangements to be made in order quantities. The maximum and minimum order quantities given by the customer from the relevant product group in each season were obtained, and these quantities were summed for each period and the weighted average was taken. By dividing the current season average with the previous season average, the ratio obtained with the order quantities entered in the previous season is ensured.

5.3. Arrangement of Days According to Past Order Information

Due to the fact that the daily capacity of the poultry meat and meat products production facility is certain and not all orders from all customers can be fulfilled with this capacity, the days that customers can place orders are limited. This restriction has been implemented for certain days of the week according to customer capacity. The days of the week that the customer will place an order on are determined annually and the customer is ensured to place an order only for the specified days. For example, a customer who is entitled to order on Mondays, Wednesdays and Fridays does not have the right to order on other days and the order quantity to be estimated due to this situation should be calculated as zero. In addition, giving the customer the right to order for a different day than the order days determined for the last year will cause problems in the estimation processes. For these cases, issues such as the number of days for which order right is granted in the current year is equal to previous years, the number of days for which order right is granted in the current year is less than previous years, and the number of days for which order right is granted in the current year is more than previous years.

6. Forecasting Customer Product Based Orders in Poultry Meat and Meat Products Production Facility

Forecasting processes, utilizing LSTM and Prophet models, were conducted on orders placed by a customer between the years 2013 and 2021. The training process for the estimation processes was carried out using three different processed data sets, and the results were evaluated on the root mean square error metric [5]. Forecasting processes are handled in three different ways: training and forecasting with the eliminated data of repeated and/or canceled orders, training, and forecasting by applying customer growth coefficient processes, arranging customer order day changes in historical data, and training and forecasting. Experimental studies on LSTM and Facebook Prophet models were carried out on Kaggle Notebooks. Examples from the dataset used in the training of the model are presented in Table 4.

Table 4. Dataset example

Order Date	Quantity	Month	Week	Weekday
12/20/2021	10	12	52	Monday
12/21/2021	0	12	52	Tuesday
12/22/2021	19	12	52	Wednesday
12/23/2021	0	12	52	Thursday
12/24/2021	23	12	52	Friday

6.1. Forecasting Made Using LSTM Algorithm

With the data preparation processes in the previous section, the customer's order data had repetitive orders cleared. The training phase utilized 80% of the data sets, while the remaining 20% was allocated for testing. For the training processes on the side of the LSTM model, estimations were made by looking back at the last 15 days before the relevant order date on each order day. The number of revolutions used in model training was determined as 35 through various experiments. The accuracy of the data obtained because of the training was provided with the root mean square error metric. The first data set to be trained with the LSTM model was provided over the data obtained by cleaning the repetitive orders. While performing this process, records that do not have an order entry in the data set are not included in the training and estimation. In the training and test processes, the root mean squared error values were obtained as 19.11 for the training data and 24.30 for the test data.

Another estimation process was carried out with the data obtained together with the cleaning of the repetitive orders in the data set, the periodic ratio and arrangement of the order data. While performing this process, records that do not have an order entry in the data set are not included in the training and estimation. In the training and test processes, the root mean squared error values were obtained as 9.02 for the training data and 8.39 for the test data. The final estimation process was carried out on the data obtained by cleaning the repetitive orders in the data set, arranging the order data periodically, and arranging the customer's order weekdays in the past years. While performing this process, the records that do not have an order entry in the data set are included in the training and estimation because they consist of fixed days. In the training and test processes, the root mean squared error values were obtained as 6.86 for the training data and 7.07 for the test data. The RMSE values obtained by using the LSTM algorithm on the data sets are shown in Table 5.

Table 5. RMSE values obtained by using LSTM algorithm on datasets

Data Sets	RMSE Values	
	Training	Test
1 st Data Set	19.11	24.30
2 nd Data Set	9.02	8.39
3 rd Data Set	6.86	7.07

6.2. Forecasting Using Prophet Time Series Algorithm

To determine the holidays, the Facebook Prophet algorithm was not used in data sets where repetitive order data were deleted, and the data were periodically proportioned and arranged. It is ensured that this algorithm is used only in the data set in which customer order days are adapted to previous years.

The first data set to be trained with the Prophet model was carried out with the data obtained by cleaning the repetitive orders. While performing this process, records that do not have an order entry in the data set are not included in the training and estimation. In the training and test processes, the root mean squared error values were obtained as 13.11 for the training data and 13.98 for the test data.

Another estimation process was carried out with the data obtained together with the cleaning of the repetitive orders in the data set and the periodic ratio and arrangement of the order data. While performing this process, records that do not have an order entry in the data set are not included in the training and estimation. In the training and test processes, the root mean squared error values were obtained as 11.07 for the training data and 12.39 for the test data.

The final estimation process was carried out based on the data obtained by cleaning the repetitive orders in the data set, arranging the order data periodically and arranging the weekdays of the customer's orders in the past years. While performing this process, the records that do not have an order entry in the data set are included in the training and estimation because they consist of fixed days. In the Prophet model, the days when the customer cannot place an order are determined as holidays. In the training and test processes, the root mean squared error values were obtained as 9.08 for the training data and 10.96 for the test data. The RMSE values obtained by using the Prophet algorithm on the data sets are shown in Table 6.

Table 6. RMSE values obtained by using Prophet algorithm on datasets

Data Sets	RMSE Values	
	Training	Test
1 st Data Set	13.11	13.98
2 nd Data Set	11.07	12.39
3 rd Data Set	9.08	10.96

7. Conclusions

In this study, the studies carried out to optimize the difficulties experienced in both meeting the raw material needs and meeting the order demands from the customers in the poultry meat and meat products production facilities are discussed. At this point, a study was carried out to meet customer order demands at the most optimum level by

making daily order estimations considering the past order data of a poultry meat and meat products production facility. When the literature is reviewed, it is seen that there are many different studies for customer order forecasting, but these studies are insufficient for poultry meat and meat products production facilities. Detailed research was conducted on meeting the incoming order demands of poultry meat and meat products production facilities. With the research, 9 years (between 2013-2021) order data of a poultry meat and meat products production facility were collected in order to predict customer order demands, and data sets were created by grouping these data on customer and product basis. In the created data sets, pre-processes were applied to clear the repetitive orders, to rate the previous orders periodically, and to adjust the previous orders on a week-by-day basis based on the customer's weekly order days of the previous year.

Three different data sets obtained were trained and tested with LSTM and Facebook Prophet models. Root mean squared error values were calculated for each data set. In the results obtained, it has been observed that the pre-processing applied to the data set has a successful effect on the estimation. In the case of applying all pre-processes in the LSTM model training, the root mean squared error value was 7.07, while in the Facebook Prophet model, this value was calculated as 10.96. In line with the data set used, it was observed that the LSTM model was more successful than the Facebook Prophet model. With the help of these estimates, the poultry meat and meat products production facility will be able to make stock and production planning for the future. In addition, it will be able to meet customer order demands at the optimum level with the least amount of product remaining in stock. The study was carried out with the customer order requests of the poultry meat and meat products production facility. In addition, the study revealed that order demands change in product price transitions. In the future, studies can be carried out to obtain more accurate results based on the product price transitions of the poultry meat and meat products production facility.




References

- [1] Ediz, Ç., Turan, A. H. (2020). Information Technology Applications in Multivariate Production Planning Decision. *International Journal of Economics and Administrative Studies*, Prof. Dr. Talha Ustasüleyman Special Issue, 19-30.
- [2] Zhang, Y., Jia, Z., Dai, Y. (2018). Real-Time Performance Analysis of Industrial Serial Production Systems with Flexible Manufacturing. *2018 Joint 10th International Conference on Soft Computing and Intelligent Systems (SCIS) and 19th International Symposium on Advanced Intelligent Systems (ISIS)*, Toyama, Japan, pp. 360-365.
- [3] Kozaklı, Ö., Mert, M., Fırat, M. Z. (2021). Türkiye etlik piliç üretiminin zaman serisi yöntemi ile modellenmesi. *Ege Üniversitesi Ziraat Fakültesi Dergisi*, 58(4), 557-567.
- [4] Holimchayachotikul, P., Murino, T., Payongyam, P., Sopadang, A., Savino, M., Elpidio, R. (2010). Application of Artificial Neural Network for Demand Forecasting in Supply Chain of Thai Frozen Chicken Products Export Industry. *12th The International Conference on Harbor, Maritime & Multimodal Logistics Modelling and Simulation*. Morocco.
- [5] Taylor, S. J., Letham, B. (2017). Prophet: Forecasting at Scale. *PeerJ Preprints*, 5:e3190v2.
- [6] Çabuk, M., Yücalar, F., Toçoğlu, M. A. (2023). Automated Analysis of E-Commerce Product Reviews with

- Machine Learning. *European Journal of Science and Technology*, 52: 110-121.
- [7] Lakshmanan, B., Vivek Raja, P.S.N., Kalathiappan, V. (2020). Sales Demand Forecasting Using LSTM Network. In: Dash, S., Lakshmi, C., Das, S., Panigrahi, B. (eds) *Artificial Intelligence and Evolutionary Computations in Engineering Systems. Advances in Intelligent Systems and Computing*, Springer, Singapore, vol. 1056, pp. 125–132.
- [8] Torres, J. F., Martínez-Álvarez, F., Troncoso, A. (2022). A Deep LSTM Network For The Spanish Electricity Consumption Forecasting. *Neural Computing and Applications*, 34: 10533–10545.
- [9] Chandriah, K. K., Naraganahalli, R. V. (2021). RNN / LSTM with modified Adam optimizer in deep learning approach for automobile spare parts demand forecasting. *Multimedia Tools and Applications*, 80(17): 26145-26159.
- [10] Çevik, Z. (2015). TMS 41 Çerçevesinde Kanatlı Kümes Hayvanlarının Değerleme ve Raporlanması, Doktora Tezi. Sakarya Üniversitesi, Sosyal Bilimler Enstitüsü, Muhasebe ve Finansman Anabilim Dalı, 210s, Sakarya.
- [11] Çelik, S., Özmelioglu, K., Karaali, A., Özdemir, V. (2014). Etlik Piliç Yetiştiriciliği. <https://www.tarimorman.gov.tr/HAYGEM/Belgeler/Hayvanc%C4%B1%C4%B1k/Kanatlı%C4%B1%20Yeti%C5%9Ftiricili%C4%9Fi/Etlik%20Pili%C3%A7%20Yetiştiriciligi.pdf> (Accessed: January 10, 2024).
- [12] Bailey, M. A., Hess, J. B., Krehling, J. T., Macklin, K. S. (2021). Broiler performance and litter ammonia levels as affected by sulfur added to the bird’s diet. *Journal of Applied Poultry Research*, 30(2).
- [13] Solano-Blanco, Alfaima L., González, Jaime E. & Medaglia, Andrés L., (2023). Production planning decisions in the broiler chicken supply chain with growth uncertainty. *Operations Research Perspectives*, Elsevier, vol. 10(C).
- [14] Bai, L., Cui, L., Zhang, Z., Xu, L., Wang, Y., Hancock, E. R. (2023). Entropic Dynamic Time Warping Kernels for Co-Evolving Financial Time Series Analysis. *IEEE Transactions on Neural Networks and Learning Systems*, 34(3): 1808 - 1822.
- [15] Zhang, L., Wang, R., Li, Z., Li, J., Ge, Y., Wa, S., Huang, S., Lv, C. (2023) Time-Series Neural Network: A High-Accuracy Time-Series Forecasting Method Based on Kernel Filter and Time Attention. *Information*, 14, 500.
- [16] Kotu, V., Deshpande, B. (2019). “Chapter 1 – Introduction”, *Data Science: Concepts and Practice*, Second Edition, Morgan Kaufmann, pp. 1-18.
- [17] Sinnaiah, T., Adam, S. and Mahadi, B. (2023). A strategic management process: the role of decision-making style and organizational performance. *Journal of Work-Applied Management*, 15(1): 37-50.
- [18] Lindemann, B., Müller, T., Vietz, H., Jazdi, N., Weyrich, M. (2021). A survey on long short-term memory networks for time series prediction. *Procedia CIRP*, 99: 650-655.
- [19] Yucalar, Fatih. (2023). Developing an Advanced Software Requirements Classification Model Using BERT: An Empirical Evaluation Study on Newly Generated Turkish Data. *Applied Sciences*, 13(20), 11127.
- [20] Zaini, N., Ean, L. W., Ahmed, A.N., Malek, M. A., Chow, M. F. (2022). PM2.5 forecasting for an urban area based on deep learning and decomposition method. *Scientific Reports*, 12(1), 17565.
- [21] Yong, Y., Xiaosheng, S., Changhua, Hu., Jianxun Z. (2019). A Review of Recurrent Neural Networks: LSTM Cells and Network Architectures. *Neural Computation*, 31(7):1235-1270.
- [22] Karasulu, B., Yücalar, F., Borandag, E. (2022). A hybrid approach based on deep learning for gender

- recognition using human ear images. *Journal of the Faculty of Engineering and Architecture of Gazi University*, 37(3): 1579-1594.
- [23] Dobilas, S. (2023). LSTM Recurrent Neural Networks — How to Teach a Network to Remember the Past. <https://towardsdatascience.com/lstm-recurrent-neural-networks-how-to-teach-a-network-to-remember-the-past-55e54c2ff22e> (Accessed: January 16, 2024).
- [24] Srivastava, P. (2023). Essentials of Deep Learning: Introduction to Long Short-Term Memory, *Analytics Vidhya*. <https://www.analyticsvidhya.com/blog/2017/12/fundamentals-of-deep-learning-introduction-to-lstm/> (Accessed: January 17, 2024).
- [25] Meng, J., Yang, X., Yang, C., Liu, Y. (2021). Comparative Analysis of Prophet and LSTM Model. *Journal of Physics: Conference Series*, 1910(1): 12-59.
- [26] Datapred. (2018). A better Facebook Prophet. <https://www.datapred.com/blog/a-better-facebook-prophet> (Accessed: January 18, 2024).
- [27] Hyndman, R. J. (2014). Measuring Forecast Accuracy. *In: Business Forecasting: Practical Problems and Solutions*. John Wiley & Sons, Hoboken, 177-183.
- [28] Aytaç, U. C., Kucukyilmaz, T., Tarakcıoğlu, G. S. (2022). Comparison of Time Series Models for Predicting Online Gaming Company Revenue, *Journal of Statistics and Applied Sciences*, 6: 25-36.
- [29] Wang, Q., Peng, R. Q., Wang, J. Q., Li, Z., Qu, H. B. (2020). NEWLSTM: An Optimized Long Short-Term Memory Language Model for Sequence Prediction, *IEEE Access*, 8: 65395-65401.

One-Part Geopolymer Binder Based on Boron Wastes: Effects of Calcination Temperature and NaOH Dosage on Strength and Microstructure

Cavit Çağatay KIZILTEPE^{1*} , İsa YÜKSEL¹, , Serdar AYDIN² 

¹Bursa Technical University, Civil Engineering Department, 16310, Bursa, Türkiye

²Dokuz Eylül University, Civil Engineering Department, 35160, İzmir, Türkiye

Abstract

Boron Enterprise Facilities are located in Kütahya-Emet, Eskişehir- Kırka and Balıkesir-Bigadiç regions in Türkiye. Waste materials containing a sum of boron (15-20%) occur during boron beneficiation with different mining procedures. Boron mine wastes are not evaluated completely in any sector. In the scope of this study, boron mine wastes from Kırka Boron Enterprise Facility were used as raw material in the production of one-part geopolymer binder by alkali fusion method. The effect of sodium hydroxide dosage (%4, %6, %8 and %10) and calcination temperature (600 °C, 650 °C and 700 °C for 4h) on compressive strength and microstructure was investigated. Test results showed that one-part geopolymer binder can be produced from boron wastes by using alkali fusion method. The highest compressive strength of 29,1 MPa was obtained by using 4% NH and calcination at 650 C for 4h. Furthermore, the formation of new crystalline phases in geopolymer binders at higher calcination temperature caused a decrease in compressive strength values. The main reaction product of the one-part geopolymer based on boron wastes is Mg and Na incorporated C-(Mg, Na)S-H structure.

Keywords: Boron mine waste, Calcination, One-part geopolymer binder

Cite this paper as: Kiziltepe Ç.C., Yuksel İ. and Aydın S. (2024). One-Part Geopolymer Binder Based on Boron Wastes: Effects of Calcination Temperature and NaOH Dosage on Strength and Microstructure, 8(1):53-62.

*Corresponding author: Cavit Çağatay Kiziltepe
E-mail: cavit.kiziltepe@btu.edu.tr

Received Date: 22/12/2023
Accepted Date: 31/01/2024
© Copyright 2024 by
Bursa Technical University. Available
online at <http://jise.btu.edu.tr/>



The works published in the journal of Innovative Science and Engineering (JISE) are licensed under a Creative Commons Attribution-NonCommercial 4.0 International License.

1. Introduction

Türkiye has 74% of world proven boron reserves [1]. The boron reserves in our country are located in Kütahya-Emet, Bigadiç-Balıkesir and Kırka-Eskişehir. The number of different boron minerals is around 230. The most important boron minerals in terms of commercial value and availability in Türkiye are tincal, colemanite and ulexite. While the tincal mineral is just in Kırka, the colemanite and ulexite minerals are in Emet, Bigadiç and Kestelek. Boron is a strategic mine that has been commonly used in a lot of different industrial areas such as nuclear, construction, ceramic and etc.

The boron mine wastes having % 15-20 B_2O_3 are created during the enriching process of boron mine via different mining methods to produce various boron compounds such as boric acid, hydrated borax, and sodium perborates [2-4]. These wastes cannot be used at any sector and have to be stored at waste dams by boron enterprises. Furthermore, the storage of these wastes as open to atmosphere results in several environmental problems such as water, air and soil pollutions because the boron minerals in these wastes dissolve by the rain water [5,6]. This situation may generate a risk in terms of people who live near the Boron Enterprise Facilities. In literature, there are several investigations as to the use of boron waste especially to produce concrete [7], Portland cement [8] or based mortar [9,10] and brick [4,6,11].

Portland cement is the most extensively used binder in the world to produce construction materials such as concrete, mortar, etc. However, the raw materials (limestone and clay) used in the production of Portland cement bring about the devastation of the natural habitat and the production of the Portland cement leads to emissions of hazardous gases such as CO_2 , SO_2 , NO_x , etc. considerably damage to natural habitat. The complex compounds in Portland cement such as C_2S , C_3S , C_3A and C_4AF occur at $1300\text{ }^\circ\text{C}$ - $1400\text{ }^\circ\text{C}$, so the energy consumption rises to high level during production of Portland cement. Therefore, the production of greener binders alternative to Portland cement has been one of the significant research studies in recent years. These studies have generally focused on the production of two-part geopolymer binders. Nevertheless, the alkali activators used in two-part systems are corrosive which, is risky for human health. Moreover, the feasibility of two-part geopolymer binders is difficult for concreting in-situ [12,13].

Researchers have focused on the production of one-part geopolymer binders (just add water) in recent years due to the above mentioned reasons. One-part geopolymer binder can be produced three different methods, mixing solid raw material and solid activator, grinding solid raw material and solid activator together and alkali fusion. Alkali fusion is a method which is used to synthesise one-part geopolymer binders. Raw materials together with alkalis are calcined at high-temperatures. A limited number of studies on the geopolymer binders produced by alkali fusion method have been published up to now.

Ye et al. [14] prepared various dry mixes of red mud and sodium hydroxide at certain ratios. The prepared dry mixes were calcined at $800\text{ }^\circ\text{C}$ for 1h. Red mud based geopolymer binders produced via alkali fusion method was replaced with silica fume at certain ratios to prepare geopolymer pastes. Ye et al. [14] reported that the compressive strength values of paste specimens improved significantly with the increasing silica fume and decreasing water/binder ratio. Abdel-Gawwad and Khalil [15] prepared a dry mix consisting of 60% cement kiln dust and 40% feldspar. The dry mix was calcined via alkali-fusion method to obtain one-part geopolymer binder. The effects of calcination temperatures ($1200\text{ }^\circ\text{C}$ and $1300\text{ }^\circ\text{C}$) and the calcination durations (2h and 3h) and the amount of

sodium hydroxide (10% and %20) were investigated on geopolymer pastes. A compressive strength value of 52 MPa was obtained at 28d. Peng et al. [16] produced the geopolymer clinker by calcining bentonite with both sodium carbonate and sodium hydroxide. The calcination temperatures were 700 °C, 850 °C and 1000 °C and the calcination duration was 3h. Peng et al. [16] reported that the compressive strength of geopolymer paste obtained with geopolymer clinker that was produced by calcining the mixture of bentonite + sodium hydroxide (25%) at 1000 °C was 45 MPa while bentonite + sodium carbonate (33%) at 850 °C was 55 MPa at 210d. Ke et al. [17] calcined the blend of red mud and sodium hydroxide at 800 °C for 1h. Sodium hydroxide ratios were adjusted as 5%,10% and 15% Na₂O of red mud. Ke et al. [17] reported that the geopolymer paste specimens prepared with red mud based geopolymer binder having 5% sodium hydroxide gained the strength after 14d. Notwithstanding, the geopolymer paste specimens which were prepared with red mud based geopolymer binder having 10% and %15 sodium hydroxide gained 10 MPa and 8 MPa compressive strength in 7 days, respectively.

In the scope of this study, the use of boron mine wastes procured from Kirka Boron Enterprise Facility as a raw material was investigated to produce one-part geopolymer binder via alkali fusion method. The effects of different calcination temperatures (600 °C, 650 °C and 700 °C) and Na₂O ratios (4%, 6%, 8% and 10%) were investigated on compressive strength and microstructure.

2. Materials and Methods

2.1. Materials

The XRF analysis of raw and calcined boron mine wastes were given in Table 1. The XRF result of calcined boron mine was obtained from powder specimen calcined at 600 °C for 1h without using alkali fusion method. Furthermore, pellet sodium hydroxide with 97%-purity (TEKKIM®) was used as an alkali activator during the calcination process. Standard silica sand (LIMAK®) was used to produce mortar mixtures.

Table 1.The chemical compositions of raw and calcined boron mine waste

Waste Type	Oxides, by weight (%)										
	SiO ₂	CaO	Al ₂ O ₃	B ₂ O ₃	MgO	K ₂ O	Fe ₂ O ₃	Na ₂ O	SO ₃	TiO ₂	LOI
Raw	19,20	16,12	1,47	6,40	18,60	0,68	0,31	4,81	0,24	-	32,17
Calcined	25,21	22,03	1,59	7,34	24,55	0,93	0,40	5,55	0,38	-	12,03

2.2. Methods

Boron mine wastes were dried in an oven at 100 °C for 24h before they were calcined via alkali fusion method. After the drying process, boron mine wastes were grinded in a ball mill at 400 rpm and for 2 minutes. Sodium hydroxide solutions having different Na₂O ratios (4%, 6%, 8% and 10%) were prepared one day before the calcination process. Then, grinded boron mine wastes and sodium hydroxide solutions with a water/binder ratio of 0.37 were mixed together. The obtained paste mixtures were firstly shaped as a ball-bearing form to avoid the negations, such as melting and bonding to vessel, during the calcination process. Then, the paste mixtures were calcined at different calcination temperatures (600 °C, 650°C and 700 °C) for 4h at a high-temperature oven. The calcination temperatures used in this study were determined according to the TG/DT analysis of raw boron waste given in Figure 1.

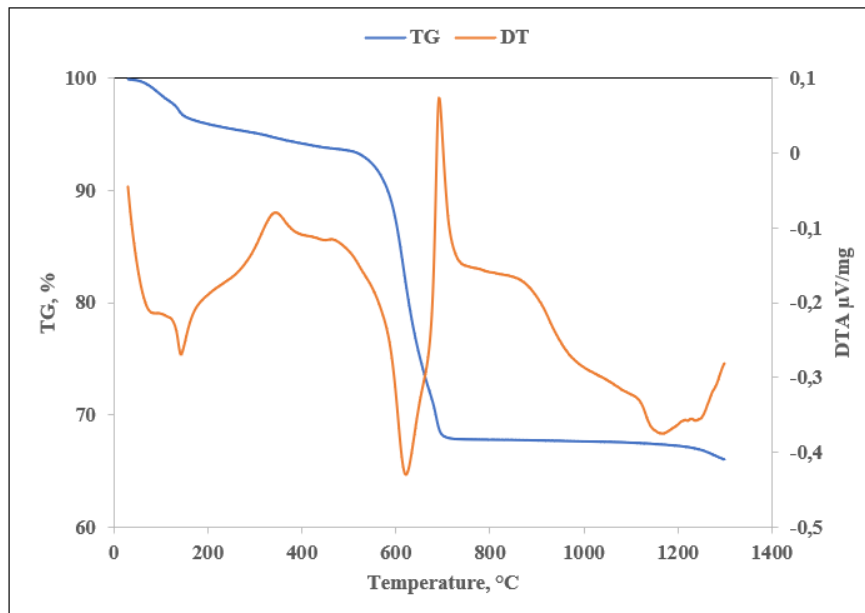


Figure 1. TG/DT analysis of boron waste

It is shown from Figure 1 that new exothermic peak has occurred at higher temperatures (at about 700 °C), which means that the cristalinity of calcined boron waste has increased and the reactivity of calcined boron wastes decreased. Calcined boron mine wastes were suddenly cooled to room temperature at the end of calcination process, and they were grinded again in a ball mill at 400 rpm and for 3 minutes. After the ball mill process, the d90 value of calcined boron mine wastes was about 30 μ .

Geopolymer mortar mixtures were produced by using laboratory type mixer. The aggregate/binder ratio of all geopolymer mortar mixtures were constant as 2.5. Initially, the geopolymer binders and standard sand were mixed in a dry state together to obtain homogen mixtures during 1 minute. Then, tap water was slowly added, and the mixing process continued during 3 min. Fresh geopolymer mortars were cast into steel molds (in size 50x50x50 mm) and compacted for 30 sec. The water/binder ratio of prepared geopolymer mortar mixtures was 0.52. After casting, the surface of geopolymer specimens open to atmosphere was covered with a nylon bag to avoid evaporation. The geopolymer specimens were left in laboratory conditions for 16h and then cured at 100 °C for 24h. After curing, the compressive strength values of geopolymer mortar specimens were determined in accordance with ASTM C109/C109M [18]. Finally, the SEM/EDS and XRD analyses were performed on the selected geopolymer paste specimens.

3. Results and Discussion

3.1. Compressive Strength Results of Geopolymer Mortars

Twelve geopolymer binders were produced at different calcination temperatures, Na₂O ratios and constant calcination duration via alkali fusion method along this study. It is importantly noticed that the mixtures codes were shortened as SH(A)-(B). SH is the abbreviation of sodium hydroxide. The A represents the Na₂O ratio while the B represents the calcination temperature. The water/binder ratio and calcination duration that were kept constant for all geopolymer binders were 0.52 and 4h, respectively.

The compressive strength results of geopolymer mortar specimens were presented in Figure 2. The increase in calcination temperatures from 600 °C to 650 °C, without taking into account Na₂O ratios, resulted in improving the

compressive strength values of geopolymer mortars between 32% and 67%. While the minimum compressive strength value was 16.3 MPa at 600 °C for geopolymer mortars having 10% Na₂O, the maximum increase rate (67%) between geopolymer mortars at 650 °C was obtained from mortars with 10%Na₂O. The compressive strength values of geopolymer mortars at 700 °C decreased as compared to 650 °C. The decrease in the strength was more pronounced for 4% and 6% Na₂O. This situation may be associated with the formation of new crystalline phase in geopolymer binders at higher calcination temperature.

As shown in Figure 2, the effect of Na₂O ratio on compressive strength values was found limited at 600 °C and 650 °C. The compressive strength values of the mortars prepared with geopolymer clinker calcined at 600 °C increased up to 8% Na₂O ratio while the compressive strength value of geopolymer specimens with 10% Na₂O decreased. A similar trend was observed at 700 °C. Furthermore, the compressive strength values of geopolymer mortar specimens having 4% Na₂O and 6% Na₂O ratios at 650 °C were obtained equal as 29.1 MPa. However, the compressive strength values decreased at higher Na₂O ratios. According to the obtained compressive strength results, the calcination temperature is a more effective parameter than the Na₂O ratio. Consequently, the optimum calcination temperature regardless of Na₂O ratios was determined as 650 °C.

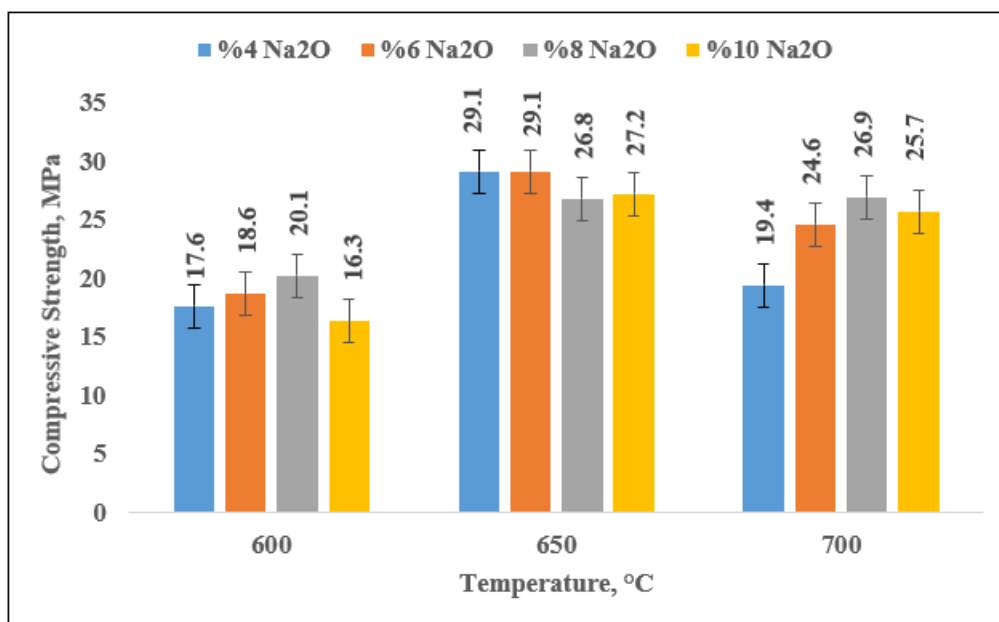


Figure 2. The compressive strength values of geopolymer mortars

3.2. Microstructure

In this section, four one-part geopolymer pastes (SH4-600, SH4-650, SH4-700 and SH10-700) were selected to determine the effect of different calcination temperatures and Na₂O ratios on the microstructures. Thus, XRD and SEM/EDX analyses were performed on the selected geopolymer pastes. Furthermore, XRD analysis of raw boron waste was performed to reveal the crystalline phases. XRD pattern of raw boron waste was illustrated in Figure 3. As shown in Figure 3, raw boron waste consisted of some crystalline phases such as dolomite, tinalconite and quartz. The most dominant phase in terms of intensity and count was dolomite.

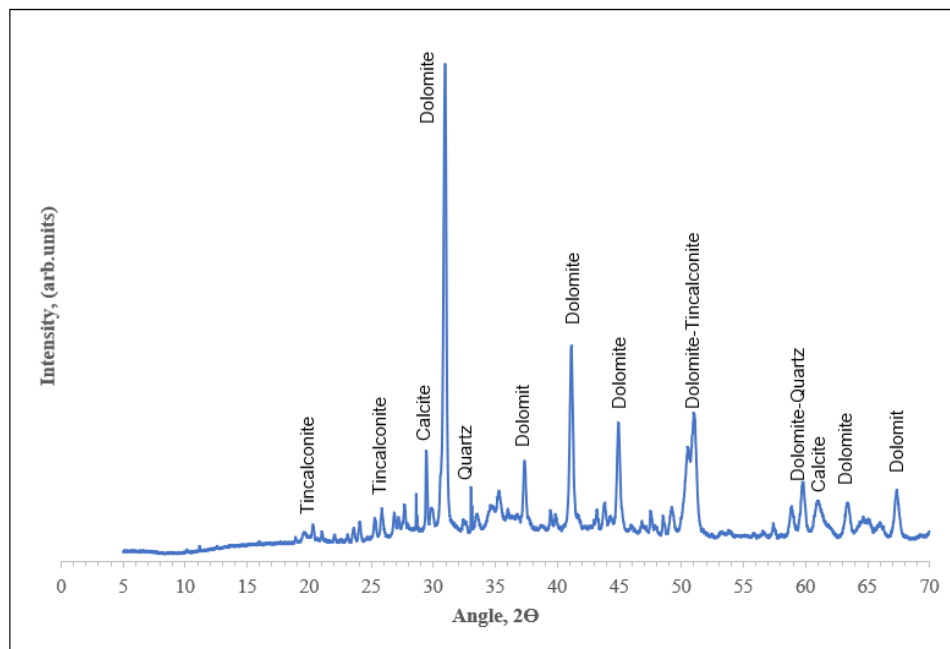


Figure 3. XRD analysis of raw boron waste

XRD patterns of selected geopolymer pastes were shown in Figure 4. After alkali fusion process, the crystalline phases in raw boron waste disappeared and was converted to the new crystalline phases. According to Figure 4, all geopolymer pastes consisted of brucite ($\text{Mg}(\text{OH})_2$, PDF Card Nr:01-073-8391), merwinite (PDF Card Nr: 04-011-6738), monticellite (PDF Card Nr: 00-035-0590), sodium oxide (PDF Card Nr: 00-001-1105), riversideite ($\text{Ca}_5\text{Si}_6\text{O}_{16}(\text{OH})_2$, PDF Card Nr:00-029-0329) and magnesium oxide (PDF Card Nr: 01-080-4184) crystal phases. However, the intensities of phases were different from each other. Merwinite ($\text{Ca}_3\text{Mg}(\text{SiO}_4)_2$) and monticellite (CaMgSiO_4) are a member of group of magnesium silicate. There is a peak for all geopolymer pastes about 29-30 °C (2θ) belonging to riversideite phase. Riversidiете is a member of the group of tobermorite gel (C-S-H), which has binding property that improves the compressive strength of geopolymer pastes. Thus, the improvement in compressive strength values for all geopolymer pastes can be explained with the formation of this phase.

If the intensities and counts of peaks has increased, the crystallinity degree of geopolymer paste has increased. This situation induces decrease in the compressive strength values of geopolymer paste. For example, the peak intensities of SH4-600 paste was found higher than that of SH4-650 paste such as SO, MO and MH. Therefore, the compressive strength value of SH4-650 (29.1 MPa) was obtained higher than the compressive strength value of SH4-600 (17.6 MPa). There was a similar situation between SH4-700 and SH10-700. The crystallinity degree of SH4-700 was higher than SH10-700 and so the compressive strength value of SH10-700 (25.7 MPa) was obtained higher than SH4-700 (19.4 MPa). Finally, it can be seen from the test results that the XRD results and the compressive strength results were compatible with each other.

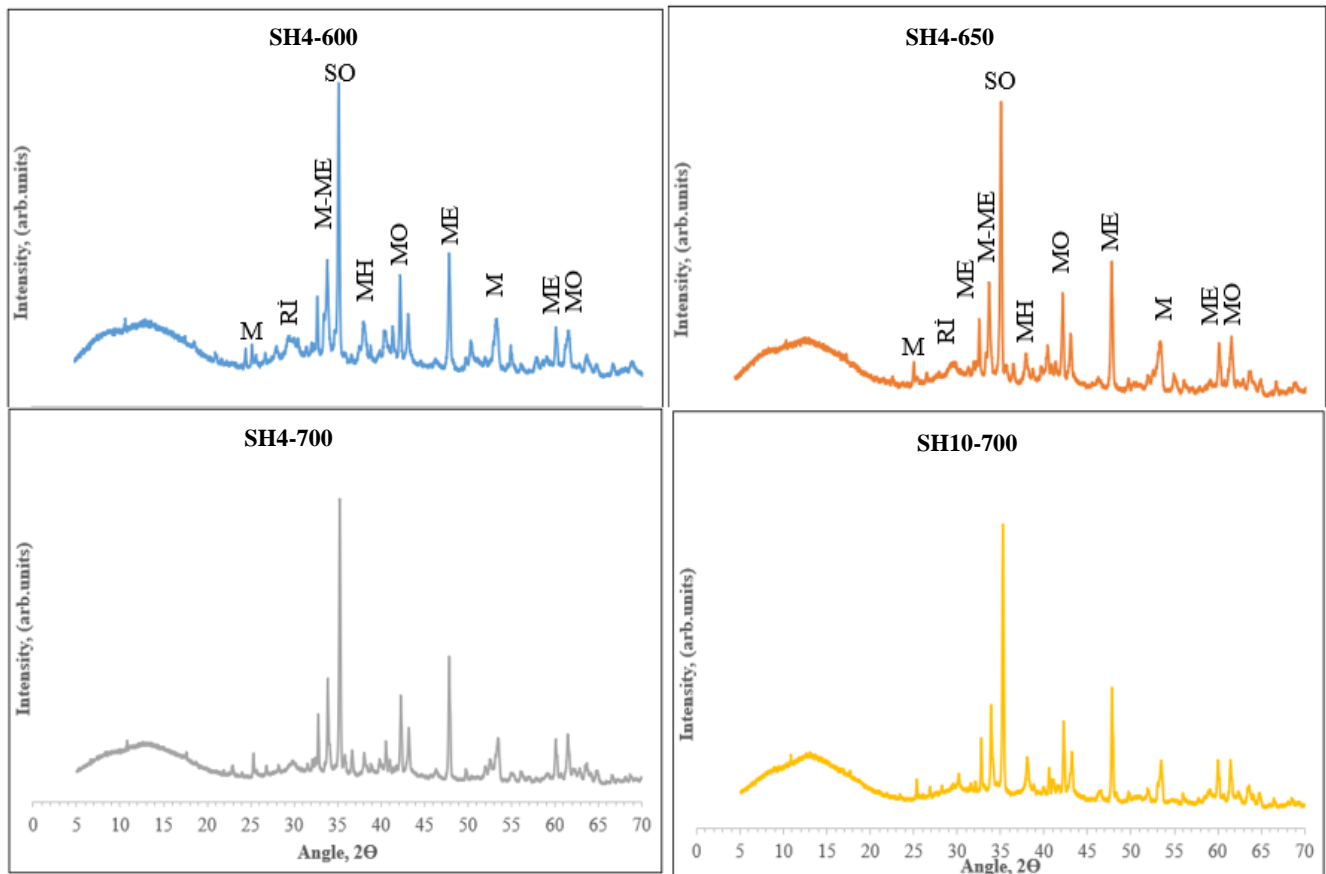


Figure 4. XRD patterns of geopolymer pastes (ME: Merwinite; M: Monticellite; SO: Sodium Oxide; MO: Magnesium Oxide; MH: magnesium hydroxide; RI: riversideite)

SEM images of geopolymer pastes were illustrated in Figure 5. The morphology of SH4-650 paste is denser than SH4-600 and SH4-700 pastes. The reaction products of SH4-650 has uniformly filled the voids with respect to SH4-600 and SH4-700. It explains the higher compressive strength value of SH4-650 as compared to SH4-600 and SH4-700 (Figure 2). The morphology of SH4-600 and SH4-700 was similar to each other like the compressive strength values. Furthermore, the matrix phase SH10-700 is denser with fewer voids than SH4-700 paste, which results in an increase in the compressive strength values. According to EDX analysis on SH4-600 paste having the lowest compressive strength, the reaction product marked with a circle on the SEM image in Figure 5, consists of Ca, Si, Mg and Na. The atomic ratios of Ca, Si, Mg and Na have been about 10%, 7%, 2% and %41, respectively. Ca/Si ratio was determined as 1.44 in this region. Therefore, it can be concluded that Mg and Na incorporated C-(Mg, Na)-S-H gel occurred as a binding phase in the light of EDX and XRD results. Furthermore, the excess of Na in this region derives from sodium oxide which was determined as crystalline phase as shown in Figure 4.

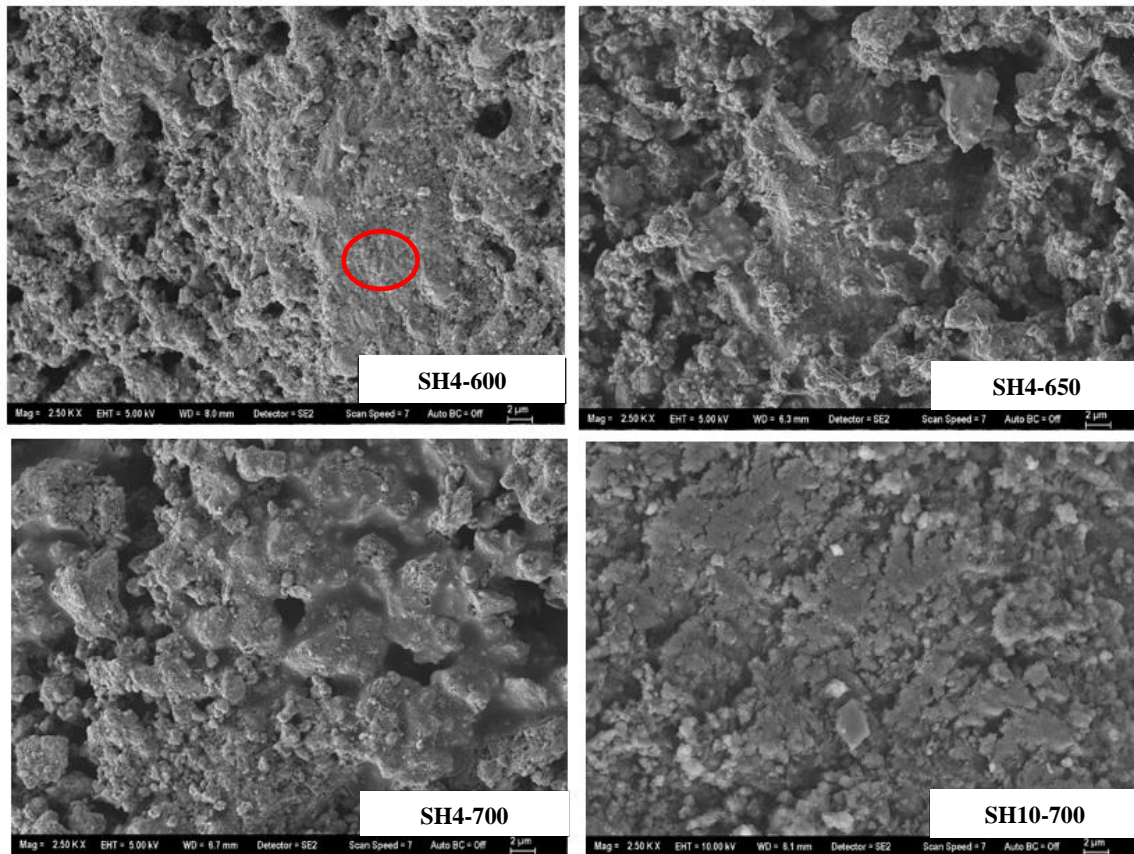


Figure 5. SEM images of geopolymer pastes

4. Conclusion

In the present study, boron mine waste discarded from Kirka Boron Enterprise Facility was used in the production of one-part geopolymer binder. The effects of calcination temperatures (600 °C, 650 °C and 700 °C) and Na₂O ratios (4%, 6%, 8% and 10%) of the geopolymer clinker on the compressive strength and microstructure of one-part geopolymer have been investigated. The obtained results in the scope of this study are as follows,

- The compressive strength values of geopolymer mortars increased by increasing the calcination temperature from 600 °C to 650 °C. On the other hand, with the increase in the calcination temperature from 650 °C to 700 °C, the compressive strength values of geopolymer mortars decreased. This situation is related to increase of the degree of crystallinity degree at higher calcination temperature. The more compressive strength values were obtained from geopolymer mortars which was calcined at 650 °C. The highest compressive strength value with 29,1 MPa was obtained from SH4-650 geopolymer mortar.
- The effect of Na₂O ratio of the geopolymer binders on compressive strength values was not as effective as calcination temperature.
- All geopolymer pastes have consisted of brucite merwinite, monticellite, sodium oxide, riversideite and magnesium oxide crystal phases. Mg-Na incorporated C-(Mg,Na)-S-H gel has occurred as a reaction product which is responsible for high compressive strength.
- Test results showed that one-part geopolymer binder can be produced from boron wastes by using alkali fusion method. One-part geopolymer binder can be obtained at low activator dosage as compared to two-part geopolymer binder.

Acknowledgement

The authors wish to express their gratitude and sincere appreciation to the Scientific and Technological Research Council of Türkiye (TUBİTAK) (Grant Nr. 219M426) for financing this research work. Additionally, the authors would like to thank Eti Mining Operations General Directorate for providing materials. Finally, the authors would also like to thank Ms.Ayşenur SİĞİNDERE for her great assistance in the lab.

References

- [1] Bor Sektör Raporu. 2011. Eti Maden İşletmeleri Genel Müdürlüğü. Türkiye: Bor Sektör Raporu.
- [2] Özdemir, M., Öztürk, N. U. (2003). Utilization of clay wastes containing boron as cement additives. *Cement and Concrete Research*, 33(10): 1659-61.
- [3] Kıpçak, İ., and M. Özdemir. (2012). Recovery of boron from the clay waste of boron industry by leaching. *Int. J. Chem. React. Eng.*, 10 (1): 1–13.
- [4] Uslu, T. Arol, A. I. (2004). Use of boron waste as an additive in red bricks. *Waste Management*, 24(2): 217-20.
- [5] Seiler, H. G., H. Sigel, and A. Sigel. (1988). Handbook on toxicity of inorganic compounds. *New York: Marcel Dekker*.
- [6] Kavas, T. (2006). Use of boron waste as a fluxing agent in production of red mud brick. *Building and Environment*, 41(12):1779-83.
- [7] Sevim, U. K. (2011). Colemanite ore waste concrete with low shrinkage and high split tensile strength. *Materials and Structures*, 44(1):187-193.
- [8] Koumpouri, D., Angelopoulos, G. N. (2016). Effect of boron waste and boric acid addition on the production of low energy belite cement. *Cement and Concrete Composites*, 68: 1-8.
- [9] Mutuk, T., Mesci, B. (2014). Analysis of mechanical properties of cement containing boron waste and rice husk ash using full factorial design. *Journal of Cleaner Production*, 69:128-132.
- [10] Över Kaman, D., Köroğlu, L., Ayas, E., Güney, Y. (2017). The effect of heat-treated boron derivative waste at 600 °C on the mechanical and microstructural properties of cement mortar. *Construction and Building Materials*, 154: 743-751.
- [11] Abalı, Y., Yurdusev, M. A., Zeybek, M. S., Kumanlioğlu, A. A. (2007). Using phosphogypsum and boron concentrator wastes in light brick production. *Construction and Building Materials*, 21(1): 52-6.
- [12] Liew, Y. M., Heah, C. Y., Li, L. Y., Jaya, N. A., Abdullah, M. M. A. B., Tan, S. J., Hussin, K. (2017). Formation of one-part-mixing geopolymers and geopolymer ceramics from geopolymer powder. *Construction and Building Materials*, 156: 9-18.
- [13] Zhang, H. Y., Liu, J. C., Wu, B. (2021). Mechanical properties and reaction mechanism of one-part geopolymer mortars. *Construction and Building Materials*, 273:121973.
- [14] Ye, N., Yang, J., Liang, S., Hu, Y., Hu, J., Xiao, B., Huang, Q. (2016). Synthesis and strength optimization of one-part geopolymer based on red mud. *Construction and Building Materials*, 111:317-25.
- [15] Abdel-Gawwad, H. A., Khalil, K. A. (2018). Application of thermal treatment on cement kiln dust and feldspar to create one-part geopolymer cement. *Construction and Building Materials*, 187: 231-7.

- [16] Peng, M. X., Wang, Z. H., Shen, S. H., Xiao, Q. G., Li, L. J., Tang, Y. C., Hu, L. L. (2017a). Alkali fusion of bentonite to synthesize one-part geopolymeric cements cured at elevated temperature by comparison with two-part ones. *Construction and Building Materials*, 130:103-112.
- [17] Ke, X., Bernal, S. A., Ye, N., Provis, J. L., Yang, J. (2015). One-Part Geopolymers Based on Thermally Treated Red Mud/NaOH Blends. *Journal of the American Ceramic Society*, 98(1): 5-11.
- [18] ASTM C109/C109M-20b. (2021). Standard Test Method for Compressive Strength of Hydraulic Cement Mortars (Using 2-in. or [50 mm] Cube Specimens). *Annual Book of ASTM Standards, USA*.

Evaluation of Cutting Temperature and Optimization in Milling of GGG60 Cast Iron

Rasit Duzce ¹ , Gurcan Samtas ^{2*} 

¹ Düzce University, Department of Manufacturing Engineering, Graduate School of Education, 81620, Düzce, Türkiye

² Düzce University, Department of Mechatronics Engineering, Faculty of Engineering, 81620, Düzce, Türkiye

Abstract

Spheroidal graphite cast irons have increased ductility, tensile strength, and toughness compared to other cast irons. Additionally, it can be mentioned that choosing spheroidal graphite cast iron over steel material has a better machining feature. In this study, face milling operations were carried out using GGG60 material and different inserts, feed, and depth of cut. The Taguchi method was used for the experimental design, and 27 experiments were performed. During the experiments, a thermal camera measured the temperature from the cutting zone. Experimental results were evaluated with analysis of variance and graphics, and cutting parameters were optimized. As a result of the optimization, optimum parameters for minimum temperature, TiAlN coated insert, 300 m/min cutting speed, 0.30 mm/tooth feed rate, and 0.5 mm depth of cut were found. According to the results obtained from the study, the most influential parameter affecting the temperature was the cutting speed. In addition, the TiAlN-coated insert has been observed as the most suitable coating type for minimum temperature.

Keywords: GGG60, Face milling, Taguchi, Optimization, Cutting temperature.

Cite this paper as:

Duzce, R. and Samtas, G. (2024).
Evaluation of Cutting Temperature and Optimization in Milling of GGG60 Cast Iron. Journal of Innovative Science and Engineering, 8(1): 63-77

*Corresponding author: Gurcan Samtas
E-mail: gurcansamtas@duzce.edu.tr

Received Date: 27/10/2022

Accepted Date: 18/04/2024

© Copyright 2024 by
Bursa Technical University. Available
online at <http://jise.btu.edu.tr/>



The works published in Journal of Innovative Science and Engineering (JISE) are licensed under a Creative Commons Attribution-NonCommercial 4.0 International License.

1. Introduction

Cast irons can be produced more efficiently in addition to their mechanical properties such as hardness, wear resistance, machinability, corrosion resistance, and strength. They have widely used engineering materials because they are economical [1]. Cast irons' machining depends on the casting's type and microstructure. While machining white cast iron is difficult, ferritic casting is more accessible than other cast irons. The machinability of spheroidal graphite cast iron, vermicular graphite cast iron, and alloyed and tempered cast irons are between white and ferritic castings [2]. Nodular graphite cast irons are used in many sectors, such as mining, machinery manufacturing, agricultural products, transportation, and construction. The mechanical properties of these materials are pretty good, and their corrosion resistance is high. Generally, cast irons are brittle. Spheroidal graphite cast irons, on the other hand, have an extremely tensile structure [3].

The surface quality of the material under processing is adversely affected by deformations in the cutting tools used in machining. The loss of tool life is the most significant of these drawbacks. One of the most important elements determining the cost of the cutting tools, or the production expenses, is the shortening of their lifespan. Therefore, it is important to know the parameters affecting tool life and to develop measures to control them [4]. Good mechanical properties are one of the most critical factors distinguishing it from other materials. In addition, the machining of the material is as necessary as the mechanical properties. Improving the machining of engineering materials is an industrially important parameter as it will reduce manufacturing costs.

As a result, several studies on machining can be found in the literature. When the literature is analyzed, certain studies claim that the alloying elements added to the material significantly impact the microstructure, mechanical characteristics, cutting force, and surface roughness of ductile cast iron and austempered ductile cast iron [5, 6]. Again, in some studies, it is stated that low austempering temperature decreases the surface roughness values while increasing the cutting forces in the machining of spheroidal graphite cast iron and austempered spheroidal graphite cast iron. It has also been stated that increasing the cutting speed reduces the vibration during the cutting process [7, 8]. In addition, various studies investigate the abrasive wear behaviour of austempered spheroidal graphite cast irons, the effect of cooling in the austempering process, and the effect of austempering temperature and time on machining [9-11]. Moncada et al. investigated the parameters affecting the machinability in turning austempered cast irons [12]. The wear types that occur in cutting tools in cast iron machining are abrasive, adhesive, and diffusion wear. The cutting tool properties sought in cast iron machining are high hardness and chemical stability. Besides sintered carbides, ceramic cutting tools are also used in cast iron machining [13]. Marwanga et al., in the turning process, investigated the changes in the microstructure of cast irons during machining [14]. Ahmet et al. Their study investigated the effect of machining conditions and material structure on the stress between the pencil and the part in the turning of four different lamellar graphite cast irons. Their study determined that the most significant factor in the stress difference increase was the amount of graphite in the total cross-section [15]. Kaçal et al. investigated the cutting tool wear and surface roughness during GGG70 ductile cast iron milling. According to the test results, it was observed that the surface roughness increased with the increase of the feed rate [16]. Kahraman et al., In their study, investigated the effect of austempering temperature and time on the surface roughness in the milling of vermicular graphite cast irons. In their research, they observed that the austempering heat treatment improved the surface quality of the materials [17]. Çakıroğlu and Uzun, in their study, performed the modeling

of the cutting force and workpiece surface roughness in the milling of vermicular graphite cast irons with artificial neural networks. As a result of the obtained mathematical model, it was seen that there was a harmony between the predicted values and the experimental results [18]. Askun et al., In their study, evaluated the machinability of spheroidal graphite cast irons alloyed with Ni and Cu in terms of cutting forces and surface qualities [19]. Avishan et al. investigated the effect of depth of cut on the machinability of alloyed austempered cast iron. As a result of their studies, they stated that reducing the depth of cut would not improve machinability [20]. Saraswati et al. investigated the mechanical properties and drillability behaviour of glass-sisal-epoxy hybrid composite material containing fillers such as fly ash and graphene. In addition, the mechanical and physical properties of the composite material used in their studies, such as tensile, bending, impact resistance, hardness, density and water absorption percentage, were also examined [21]. Pradhan et al. machined complex-shaped tapered holes using hot, abrasive jet machining. In their work, they conducted experimental studies to evaluate the abrasive footprint effect for hot, abrasive jet machining on surface roughness. They also modelled experimental studies using computational fluid dynamics [22]. Mahapatra et al. applied a hard turning process to AISI H13 steel using nanofluid with a minimum quantity of lubrication. The experiments measured tool vibration and surface roughness and analyzed chip morphology. In the experiments, AlTiNSiN nanocomposite-coated cutting tools were used [23]. Pradhan et al. performed the turning process on Functionally Graded material using nano-fluid-assisted minimum amount lubrication, and the machined surface and chip morphology were examined. In their study, they used three different spindle speeds, three different feeds and three different cutting depths. They chose the Taguchi L27 orthogonal array for the experimental design. Microstructure images of the machined surfaces were also examined with a scanning electron microscope [24]. Jena et al. applied hard turning to high-strength, low-alloy AISI 4340 steel. Their study modelled the surface roughness and optimized the cutting parameters. For the experimental design, the Taguchi L16 orthogonal array was selected. According to the ANOVA analysis performed in the study, it was stated that feed rate and cutting speed were effective parameters on surface roughness [25]. HAJM (Hot Abrasive Jet Machining) is a non-traditional process in which heated abrasive particles are sprayed at high speed and pressure. Pradhan et al. Their study applied the HAJM machining process, which uses SiC abrasive parts, to S_3N_4 material. In the study, regression models were created for all experimental results. The microstructures of the part surfaces after processing were analyzed using a scanning electron microscope. Additionally, CFD simulation was used, and RSM and genetic algorithms were also used [26].

When the literature was examined, no study was found to examine the cutting temperatures and evaluate the effects of cutting parameters in the face milling process of GGG60 material. In addition, the article has a unique value in using the Taguchi methodology in this study. In the study, L27 (3^4) Taguchi orthogonal array was chosen. Instead of 81 full factorial designs, 27 experiments were performed [27]. Experimental results were evaluated with Analysis of Variance (ANOVA) and 3D graphics. In addition, Taguchi's predictive values and experimental outcomes were compared.

2. Material and Methods

This article investigated the effects of cutting parameters on the cutting temperature in the face milling process of GGG60 cast iron, and the cutting parameters were optimized using the Taguchi method. The recommended dimensions for the test sample to be milled according to the ISO 8688-1 standard are at least three times the length and 0.6 times the cutting width of the tool holder diameter used [28]. Considering this situation, specially cast GGG60 spheroidal graphite cast iron was used in the milling experiments. The technical specifications of GGG60 cast iron are shown in Tables 1 and 2.

Table 1. GGG60 cast iron components (Matweb)

C	Fe	Mn	P	S	S
%3.2	%92.83	%0.1	%.0.15-	%	%0.005

Table 2. Mechanical and physical properties of GGG60 cast iron (Matweb)

Intensity	Hardness Brinell	Tensile Strength
7.30 g/cm ³	200-270	550 Mpa

In the experiments, TN6525 coded TiAlN coated, TN7535 coded TiN-TiCN-Al₂O₃ coated, and WS30PM coded AlTiN (multilayer) coated four cutting edge cutting edges belonging to WIDIA (Germany) cutting tool company were used. In addition, the three-edged tool holder suitable for the tips used is specially produced and supplied as an equivalent. (Figure 1).

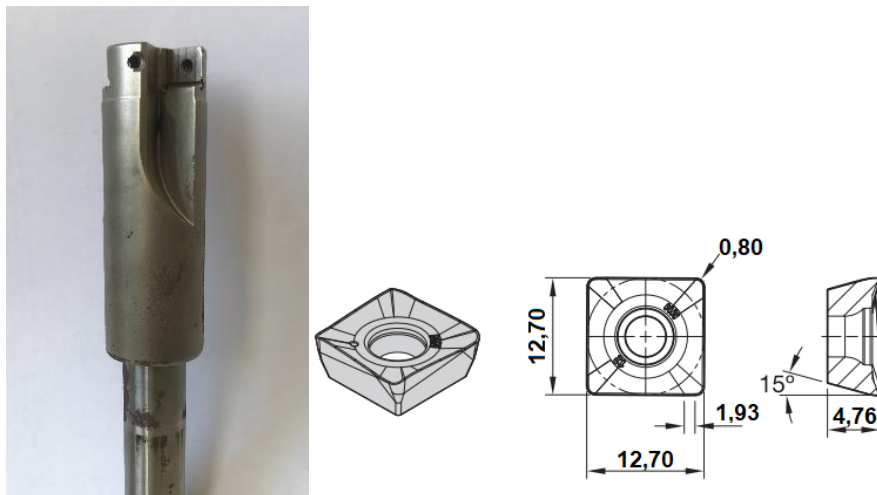


Figure 1. Tool holder and insert used

DELTA SEIKI 1050A triaxial vertical milling machine was used in milling operations. Experiments were performed in a dry environment without using a cooling liquid. Temperature measurements were made with a Fluke TiS20 thermal imager when the cutting tool reached the midpoint of the material. This takes about 3 seconds. The thermal camera used can measure between -20 °C and 350 °C, has a detector resolution of 120x90, a field of view of 35.7° x 26.8°, and a frame rate of 9 Hz.

3. Taguchi Method

3.1. Design and Conduct of Experiments

The Taguchi L27 orthogonal array was used for the experimental design. Only 27 experiments were performed instead of the full factorial design of 81 experiments. The number of experiments can be drastically reduced when using the Taguchi technique for analysis and assessment. To identify quality features, the Taguchi approach makes use of several functions. The Taguchi “smaller the better” function was used in this study because the smallest value was desired for the cutting zone temperature measurements. The selected cutting parameters and their levels are given in Table 3. The cutting tool catalogue was considered in determining the cutting parameters [29, 30]. The experimental design was created by considering the L27 orthogonal array. The experimental results and the S/N (signal-to-noise) ratios calculated according to the experimental results are given in Table 4.

Table 3. Parameters and levels

Parameters	Level 1	Level 2	Level 3
Cutting inserts (Kt)	TiAlN	TiN-TiCN-Al ₂ O ₃	AlTiN
Cutting speed (V, m/dak)	175	225	300
Feed rate (f, mm/tooth)	0.10	0.20	0.30
Cutting depth (a, mm)	0.5	1	1.5

Table 4. Experimental design and measured temperature values

Exp. no	Cutting parameters				Experimental results and S/N ratios	
	A	B	C	D	Temperature (T, °C)	S/N _T (dB)
	Cutting inserts (Kt)	Cutting speed (V)	Feed rate (f)	Cutting depth (a)		
1	TiAlN	175	0.1	0.5	47.7	-33.570
2	TiAlN	175	0.1	0.5	55.9	-34.948
3	TiAlN	175	0.1	0.5	54.9	-34.791
4	TiAlN	225	0.2	1	57.8	-35.239
5	TiAlN	225	0.2	1	54.3	-34.696
6	TiAlN	225	0.2	1	61.8	-35.820
7	TiAlN	300	0.3	1.5	52.7	-34.436
8	TiAlN	300	0.3	1.5	55.3	-34.855
9	TiAlN	300	0.3	1.5	48.4	-33.697
10	TiN-TiCN-Al ₂ O ₃	175	0.1	1.5	49.9	-33.962
11	TiN-TiCN-Al ₂ O ₃	175	0.1	1.5	57.6	-35.208
12	TiN-TiCN-Al ₂ O ₃	175	0.1	1.5	55.7	-34.917
13	TiN-TiCN-Al ₂ O ₃	225	0.2	0.5	58	-35.269
14	TiN-TiCN-Al ₂ O ₃	225	0.2	0.5	55	-34.807
15	TiN-TiCN-Al ₂ O ₃	225	0.2	0.5	57.1	-35.133
16	TiN-TiCN-Al ₂ O ₃	300	0.3	1	58.2	-35.298
17	TiN-TiCN-Al ₂ O ₃	300	0.3	1	58.8	-35.388
18	TiN-TiCN-Al ₂ O ₃	300	0.3	1	60.4	-35.621
19	AlTiN	175	0.1	1	53.4	-34.551
20	AlTiN	175	0.1	1	67.4	-36.573
21	AlTiN	175	0.1	1	66.8	-36.496

22	AlTiN	225	0.2	1.5	57.7	-35.224
23	AlTiN	225	0.2	1.5	52.7	-34.436
24	AlTiN	225	0.2	1.5	50.2	-34.014
25	AlTiN	300	0.3	0.5	47.7	-33.570
26	AlTiN	300	0.3	0.5	45.6	-33.179
27	AlTiN	300	0.3	0.5	51	-34.151

According to the test results, the average value of the temperature results was calculated as 55.259 °C, and the average S/N ratio for the temperature was -34.809 dB. The graph of the temperature values obtained from the experiments is given in Figure 2.

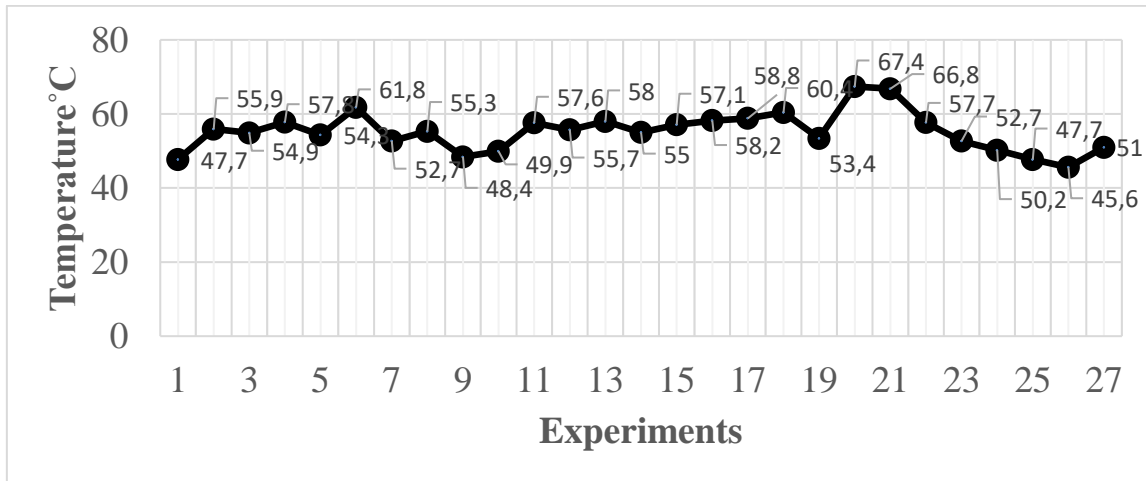


Figure 2. Temperature values obtained from experiments

The temperature images taken with the thermal camera are shown in Figure 3. The highest value in the cutting zone was considered in temperature measurements. In the study, it is seen that the highest temperature was in the 20th experiment. Here, the low feed rate also increases the machining time of the cutting tool on the material. Therefore, long friction is thought to cause an increase in temperature. On the other hand, AlTiN coatings have a higher coefficient of friction than different coating types. Therefore, the temperature increase in the 20th experiment can also be attributed to the coating type.

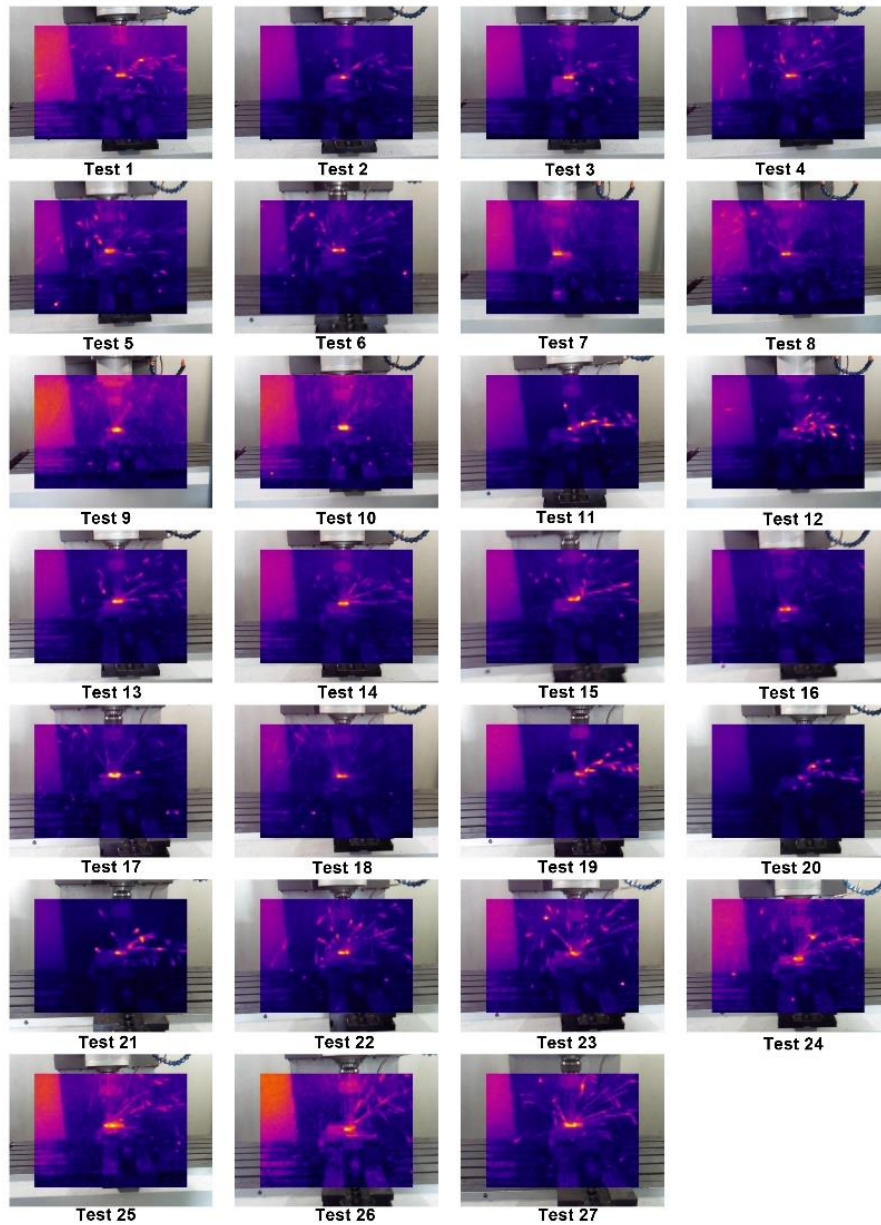


Figure 3. Thermal images obtained with a thermal camera

3.2. Determining Optimum Levels

Table 5 shows the averages of the S/N ratios for each level. These levels show the average values of the S/N ratios calculated for the analysis of temperature values in the experimental research. Predictive values for the ideal parameters are computed using these values.

Table 5. Means of S/N ratios for each level

Parameters	Levels			Delta
	Level 1	Level 2	Level 3	
A (Cutting insert, Kt)	-34.70	-35.08	-34.74	0.38
B (Cutting speed, V)	-35.06	-34.98	-34.48	0.58
C (Feed rate, f)	-35.06	-34.98	-34.48	0.58
D (Cutting depth, a)	-34.40	-35.56	-34.56	1.16

One of the critical steps in the Taguchi method is specifying the optimum levels. Optimum levels are determined by evaluating different levels of cutting parameters and combinations created by the chosen orthogonal array. These levels are used to draw the effect graph (Figure 4). At the same time, they were evaluating the main effect graph. The lowest level for the temperature values and the highest levels for the S/N ratios are considered since the desired minimum temperature.

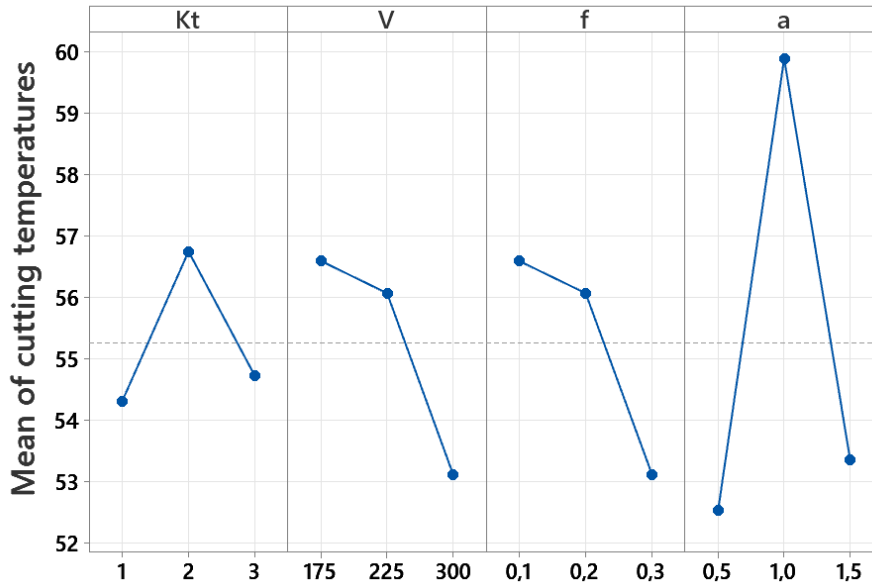


Figure 4. Main effect graph for temperature values

The optimum combination of test parameters for minimum temperature values according to Figure 2 is $A_1B_3C_3D_1$ (A_1 = TiAlN coated insert, B_3 = 300 m/min cutting speed, C_3 = 0.30 mm/tooth feed rate and D_1 = 0.5 mm cutting depth) determined.

3.3. Evaluation by ANOVA

The Taguchi confidence interval is calculated using an ANOVA (Analysis of Variance) to examine the interactions between all the parameters employed in the experimental design, how they affect the quality characteristics, how these changes in quality characteristics occur at various cutting parameter levels [31, 32]. The effects of the cutting insert, cutting speed, feed rate, and depth of cut on temperature were evaluated by ANOVA, and the results of the ANOVA are shown in Table 6.

Table 6. ANOVA results

Factors	Degrees of freedom (DF)	Sum of squares (SS)	Mean squares (MS)	F	T-Value	P-Value	Factor effect (%)
Kt	1	0.761	0.7606	0.02	0,16	0.877	0.10
V	1	58.456	8.8007	0.29	-0,53	0.599	7.84
f	1	4.425	4.4246	0.14	0,38	0.708	0.59
a	1	2.961	2.9606	0.10	0,31	0.760	0.40
Error(e)	22	678.543	30.8429				91.06
Total	26	745.145					100

According to the ANOVA result, the R^2 value was 8.94%. When the variance analysis results were evaluated, the most influential parameter affecting the temperature was the cutting speed, with 7.84%. This parameter is followed by the

rate of progression of 0.59%. The error rate in the table is 91.06%. The amount of an observed variable differs from the model's predicted value in ANOVA. So, the error is the portions of the scores not accounted for by the analysis. In ANOVA, the errors are assumed to be independent and generally distributed around the sample means [33]. In the Taguchi method, analysis of variance is used to calculate the confidence interval and determine the most influential parameter. Therefore, it is sufficient to state that cutting speed is the most significant factor here. It is also possible to see similar results in the literature [34].

3.4. Confirmation Tests and Taguchi Predicted Values

The validation experiments and the quality characteristics are examined in the final stage of the Taguchi method. To put it another way, validation experiments are run to verify the chosen ideal set of cutting parameters and levels. A₁B₃C₃D₁ (A₁= TiAlN coated insert, B₃ = 300 m/min cutting speed, C₃ = 0.30 mm/tooth feed rate, and D₁ = 0.5 mm depth of cut) estimation based on the optimum combination obtained for the temperature, taking into account the individual effects of the cutting parameters temperature value (T_p) is calculated with the following equations [35, 36].

$$\eta_{gT} = A_1 + B_3 + C_3 + D_1 - 3\eta_{\frac{S}{N}-T} \quad (1)$$

$$T_p = 10^{-\eta_{gT}/20} \quad (2)$$

They are the signal-to-noise ratios of the optimum levels of the A₁B₃C₃D₁ parameters (Table 5). $\eta_{\frac{S}{N}-T}$ is the average of the S/N ratios of the temperature values. S/N ratio calculated for η_{gT} temperature optimum levels and T_p are Taguchi prediction values calculated for temperature. The temperature estimate value calculated using Equation 1 and Equation 2 was 48.05 °C. A confidence interval (CI) is used to compare the result of validation experiments with the predicted value and confirm the “smaller the better” characteristic. The CI (Eq. 3) is the maximum and minimum value, and the accuracy of the validation experiments is tested by comparing the calculated value with the predicted values [35, 36].

$$CI = \sqrt{F_{\alpha:1, V_e} \times V_{ep} \times \left(\frac{1}{n_{eff}} + \frac{1}{r} \right)} \quad (3)$$

In equation 3, $F_{\alpha:1}$, and the significance level is the F ratio of α , α significance level, $1 - \alpha$ confidence interval, V_e is the degree of freedom of the temperature error according to the variance analysis results. When Table 6 is examined, the degree of freedom of the error is 22. In this case, the 1-22 value from the 95% confidence level F table was 4.30. V_{ep} is again the variance of error according to the ANOVA, r is the number of validation experiments, and n_{eff} is the number of effective measured results [37, 38].

$$n_{eff} = \frac{N}{1 + V_t} \quad (4)$$

In Equation 4, N denotes the total number of experiments (27), and V_t represents the total degrees of freedom (4) of the shearing parameters for which the mean is calculated using Table 6. In this case, the n_{eff} was calculated as 5.4. In this study, considering the optimum combination determined for the temperature, three confirmation experiments were

performed for each. They are considering Eq. 3 and Eq. 4; the CI is 8.29. In using the confidence interval, the Taguchi estimation value calculated for each parameter is added and subtracted with the confidence interval. The mean of the validation experiments should be between these two values. The average of three verification tests conducted for the cutting temperature is 49.17 °C. In this case, for temperature, $(48.05-8.29) < 49.17 < (48.05+8.29) = 39.76 < 49.17 < 56.34$ range was obtained, and confirmation experiments for temperature were performed within the confidence interval. In this case, it can be said that the optimization is successful. Table 7 compares the experimental results with the Taguchi predicted values. Eq.1 and Eq.2 were used to calculate the estimation values. The approximative values and experimental values were close to each other. For confidential statistical analysis, error values should be less than 20% [31].

Table 7. Comparison of optimized and random conditions with predicted values

Levels	Taguchi method		
	Experiment	Prediction	Error (%)
A ₁ B ₃ C ₃ D ₁ (Optimum)	49.17	48.05	2.28
A ₂ B ₁ C ₂ D ₃ (Random)	55.70	57.89	3.78
A ₂ B ₂ C ₃ D ₁ (Random)	57.10	53.16	6.90

In Table 7, the experimental values are compared with the predicted values. It is seen that the error values between the results of the confirmation test and the results obtained by the Taguchi method are less than 20%. In this case, the results obtained from the validation experiments show that the optimization has been carried out successfully.

4. Results and Discussion

The cutting parameters affecting the experimental results and the effects of these parameters on the temperature were evaluated with three-dimensional graphics (Figure 5). Figure 5a shows the impact of cutting speed and inserts on the temperature in the graph. Here, the temperature drop is seen in the TiAlN-coated insert. This situation is similar to Taguchi-optimized values. When evaluated together with the cutting speed, it is seen that the temperature decreases with the cutting speed of 175 m/min, the TiAlN coated insert, the 300 m/min cutting speed, and the AlTiN coated insert. Considering all parameter effects in Taguchi optimization, these drop conditions are expected. Figure 5a shows that the highest cutting temperature is at 175 m/min cutting speed and AlTiN coated insert. In addition, in this graph, it is seen that the temperature increases as the cutting speed increases, but the temperature decreases at 300 m/min cutting speed and AlTiN coated insert. Figure 5b shows the effects of insert and feed rate on temperature. Here again, it is seen that the lowest temperature is in the TiAlN-coated insert. In addition, when evaluated with the feed rate, it can be said that these situations are similar to Taguchi optimized values, where the lowest temperature is 0.10 mm/tooth and 0.30 mm/tooth in the TiAlN coated insert. Figure 5b shows a 0.20 mm/tooth feed rate and a sudden temperature rise in the TiAlN-coated insert. This is attributed to the cutter coating type. Figure 5b shows the highest temperature at the AlTiN-coated insert and 0.10 mm/tooth feed. In addition, 0.30 mm/tooth feed and a sudden temperature drop are observed in the AlTiN-coated insert. If low-temperature values are desired, combinations of 0.30 mm/tooth or 0.10 mm/tooth feed and TiAlN coated insert, 0.30 mm/tooth feed, and AlTiN coated insert can be used.

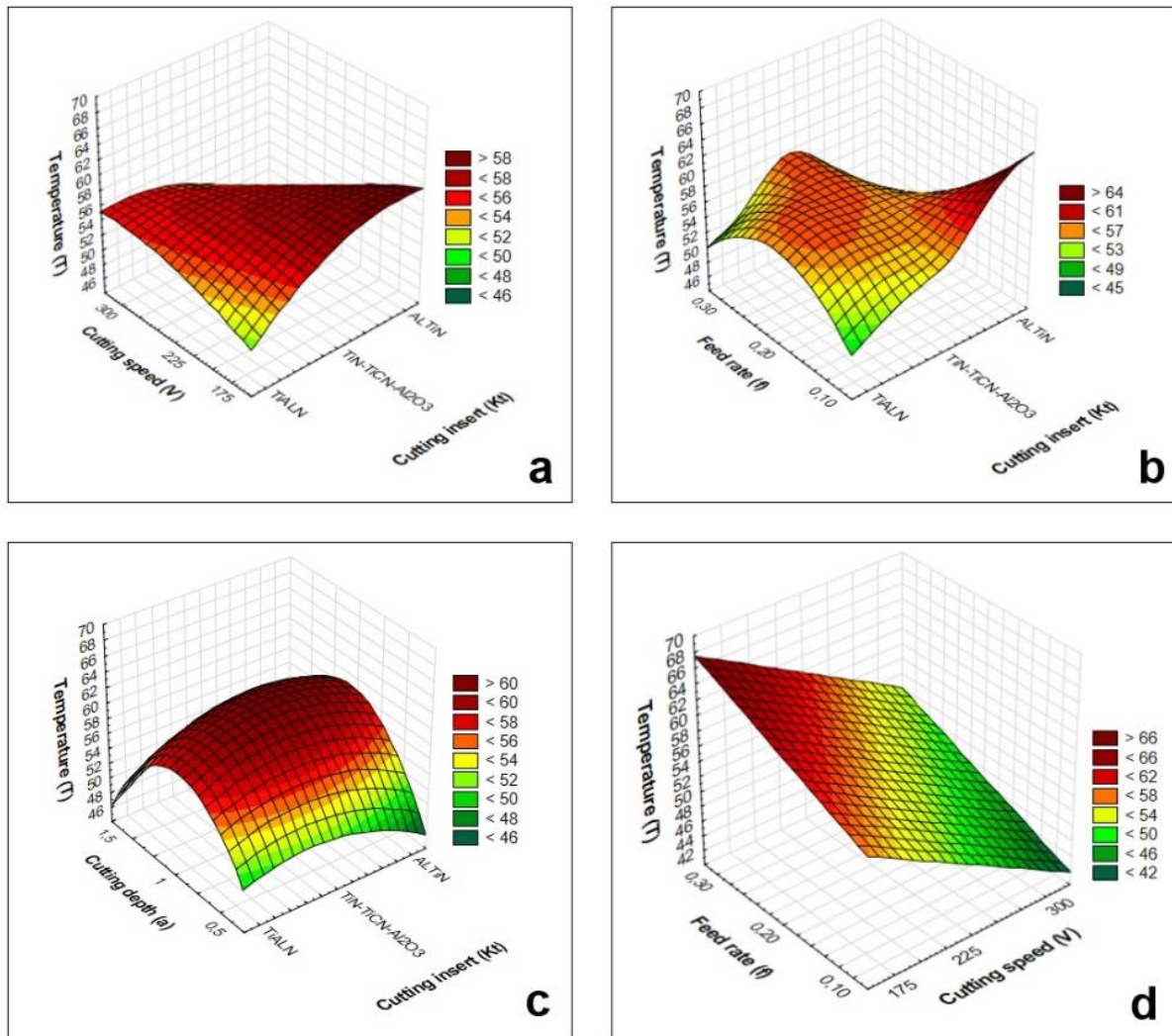


Figure 5. Effects of cutting parameters on temperature

Figure 5c shows the cut depth and the inserts' effects on temperature. Here again, the TiAlN-coated insert showed the best performance. It is seen that the lowest temperature is at 0.5 mm depth of cut and TiAlN insert. This situation is similar to Taguchi's optimized values. In addition, it is seen that the temperature increases as the depth of cut increases but decreases in the combination of 1.5 mm depth of cut and TiAlN insert. It also showed the best performance for all inserts with a depth of cut of 0.5 mm. The effects of cutting speed and feed rate on temperature are shown in Figure 5d. Here, it is seen that the temperature increases as the feed rate increases but decreases as the cutting speed increases. When the cutting speed and feed rate are evaluated together, it can be said that the best performance is 0.30 mm/tooth feed rate and 300 m/min cutting speed, similar to Taguchi's optimized values.

When the graphs were evaluated, it was seen that the TiAlN coating would exhibit ideal performance in terms of temperature in surface milling of GGG60 material. Increasing cutting temperatures during machining may cause chip adhesion to the cutting edge. This will increase the surface roughness. Therefore, low temperature is desired. According to these results, the article has a unique degree in the literature.

5. Conclusions

This study investigated the effects of cutting parameters on the cutting zone temperature in face milling processes applied to GGG60 cast iron. The Taguchi method was used for the experimental design, and 27 experiments were carried out. The cutting parameters were optimized in the study, and three validation experiments were carried out with the optimized parameters after the optimization. Taguchi prediction values and experimental results were compared. In addition, the effects of cutting parameters on temperature were evaluated with three-dimensional graphics. It is possible to list the results obtained from this study as follows;

- As a consequence of the optimization, the optimum combination of the test parameters for the minimum temperature values is $A_1B_3C_3D_1$ (A_1 = TiAlN coated insert, B_3 = 300 m/min cutting speed, C_3 = 0.30 mm/tooth feed rate, and D_1 = 0.5 mm cutting depth).
- The average of the three validation experiments conducted with optimized parameters (49.17 °C) was below the average of the test results (55.259 °C).
- When the variance analysis results were evaluated, the cutting speed was the most influential parameter affecting the temperature, with 7.84%. Since the cutting speed is, the distance travelled in meters per minute, increasing and decreasing the cutting speed directly affects the cutting speed as it will change the friction per unit time. Therefore, the ANOVA result confirms this explanation.
- The estimated value (48.05°C) calculated using the Taguchi method was below the average of the test results. This shows that the Taguchi method can be used successfully in similar studies.
- When the results obtained from the experiments with the optimum and randomly selected parameters were compared with the Taguchi estimation values, the error values were below 7%. For reliable statistics, the error value should be below 20%.
- When the three-dimensional graphics are evaluated, the optimal incision tip coating for the minimum temperature is the TiAlN-coated insert, similar to the Taguchi optimized parameters.
- TiAlN coating is recommended for the inserts used in this study if the low temperature is desired in face milling operations to be applied to GGG60 cast iron.
- Titanium Aluminum Nitride coating is suitable for machining very hard steels, aluminium-silicon and Titanium alloys. This coating thickness is generally 3-5 μm thick. Since it has a very hard structure, it allows work at high speeds. The study results show that this coating is the most ideal for performance.

This study used the Taguchi method to reduce the number of experiments and experimental design, thus saving time and processing costs. As a complete design, instead of 81 experiments, 27 experiments were carried out. When the experimental and Taguchi results are evaluated, the results obtained are applicable and satisfactory. In subsequent studies, tool wear and surface roughness values can be measured in face milling of GGG60 cast iron using the same orthogonal array, and experimental results can be optimized.



References

- [1] Çelik, Ö. (2001). Küresel Grafitli dökme demirlerin aşınma davranışları, Yüksek Lisans Tezi, İstanbul Üniversitesi, Fen Bilimleri Enstitüsü, İstanbul, Türkiye.
- [2] Murthy, V.S.R. and Kishore, Seshan, S., (1984). Characteristics of compacted Graphite Cast Iron, Transactions of the American Foundrymen's Society, 92: 373-380.
- [3] Makine Eğitimi, Küresel grafitli dökme demirler, Erişim Tarihi: Mart 17, 2022 [Online]. Erişim: <https://www.makinaegitimi.com/kuresel-grafitli-dokme-demirler/>.
- [4] Coelho, R.T., Souza, A.F., Roger, A.R., Rigatti A.M.Y. and Riberio, A.A (2010). Mechanistic approach to predict real machining time for milling free-form geometries applying high feed rate, International Journal of Advanced Manufacturing Technology, 46: 1103–1111.
- [5] Hsu, C.H., Chen, M.L. and Hu, C.J. (2007) Microstructure and mechanical properties of 4% cobalt and nickel alloyed ductile irons, Materials Science and Engineering A, 444: 339–346.
- [6] Şeker, U., Çiftçi İ. and Hasirci, H. (2003) The effect of alloying elements on surface roughness and cutting forces during machining of ductile iron, Materials and Design, 24: 47–51.
- [7] Uçun, I. and Aslantas, K. (2009). The performance of ceramic and cermet cutting tools for the machining of austempered ductile iron, International Journal of Advanced Manufacturing Technology, 41: 642–650.
- [8] Ghani, A.K. and Choudhury, Husni I.A. (2002). Study of tool life, surface roughness and vibration in machining nodular cast iron with seramic tool, Journal of Materials Processing Technology, 127: 17–22.
- [9] Klocke, F. Klöpper, C. Lung, D. and Essig, C. (2007). Fundamental wear mechanisms when machining austempered ductile iron (ADI), Annals of the CIRP., 56(1): 73-76.
- [10] Cakir, M.C., Bayram A., Isik, Y. and Salar, B. (2005). The effects of austempering temperature and time onto the machinability of austempered ductile iron, Materials Science and Engineering A, 407: 147–153.
- [11] Çetin, M. ve Gül, F. (2006). Östemperlenmiş küresel grafitli dökme demirin abrasiv aşınma davranışına östemperleme işleminde soğutmanın etkisi, Gazi Üniv. Müh. Mim. Fak. Der., 21(2): 359-366.
- [12] Moncada, O.J., Spicacci, R.H. and Sikora, J.A. (1998). Machinability of austempered ductile iron, AFS Trans, 106: 39–45.
- [13] Çakır, M.C. (2018). Modern Talaşlı İmalatın Esasları, Dora yayınları, 155-239. ISBN: 978-6052470053.
- [14] Marwanga, R.O., Voigt, R.C. and Cohen, P.H. (2000). Influence of graphite morphology and matrix structure on chip formation during machining of continuously cast ductile irons, AFS Transactions, 108: 651, 2000.
- [15] Yardımeden, A., Aksoy, M. ve İnan, A. (2004). Lamel grafitli dökme demirlerin işlenmesinde kale mile parça arasında meydana gelen gerilime, işleme şartları ve malzeme yapısının etkisi, 11. Uluslararası Makina Tasarım ve İmalat Kongresi, Antalya, Türkiye.
- [16] Kaçal, A. Çelik, B. ve Sertsöz, Ş. (2019). GGG70 sfero dökme demirin frezelenmesinde yüzey pürüzlülüğü ve takım aşınmasının incelenmesi, IMCOFE 2019, Antalya, Türkiye, 308-315.
- [17] Kahraman, Y., Uzun, G. ve Korkut, İ. (2015). Vermiküler grafitli dökme demirlerin frezelenmesinde östemperleme sıcaklığı ve süresinin yüzey pürüzlülüğüne etkisi, 6. Ulusal Talaşlı İmalat Sempozyumu (UTİS 2015), İstanbul, Türkiye, 178-188.

- [18] Çakıroğlu, R. ve Uzun, G. (2021). Yüksek ilerleme ile frezeleme işlemi esnasında oluşan kesme kuvvetinin ve iş parçası yüzey pürüzlülüğünün Yapay Sinir Ağları ile modellenmesi, Gazi Mühendislik Bilimleri Dergisi, 7(1): 58-66.
- [19] Aşkun, Y., Hasırcı, H. ve Şeker, U. (2003). Ni ve Cu ile alaşımlandırılmış küresel grafitli dökme demirlerin işlenebilirliğinin kesme kuvvetleri ve yüzey kaliteleri açısından değerlendirilmesi, Pamukkale Üniversitesi Mühendislik Fakültesi, Mühendislik Bilimleri Dergisi, 9(2): 191-199.
- [20] Avishan, B., Yazdani, S. and Jalali, Vahid D. (2009). The influence of depth of cut on the machinability of an alloyed austempered ductile iron, Materials Science and Engineering A, 523: 93-98.
- [21] Saraswati, P.K. Sahoo, S. Parida S.P. and Jena P.C. (2019). Fabrication, characterization and drilling operation of natural fiber reinforced hybrid composite with filler (Fly-Ash/Graphene), International Journal of Innovative Technology and Exploring Engineering, 8 (10): 1653-1659.
- [22] Pradhan, S., Das, S.R., Jena, P.C. and Dhupal, D. (2021). Machining performance evaluation under recently developed sustainable HAJM process of zirconia ceramic using hot SiC abrasives: An experimental and simulation approach, Proceedings of Institute Mechanical Engineering Part C: J Mechanical Engineering Science, 1–27.
- [23] Mahapatra, S., Das, A., Jena, P. C. and Das S.R. (2023). Turning of hardened AISI H13 steel with recently developed S3P-AlTiSiN coated carbide tool using MWCNT mixed nanofluid under minimum quantity lubrication, Proceedings of Institute Mechanical Engineering Part C: J Mechanical Engineering Science, 237(4): 843-864.
- [24] Pradhan, S., Das, S.R., Jena P.C. and Dhupal, D. (2021). Investigations on surface integrity in hard turning of functionally graded specimen under nano fluid assisted minimum quantity lubrication, Advances in Materials and Processing Technologies, 8: 1714-1729.
- [25] Jena, J., Panda, A., Behera, A. K., Jena, P. C., Das, S.R. and Dhupal, D. (2019). Modeling and optimization of surface roughness in hard turning of AISI 4340 steel with coated ceramic tool, Innovation in Materials Science and Engineering, 151-160.
- [26] Pradhan, S., Dhupal, D., Das, S.R. and Jena P.C. (2021). Experimental investigation and optimization on machined surface of Si₃N₄ ceramic using hot SiC abrasive in HAJM, Materials Today: Proceedings, 44: 1877-1887.
- [27] Canıyılmaz, E. ve Kutay, F. (2003). Taguchi metodunda varyans analizine alternatif bir yaklaşım, Gazi Üniv. Müh. Mim. Fak. Der., 18(3): 51-63.
- [28] Taylan, F. (2009). Sert malzemelerin frezelenmesinde takım aşınma davranışlarının belirlenmesi, Doktora Tezi, Süleyman Demirel Üniversitesi, Fen Bilimleri Enstitüsü, Isparta, Türkiye.
- [29] WIDIA Cutting tool company (2020). Advances catalog, WIDIA press, Germany.
- [30] WIDIA Cutting tool company (2017). Master Catalog, WIDIA press, Germany.
- [31] Kara F.(2018). Optimization of surface roughness in finish milling of AISI P20+S plastic-mold steel, Materiali in tehnologije/Materials and technology, 52(2): 195–200.
- [32] Samtaş, G. ve Korucu, S. (2019). Kriyojenik işlem görmüş EN AW 5754 (AlMg3) alüminyum alaşımının frezelenmesinde yüzey pürüzlülüğü için kesme parametrelerinin optimizasyonu, Politeknik Dergisi, 22(3): 665-673.
- [33] Doncaster, C. P. (2022). Terminology of analysis of variance, Accessed: March 18, 2022 [Online]. Available: <http://www.southampton.ac.uk/~cpd/term.html>.

- [34] Samtaş, G. and Korucu, S. (2021). Multiple optimization of cutting parameters in milling of cryogenically treated Aluminium 6061-T651 alloy with cryogenic and normal cutting inserts, *Surface Topography: Metrology and Properties*, 9(4): 1-10.
- [35] Kara, F. and Öztürk, B. (2019). Comparison and optimization of PVD and CVD method on surface roughness and flank wear in hard-machining of DIN 1.2738 mold steel, *Sensor Review*, 39(1): 24-33.
- [36] Kıvak T. (2014). Optimization of surface roughness and flank wear using the Taguchi method in milling of Hadfield steel with PVD and CVD coated inserts, *Measurement*, 50: 19-28.
- [37] Samtaş G. (2015). Optimization of cutting parameters during the face milling of AA5083-H111 with coated and uncoated inserts using Taguchi method, *Int. J. Machining and Machinability of Materials*, 17(3/4): 211-232.
- [38] Samtaş, G. ve Korucu, S. (2019). Temperlenmiş alüminyum 5754 alaşımının frezelenmesinde kesme parametrelerinin Taguchi Metodu kullanılarak optimizasyonu, *Düzce Üniversitesi Bilim ve Teknoloji Dergisi*, 7(1): 45-60.

The Impact of Quality Dimensions and Some Other Critical Factors on Consumers' Furniture Purchasing Decisions

Melike Nur Ince ¹ , Cagatay Tasdemir ^{2*} 

¹ Department of Industrial Engineering (Grad. School), Bursa Technical University, Bursa, Türkiye

² Department of Forest Industry Engineering, Bursa Technical University, Bursa, Türkiye

Abstract

This research examined the influence of quality dimensions and various other factors on consumer choices in the Turkish furniture market, aiming to bridge a literature gap by leveraging theoretical insights and empirical data. Utilizing a detailed survey, the study captured consumer perceptions of factors influencing furniture purchases, focusing on Garvin's eight quality dimensions: suitability, perceived quality, features, aesthetics, service, durability, reliability, and performance. The methodology included a 19-question survey targeting Bursa's population to gather data on demographic characteristics and purchasing influences, which was analyzed via Microsoft Excel. The findings underscored the paramount importance that consumers placed on durability and performance, suggesting a pragmatic approach to furniture buying where functionality trumped aesthetics. A notable preference for sustainable and eco-friendly furniture emerged, aligning with broader environmental trends. Demographically, most respondents were young, university-educated adults, indicating a market segment with distinct tastes and preferences, particularly toward modern-style furniture. These insights advocated for furniture industry stakeholders to adopt marketing strategies emphasizing product durability, performance, and environmental friendliness, aligning with consumer expectations for quality and sustainability. This alignment could be crucial for guiding product development and design to cater to contemporary consumer needs.

Keywords: Consumer preferences, Furniture industry, Purchasing, Decisions, Quality dimensions

Cite this paper as:

Ince, M.N. and Tasdemir C. (2024). *The Impact of Quality Dimensions and Some Other Critical Factors on Consumers' Furniture Purchasing Decisions*. Journal of Innovative Science and Engineering. 8(1): 78-91

*Corresponding author: Cagatay Tasdemir
E-mail: cagatay.tasdemir@btu.edu.tr

Received Date: 15/03/2024

Accepted Date: 06/05/2024

© Copyright 2024 by
Bursa Technical University. Available online
at <http://jise.btu.edu.tr/>



The works published in Journal of Innovative Science and Engineering (JISE) are licensed under a Creative Commons Attribution-NonCommercial 4.0 International License.

1. Introduction

As society progresses, the evolution of human needs has become increasingly complex and multifaceted, transcending beyond basic survival to encompass a richer tapestry of desires and aspirations. In the early stages of human development, needs were predominantly focused on physiological sustenance and safety – essentials for survival. However, as civilization advanced, these needs evolved, placing a greater emphasis on social belonging, esteem, and self-actualization. Today, in a world characterized by rapid technological advancements and a plethora of choices, human needs have further diversified, integrating aspects of digital connectivity, environmental sustainability, and personal well-being. This evolution reflects a shift from mere survival to a quest for a more meaningful, interconnected, and self-aware existence. In this dynamic landscape, individuals seek not only physical comfort and security but also opportunities for personal growth, social connectivity, and a more profound sense of purpose. The evolution of human needs, thus, mirrors the journey of humanity itself – from basic survival to a pursuit of holistic fulfillment in an ever-changing world.

The intricate interplay between human motivation and behavior finds a compelling narrative in Abraham Maslow's Hierarchy of Needs, a theory that delineates the gradation of human necessities from the basic to the self-actualizing [1]. When applied to furniture needs, this hierarchy transcends beyond mere functionality, intertwining with the quality dimensions of furniture to reflect a broader spectrum of human desires and aspirations. Furniture, in its essence, is not just a fulfillment of the fundamental physiological need for rest and comfort but a representation of one's journey through Maslow's pyramid. Each quality dimension of furniture – from durability and comfort, aligning with the basic needs of safety and security, to aesthetic design and craftsmanship, resonating with the higher-order needs of esteem and self-actualization – mirrors the multifaceted nature of human needs.

Furniture has been presented in different styles for various uses from the past to the present. In the past, furniture, as a luxury and status symbol, involved intensive handcraftsmanship. The development of design, material, and production technologies has made it possible to offer a wide variety of options to consumers from all segments [2]. Although furniture in the past was a luxury and status symbol based on its handcraftsmanship, design, and production technology, it can still be used as a symbol of luxury and status even if not functionally necessary [3]. Therefore, furniture consumers' purchase decisions change based on essential demographic characteristics such as age, gender, and education [4]. Consumers' purchasing behaviors generally aim to achieve the highest yield at the lowest cost, regardless of the product and service [5]. Therefore, consumers generally prioritize brands widely accepted and preferred by everyone. However, each consumer's socio-cultural, psychological, demographic, and situational factors differ. This reflects on the purchasing process and shapes their preferences.

Studies in the literature on consumers' furniture choices revealed that age and income have been statistically significant factors, with age having a more potent effect in determining consumer preferences for different types of wood in furniture. Older participants preferred oak, while younger ones opted for spruce. Participants with higher income levels preferred cherrywood, whereas oak was chosen by those with lower income levels [6].

In their study conducted in Slovakia, Kaputa and Supin (2010) surveyed through email to determine the factors influencing furniture consumers' purchasing decisions. They found that the most important factors affecting consumers'

purchase decisions were quality, price, and design and noted that participants preferred more modern-style furniture [4]. Palus et al. (2012) examined consumer preferences in Slovakia and Poland for wood products, including joinery products and household furniture. They observed that consumers preferred wood-based materials for their ecological properties, environmental friendliness, renewability, naturalness, and health and safety features [7].

In another study, Olsiakova et al. (2016) used a survey and a structured Kano model to examine consumer requirements for wood products in 2004 and 2014. Their research suggested that Price was no longer the most critical factor for consumers, highlighting that quality had become more prominent [8]. Oblak et al. (2017) conducted a study using the Analytic Hierarchy Process (AHP) to analyze the purchasing behaviors of furniture consumers in Slovenia and Croatia. This research aimed to assist manufacturers and retailers in developing their marketing strategies. The study revealed that a lower price significantly incentivized furniture purchasing. It also observed that, in addition to obtaining information from furniture stores, potential consumers predominantly preferred the Internet as their primary source of information [9].

Atılgan et al. (2018) surveyed 392 individuals in Afyonkarahisar to examine consumer preferences towards furniture styles. The results showed that 76.3% of consumers preferred modern-style furniture. It was also observed that affordability, durability, comfort, ease of transportation, and aesthetics influenced furniture preferences [10]. Kaputa et al. (2018) studied customers' preferences regarding furniture materials, characteristics, and styles during purchases in Slovakia and Croatia. The findings indicated that wooden furniture was preferred over other alternatives [3].

Oblak et al. (2020) carried out a combined analysis study to understand consumer behaviors in furniture purchasing in Slovenia, Serbia, and Croatia. Their findings identified the three most important factors influencing purchasing decisions: quality, price, and additional services [11]. In another previous study, Jost et al. (2020) observed and analyzed changes in customer preferences regarding furniture materials, qualities, and styles in Slovenia between 2010 and 2019. The study revealed that tastes for furniture materials had changed over the last decade, with wooden furniture being widely preferred. It was observed that there were significant differences in the choice of materials for outdoor furniture during the observed period. The study also found a decrease in futuristic furniture preferences in 2019, while preferences for rustic and retro styles remained constant over time [12].

In their study, Loucanova and Olsiakova (2020) employed the Kano model to determine how Slovak consumers perceive retro innovations in wood products and identify the key features necessary for customer satisfaction. The results indicated that consumers positively perceived retro innovations in wood products, especially furniture, carpentry products, and other wooden designs. The study also revealed that consumers prefer wood since it's eco-friendly, renewable, natural, and safe. Furthermore, the study documented that price is no longer perceived as an essential parameter by consumers; instead, quality has become a more significant parameter [13].

Guzel (2020) surveyed citizens of Kayseri, Turkey, a significant player in the furniture and wood products manufacturing sector, to measure consumers' thoughts, knowledge, and awareness about wooden materials. The study analyzed the collected data using descriptive statistics and one-way ANOVA, which revealed that consumers find wood to be a natural and organic material that provides pleasure and happiness when used. However, due to the cost of solid wood, consumers are inclined to use wooden composite furniture. Additionally, it was found that consumers prefer wood for its certain qualities, such as eco-friendliness, renewability, naturalness, safeness, fire resistance, and sturdiness [14].

Barcic et al. (2021) directed their attention towards the identification and comparison of the purchasing habits of furniture consumers prior to and amidst the COVID-19 pandemic. Two surveys were carried out in Croatia, one during April and May in 2020, and the second one in March 2021. Disparities were discovered in consumer purchasing behaviors and preferences for wooden furniture among respondents based on demographic and economic factors both before and during the pandemic.[15].

When all these previous studies were reviewed, it was evident that the factors influencing consumers' purchasing behaviors vary according to regions, economic conditions, and demographic characteristics. Women prioritize design, quality, and functionality, while men focus more on Price. Younger consumers are inclined to conduct detailed research on products, whereas older individuals seek expert or peer opinions. Additionally, with the advancements in internet technology, consumers' channels for gathering information about furniture have shifted towards digital platforms. Moreover, consumers highlight wood and wood-based composite furniture as their preferred raw materials for furniture. This preference could be attributed to the importance consumers place on parameters such as ecological sustainability, renewability, naturalness, healthiness, safety, fire resistance, and durability [3, 7, 8, 13, 14]. These findings suggest that catering to "green" consumers could create a potential niche market for eco-labeled furniture products.

As can be interpreted from the above layout of previous literature, in the dynamic world of consumer behavior, the furniture industry stands as a testament to the complex interplay of quality, aesthetics, and consumer preferences. Purchasing furniture goes beyond the mere acquisition of a household item; it embodies the consumer's taste, lifestyle, and perceptions of quality. This article delves into the intricate relationship between the quality dimensions defined by marketing discipline and consumers' purchasing decisions. Despite the substantial research on consumer behavior in various sectors, the furniture market presents unique challenges and opportunities that merit a dedicated investigation.

Quality dimensions in furniture encompass a range of factors, from material and design to durability and brand reputation. Each element plays a critical role in shaping consumer preferences and decisions. However, existing literature has often treated these dimensions in isolation without fully exploring their collective impact on the consumer's decision-making process. Moreover, the studies exploring the characteristics of the customer base in Türkiye, and the rationale underlying their furniture purchasing decisions were either limited or absent. This gap in research presents an opportunity to examine how these quality dimensions intertwine to influence consumer choices in the furniture market.

Furthermore, the evolving consumer trends, driven by factors such as environmental consciousness and the pursuit of personalized experiences, have added new layers of complexity to this relationship. This study aims to bridge the gap in existing research by comprehensively analyzing how various quality dimensions and other critical factors collectively influence consumers' furniture purchasing decisions. By integrating theoretical insights with empirical findings, this article offers a nuanced understanding of consumer behavior in the furniture industry, providing valuable insights for manufacturers, retailers, and marketers alike. Such insights could provide significant opportunities for gaining a competitive advantage in the furniture industry. Therefore, the objectives of this study could be summarized as the identification of consumers' preferences related to furniture and the impact of the quality dimensions and other critical factors that influence their purchasing behaviors. Documenting the characteristics of customer preferences and attributes of the market could provide a deeper understanding of the dynamics shaping furniture purchasing decisions, offering

valuable knowledge for designers, furniture manufacturers, and marketers in product development, production, and marketing processes to ensure supply characteristics align with evolving needs and expectations of the market.

2. Material and Methods

The study was designed to snapshot the perceived importance of factors in consumers' furniture purchasing decisions. The research conducted by Kaputa and Supin (2010) on consumer preferences in furniture purchasing decisions in Slovakia has been adapted and altered to survey the Turkish consumer base [4]. The study was conducted after obtaining official approval from the Physical, Engineering, and Social Sciences Ethical Committee at Bursa Technical University.

Within the scope of this study, a 19-question survey was prepared using Google Forms. The survey form comprised two main sections: Demographic characteristics of consumers (3 questions) and factors influencing their purchasing decisions (16 questions). The demographic factors aimed to be identified were gender, age, and education level since consumers' furniture purchasing behaviors are influenced by demographic factors such as economic status, educational level, age, and gender [16, 17]. The questions regarding the factors influencing consumers' furniture purchasing decisions were constructed around Garvin's eight dimensions of quality, outlined in his work titled *Competing on The Eight Dimensions of Quality* [18]. These quality dimensions were suitability, perceived quality, features, aesthetics (design), pre- and post-sale service, durability, reliability, and performance. The impact of quality dimensions on the purchasing decision was also evaluated with the help of some indirect questions that explored the status of consumers' price sensitivity, shopping frequency, often-shopped-for furniture category, style preferences, and quality considerations while shopping for new furniture items. The survey utilized a 5-point Likert scale (Definitely Yes, Yes, Undecided, No, Definitely No) for the questions that did not require specific qualitative or quantitative answers.

Survey results were collected through digital link sharing, and the data was transferred to Microsoft Excel for visualization. For surveying purposes, Bursa, one of Turkey's largest furniture centers, was chosen as the study field. The population of Bursa, a total of 2.16 million people, formed the study population, and the study sample comprised city residents. From the population, at the 95% confidence level, 50% population variability, and $\pm 5\%$ margin of error, a sample size of 384 was determined by consequently using Equation 1 and 2 [19, 20].

$$n = \frac{z^2(pq)}{e^2} \quad (1)$$

Where;

n: Sample size

z: Standard error at the preferred confidence level

p: population variability

q: 100-*p*

e: Acceptable margin of error for the sample

$$n_{adjusted} = \frac{n}{1 + \frac{n-1}{N}} \quad (2)$$

Where;

$n_{adjusted}$ = Sample size adjusted for finite population

n = Calculated sample size with Equation 1

N = Population size

The data collection phase of the study was limited to three weeks, and the data obtained through Google Forms was compiled at the end of the three-week data collection period. Invitations were sent out in sets of 10 (five male and five female invitees) until the target sample size was reached within the data collection phase of the study. The study employed a Hybrid approach that combined Quota Sampling and Judgmental Sampling techniques. In quota sampling, the researcher determines quota characteristics based on factors such as demographics or product usage, and these are used to form quotas for each participant class [19]. A gender quota was applied in the study, with measures taken to ensure a balance close to a 50-50 distribution between male and female participants. The size of the quotas was determined based on the researchers' opinions about the proportional size of each participant class in the population.

In judgmental sampling, researchers used their judgment and the judgments of two furniture marketing experts to determine who would be included in the sample. This subjective and data-access-oriented method meant that certain population members had less chance of being selected than others. With the hybrid sampling approach, researchers invited population members whom they believed would provide the quickest access to data. The survey link was sent via email, online messaging applications, and social media to invite participation in the study.

3. Results and Discussion

In the study, nineteen questions were directed to the participants to observe the perceived importance of certain factors that could influence consumers' furniture purchasing decisions and the impact of various quality dimensions. The responses provided by the participants in the survey were summarized in graphical form. At the end of the data collection phase, the total number of invitations sent out amounted to 1600 (800 male and 800 female invitees), of which 384 people participated in the survey, and the responses of 2 people were invalidated due to inconsistencies, resulting in a 24% participation rate.

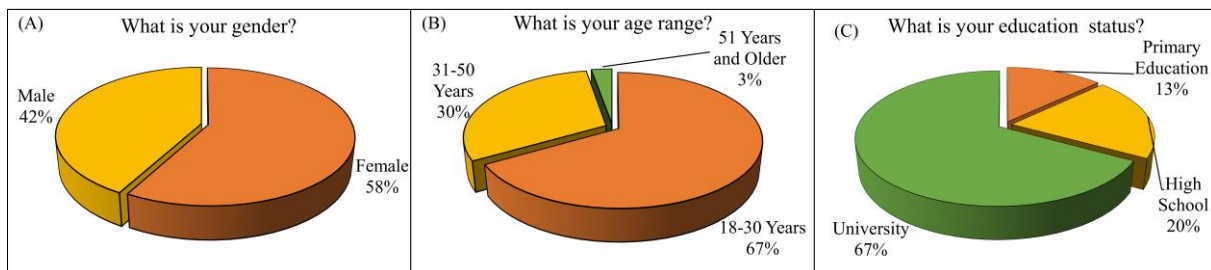


Figure 1. Demographics of the study participants.

As shown in Figure 1, 58% of the participants were female, and 42% were male. Even though the same number of male and female participants were invited, the balance between genders was slightly tilted due to the relatively low participation rate. Additionally, a significant portion of the participants were within the 18-30 age range (67%) and had a university degree (67%).

In response to the question “What type of furniture do you prefer for your home?” as shown in Figure 2A, 70% of participants preferred modern-style furniture. In contrast, the remaining participants were equally distributed among retro, custom, industrial, and other furniture design options. These results contradicted past studies, which observed a higher preference for wooden retro-style furniture [13].

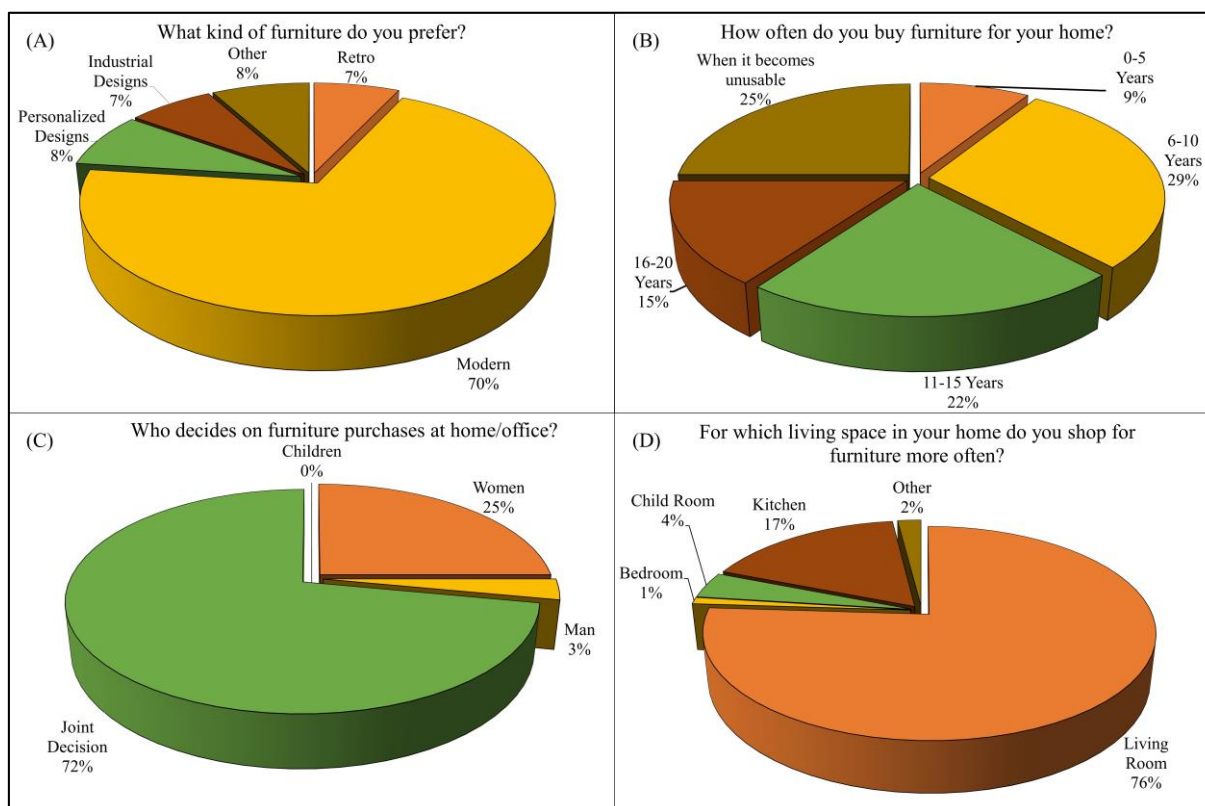


Figure 2. Distribution of Participant Preferences on (A) Furniture Type, (B) Shopping Frequency, (C) Decision Maker on Selection of the Furniture, and (D) Primary Living Space Considered for Furniture Shopping.

As shown in Figure 2B, 29% of participants reported a shopping frequency every 6-10 years, and the next 25% stated they only replaced furniture when it became unusable. 72% of the participants declared that furniture purchasing decisions for home/office are made jointly with other individuals in the home/office, as illustrated in Figure 2C. All participants reported that children do not have a significant influence on the furniture purchasing decision. This finding was contradictory to the findings of one previous study documenting the direct and indirect influence of children on purchasing decisions for various items [21, 22, 23]. Such a contradictory finding could be due to the lack of a question that explored the decision-making dynamics for specific furniture items that are directly used by children. In examining the responses of participants who did not consider furniture purchasing decisions to be joint decisions, 25% of these participants indicated that women significantly influence furniture purchasing decisions. In comparison, 3% stated that men are the final decision-makers. As shown in Figure 2D, 76% of the participants primarily consider replacing their living room furniture, followed by the next 17% who consider replacing their kitchen furniture first.

As shown in Figure 3, 93% of the survey participants prefer furniture options with average price/average performance when purchasing furniture. Only 1% of the consumers declared they would prioritize affordability even if the furniture item has a low performance. For any product, performance refers to a product’s primary operating characteristics.

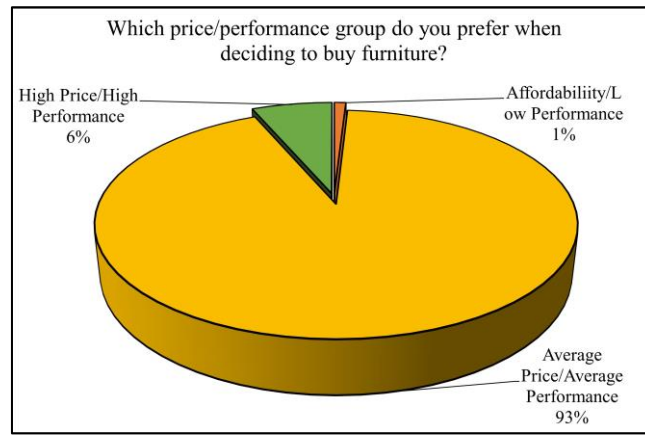


Figure 3. Distribution of Participants' Preferences Across Main Price/Performance Categories.

As shown in Figure 4A, the furniture price had a significant role in the furniture purchasing decisions of 87% of the study participants. Overall quality and design elements were also highly influential on furniture purchasing decisions based on the answers of 97.22% and 97% of participants, who voted at least “Yes,” respectively, as given in Figures 4B and 4C. Moreover, 24% of participants stated that the origin of the furniture does not influence their purchasing decisions, as illustrated in Figure 4D. Similarly, as shown in Figure 5A, 20% of participants declared that the Warranty Period does not influence their furniture purchasing decisions, whereas 13% were undecided. On the other hand, reliability was among the influential factors, as 97.22% of the participants voted at least “Yes,” as shown in Figure 5B. Color and Texture were highlighted as influential elements by 88% of the participants, while the remaining 12% were undecided or thought these elements were not that important, as shown in Figure 5C. Another notable study finding was that 21% of participants reported that the brand factor does not influence their furniture purchasing decisions, while 19% were undecided, and 59% stated that they deem the brand factor essential while shopping for furniture, as given in Figure 5D.

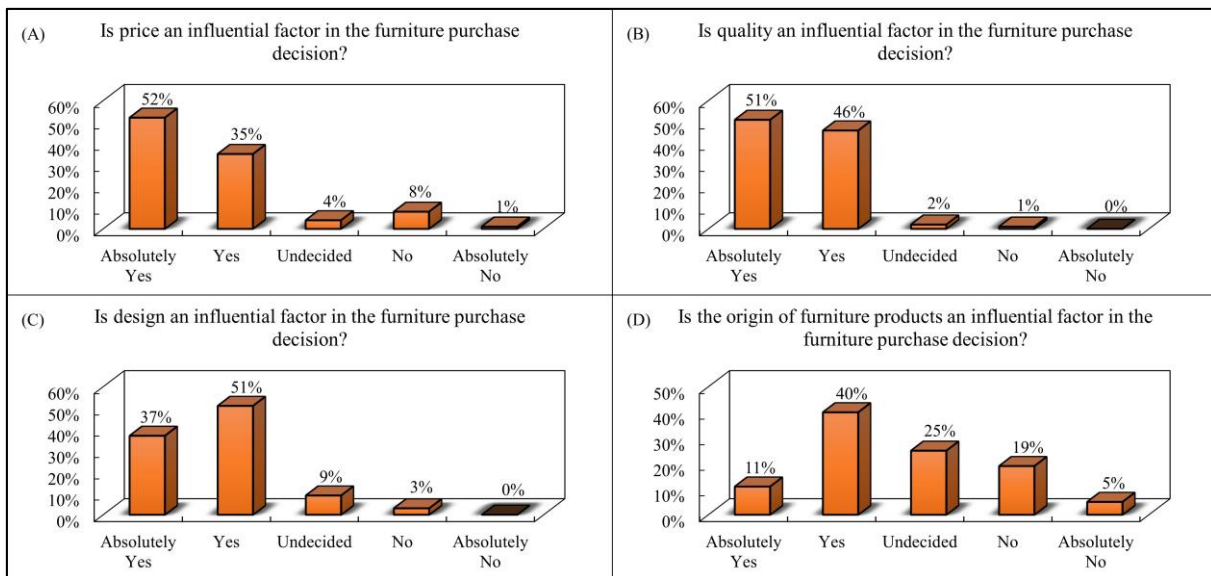


Figure 4. Consumer Preferences Regarding the Influence of the Price(A), Quality (B), Design (C), and Origin of Products (D) on Furniture Purchasing Decisions.

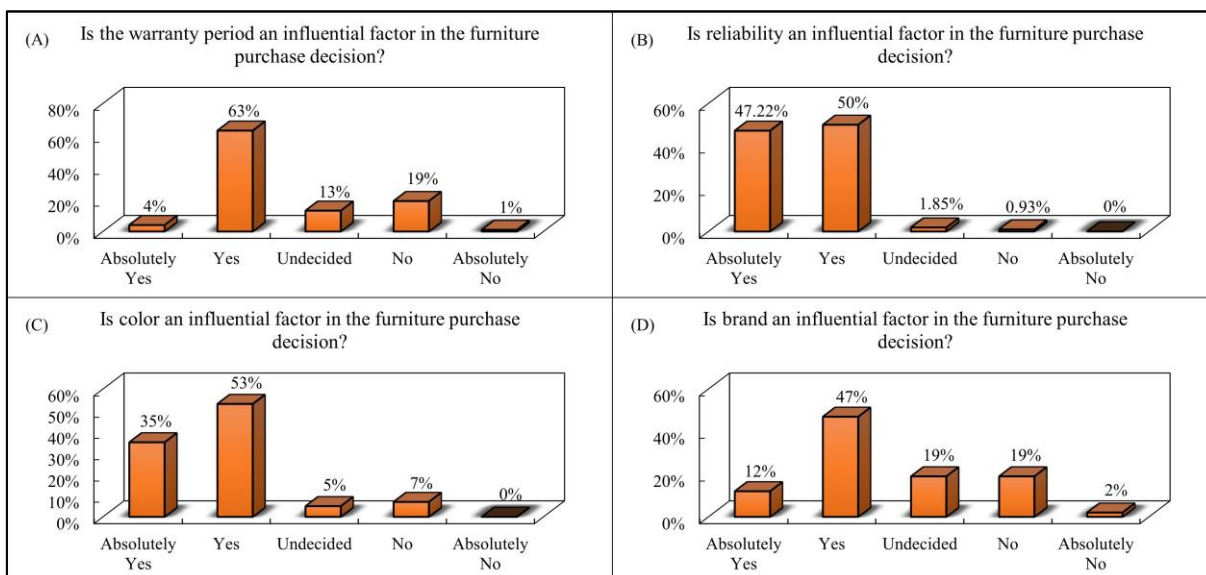


Figure 5. Consumer Preferences Regarding the Influence of (A) the Warranty Period, (B) the Reliability, (C) the Color, and (D) the Brand on Furniture Purchasing Decisions.

Furthermore, as shown in Figure 6, 32% of respondents were undecided about the influence of the product/production process’s environmental impacts on their furniture purchasing decision. 50% of the study participants stated that they consider the environmental impact of furniture products and their production processes while shopping for new furniture. In contrast, only 18% declared the environmental impact of the furniture products and production processes as non-influential. The results of this study were parallel with those of previous literature and indicated a growing preference for environmentally friendly production processes and products [3, 7, 8, 13, 14].

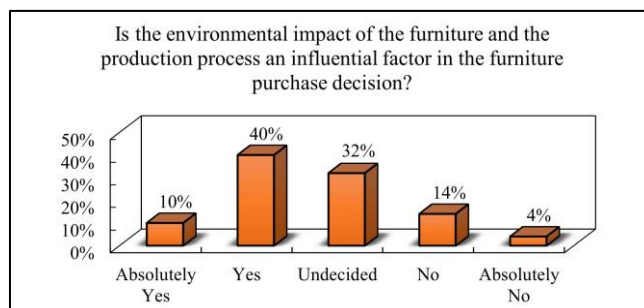


Figure 6. Consumer Preferences Regarding the Environmental Impact of Furniture and Furniture Production Process.

As for the marketing channels that are the primary information sources and trigger the consumers’ purchasing decision, according to 67.6% of consumers, stores were influential on their purchasing decision, followed by recommendations from close contacts such as family, friends, and relatives (62%) and brand’s website (46.3%), as illustrated in Figure 7. Social media marketing channels, which are trending nowadays, are also among the influential marketing outlets for 30.6% of consumers. However, only 11.1% of consumers stated that all marketing channels influence their furniture purchasing decisions. On the other hand, 3.7% of the respondents stated that no marketing channels influence them in their furniture purchasing decisions. Traditional marketing channels, such as radio and television advertisements, thought to be the most effective in common belief, have been found to influence the furniture purchasing decisions of only 4.6% of participants. Another traditional marketing channel, print media, was deemed an effective marketing tool in furniture purchasing decisions by only 0.9% of the consumer base. However, recent studies have shown that younger consumers prefer the Internet and social networks as primary marketing channels to gather information about products

and services; older consumers prefer more traditional media such as stores, recommendations from close contacts, and expert opinions [15].

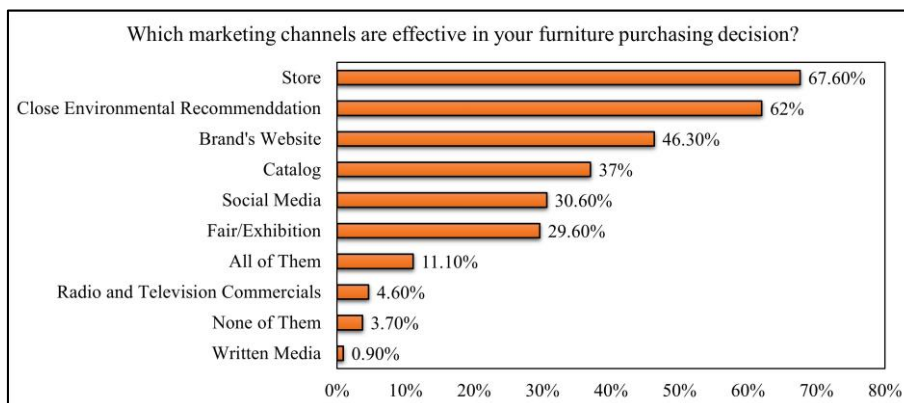


Figure 7. Marketing Channels That Are Influential on Furniture Purchasing Decisions.

Finally, consumers were asked which quality dimension they paid the most attention to while purchasing furniture this question aimed to prioritize the quality dimensions based on consumer perceptions. According to the participants, the most critical dimensions were durability and performance, highlighted by 25.93% and 20.37% of participants, respectively, as shown in Figure 8. In the literature, there is evidence that durability and performance are crucial elements of furniture design for better service life and customer experience [24]. The third and fourth most considered dimensions were reliability and serviceability, both with percentages of 12.96%. The least considered quality dimensions during furniture purchase decisions were aesthetics and features, which were mentioned by only 2.78% and 4.63% of consumers. Conformance and perceived quality dimensions made the list after serviceability with percentages of 11.11% and 9.26%, respectively.

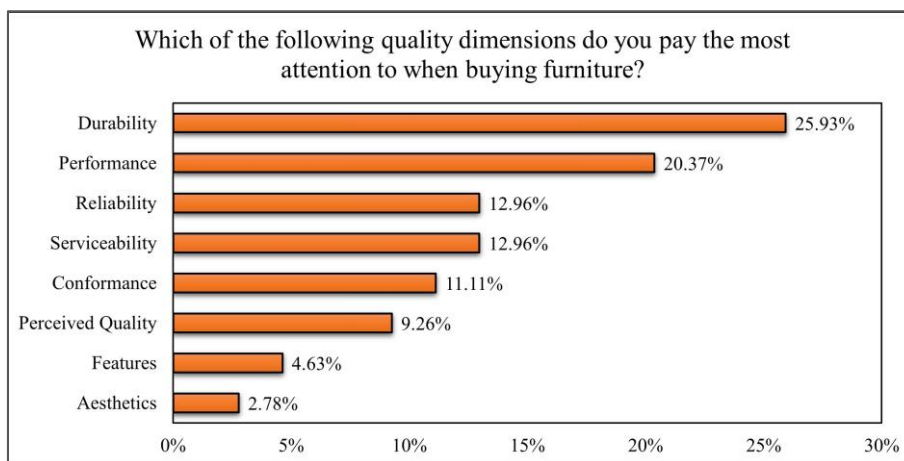


Figure 8. The Prioritization of Quality Dimensions by Consumers When Purchasing Furniture.

The findings of this study were explained in detail in the previous sections of the article. According to the survey carried out within the study, it was determined that furniture consumers predominantly prefer modern-style furniture, which was consistent with other studies in the literature. Kaputa and Supin (2010) observed that consumers mostly favored modern-style furniture [4]. Similarly, Atilgan et al. (2018) found that consumers primarily chose modern-style furniture items [10].

This research documented that price, perceived quality, design, warrant period, color and texture, brand, and reliability are all significant factors in consumers' furniture purchasing decisions. Findings of previous literature also yielded similar results. Kaputa and Supin (2010) indicated that perceived quality, price, and design were influential factors in purchasing decisions [4]. Atilgan et al. (2018) stated that affordable prices, durability, comfort, and aesthetics influenced purchasing decisions [10]. Oblak et al. (2020) achieved similar results, identifying quality, price, and additional services as influential factors in purchasing decisions [11]. However, contradictory to the findings of this study, Olšiaková et al. (2016) argued that Price was no longer an influential factor in furniture purchasing decisions [8]. Similarly, Loučanová and Olšiaková (2020) found that Price was no longer an adequate criterion in purchasing decisions and that quality was a more influential criterion [13].

Furthermore, the study results indicated that participants considered the store, recommendations from close contacts, and the brand's website the most influential marketing channels. Previous literature published by Kaputa and Supin (2010) identified stores, catalogs, and internet platforms as influential marketing channels in purchasing decisions. Since print media was not deemed significantly influential by the target consumer base of this study, previous literature findings documented by Kaputa and Supin (2010) were complementary and contradictory [4].

The study also asked, "Is the environmental impact of furniture and its production process a significant factor in purchasing decisions?" To this question, 50% of participants responded with at least "Yes." Meanwhile, 32% of respondents remained neutral. In the literature, Barčić et al. (2021) emphasized a trending perceived importance of sustainability in the wooden furniture sector [15]. Guzel (2020) demonstrated that consumers prefer wood in furniture due to its ecological and renewable properties [14]. Parallely, Palus et al. (2012) argued that wood's ecological properties, environmental friendliness, renewability, and naturalness make it preferable over non-wood materials [7]. Conversely, Kaputa et al. (2018) found that many consumers in furniture production do not consider environmental issues [3]. Varying consideration levels of consumers regarding ecological aspects of the products and production processes could be due to the regional sustainability awareness levels or the severity of the environmental issues encountered as part of consumers' personal experiences, which could trigger the development of a sense of elevated ecological responsibility.

Several managerial, practical, and academic implications could be derived from the results of this study. Managerial implications could be summarized under four main titles: Targeted Marketing Strategies, Product Development and Design, Pricing Strategy, and Customer Relationship Management. As for the first title, understanding how different demographic groups (age, gender, and education) make furniture purchasing decisions allows for more targeted and effective marketing strategies. For instance, in this study, most participants were young adults who value durability and performance more; therefore, marketing efforts can be directed toward highlighting furniture products' useful life and expected functionality. Within the product development and design scope, insights into quality dimensions valued by consumers (like durability, performance, and reliability) could effectively guide product development efforts. Furniture manufacturers might prioritize these aspects in their designs to meet consumer expectations. When it comes to pricing strategy, understanding the price sensitivity of various consumer segments can help set appropriate pricing strategies that balance quality and affordability to appeal to the target market. In addition, from the perspective of customer

relationship management, knowing the importance of serviceability and pre- and post-purchase service can lead to the development of robust customer service policies, enhancing customer satisfaction and loyalty.

Scientific implications of the study could be structured around the theme of Consumer Behavior Research. This study contributes to the academic literature on consumer behavior, particularly in the context of the furniture industry. It offers new insights or validates existing theories regarding the factors influencing furniture purchasing decisions. Moreover, the study employed a hybrid sampling methodology intending to contribute to methodological diversity in market research.

Last but not least, Practical implications of the study could be discussed within the context of Consumer Education, Industry Benchmarks, and Policy Development. The study's findings could be used to educate consumers about the importance of various quality dimensions in furniture, aiding them in making more informed purchasing decisions. The study could be used as a reference source to establish benchmarks for quality and service standards in the furniture industry, encouraging overall industry improvement. Additionally, insights from the study could contribute to informed policy decisions regarding consumer protection, fair trading, and sustainable practices in the furniture industry. Furthermore, since the study's findings highlighted a slight skewness towards sustainable products and production processes, it could be perceived as a clue to promote a greater industry focus on eco-friendly and sustainable furniture, impacting environmental conservation efforts.

Overall, this study provided valuable insights for furniture industry stakeholders, contributed to academic knowledge in consumer behavior and market research, and had practical implications for consumers, industry standards, and potentially policymaking.

4. Conclusion

This study aimed to observe the impact of demographic factors such as age, gender, and education level on consumers' furniture purchasing decisions and the influence of the eight quality dimensions on consumer purchase decisions.

- The demographic information of the survey participants shows that the majority (58%) were female, 66.67% were aged between 18 and 30, and 67% were university graduates.
- The responses to the survey questions showed that 69% of consumers preferred modern-style furniture, with the remaining participants almost equally distributed among retro, custom designs, industrial designs, and other furniture styles.
- 29% of the participants stated that they shop for furniture every 6-10 years, followed by the next 25% who shop for furniture when it becomes unusable, and 22% who renew their furniture every 11-15 years.
- 72% of consumers make furniture purchasing decisions based on consensus, and children do not influence these decisions.
- Most consumers (76%) commonly shop for living rooms.
- 92.59% of the participants prefer furniture products that come at an average price and offer average performance.
- Price, quality, design, origin of furniture products, warranty period, reliability, color, brand, the environmental impact of the furniture, and its production process all influence consumers' furniture purchasing decisions.
- Durability (25.93%) and performance (20.37%) were the most influential quality dimensions. Surprisingly, the least

considered quality dimensions were features (4.63%) and aesthetics (2.78%).

As can be interpreted from the above conclusive remarks, this study provided valuable insights for furniture designers, manufacturers, and marketing specialists about consumer purchasing behaviors, what consumers pay attention to when selecting furniture, and their preferences in furniture styles. Additionally, it has been observed that consumers, when purchasing furniture, not only consider visible factors such as Price, aesthetics, and quality but are also reasonably concerned about the environmental friendliness of the furniture itself and its production process.

When considering future research topics in this area, researchers could extend similar studies to a broader geographic area, encompassing various consumer groups at regional, national, and continental levels. Additionally, they could conduct comparative analyses of consumer preferences in furniture purchasing decisions by working with equally sized samples in different regions or cities within a country. On the other hand, this study could be extended beyond the furniture sector to address different industries that cater to end consumers. By re-evaluating consumer desires and preferences under the influence of various factors, findings could be obtained that would enable more accurate strategies to guide different sectors.

This study is expected to serve as an essential resource and reference for professionals and academics working in the fields of furniture design, production, and marketing.

References

- [1] A. H. Maslow, "A Theory of Human Motivation.," *Psychol Rev*, vol. 50, no. 4, pp. 370–396, Jul. 1943, doi: 10.1037/h0054346.
- [2] I. Akyuz, "Investigation of Psychological, Socio-Psychological and Socio-Cultural Factors Affecting Consumer Behavior in Furniture Purchasing," Institute of Science, Trabzon, 2006.
- [3] V. Kaputa, A. Pirc Barčić, H. Maťová, and D. Motik, "Consumer Preferences for Wooden Furniture in Croatia and Slovakia," *Bioresources*, vol. 13, no. 3, pp. 6280–6299, 2018, doi: 10.15376/biores.13.3.6280-6299.
- [4] V. Kaputa and M. Supin, "Consumer Preferences For Furniture," 2010. [Online]. Available: <https://www.researchgate.net/publication/288346897>
- [5] Ü. Tutar and F. Çamlıbel, "The Conceptual Dimensions of the Consumer Perception of Value Affecting Consumer Preference," *Balikesir University Faculty of Economics and Administrative Sciences Journal*, vol. 3, no. 1, pp. 47–58, 2022, Accessed: Sep. 27, 2023. [Online]. Available: <https://dergipark.org.tr/pub/bauniibfd/issue/70923/1022376>
- [6] D. Nicholls and M. Bumgardner, "Evaluating Selected Demographic Factors Related to Consumer Preferences for Furniture from Commercial and from Underutilized Species," *For Prod J*, vol. 57, no. 12, pp. 79–82, 2007, Accessed: Nov. 07, 2023. [Online]. Available: <https://www.fs.usda.gov/research/treesearch/29381>
- [7] H. Paluš, H. Maťová, and V. Kaputa, "Consumer Preferences for Joinery Products and Furniture in Slovakia and Poland," *Bioresources*, vol. 54, no. 2, pp. 123–132, 2012, doi: 10.15376/biores.13.3.6280-6299.
- [8] M. Olšiaková, E. Loučanová, and H. Paluš, "Monitoring Changes in Consumer Requirements for Wood Products in Terms of Consumer Behavior," *Acta Facultatis Xylologiae Zvolen*, vol. 58, no. 1, pp. 137–147, Jan. 2016, doi: 10.17423/afx.2016.58.1.15.

- [9] L. Oblak, A. P. Barčić, K. Klarič, M. K. Kuzman, and P. Grošelj, "Evaluation of Factors in Buying Decision Process of Furniture Consumers by Applying AHP Method," *Drvena Industrija*, vol. 68, no. 1, pp. 37–43, Mar. 2017, doi: 10.5552/drind.2017.1625.
- [10] A. Atilgan, H. Ulusoy, N. Kahraman, and H. Peker, "Consumers' Preferences for Furniture Styles and Factors that Effect in Choosing," *Journal of Bartın Faculty of Forestry*, vol. 20, no. 2, pp. 232–238, 2018, doi: 10.24011/barofd.401213.
- [11] L. Oblak, B. Glavonjić, A. Pirc Barčić, T. Bizjak Govedič, and P. Grošelj, "Preferences of Different Target Groups of Consumers in Case of Furniture Purchase," *Drvena industrija*, vol. 71, no. 1, pp. 79–87, Mar. 2020, doi: 10.5552/drvind.2020.1932.
- [12] M. Jošt, V. Kaputa, M. Nosál'ová, A. P. Barčić, I. Perić, and L. Oblak, "Changes in Customer Preferences for Furniture in Slovenia," *Drvena Industrija*, vol. 71, no. 2, pp. 149–156, Jun. 2020, doi: 10.5552/drvind.2020.1967.
- [13] E. Loučanová and M. Olšiaková, "Consumers' Perception of Retro-Innovation of Wood Products," *Acta Facultatis Xylologiae Zvolen*, vol. 62, no. 2, pp. 165–174, 2020, doi: 10.17423/afx.2020.62.2.15.
- [14] T. A. Guzel, "Consumer Attitudes toward Preference and Use of Wood, Woodenware, and Furniture: A Sample from Kayseri, Turkey," *Bioresources*, vol. 15, no. 1, pp. 28–37, 2020, doi: 10.15376/biores.15.1.28-37.
- [15] A. P. Barčić, M. K. Kuzman, T. Vergot, and P. Grošelj, "Monitoring Consumer Purchasing Behavior for Wood Furniture Before and during the COVID-19 Pandemic," *Forests*, vol. 12, no. 7, Jul. 2021, doi: 10.3390/f12070873.
- [16] B. G. Şahin and E. E. Akballı, "Consumer Behaviors of Affecting Factors and Method Analysis," *International Journal of Social and Educational Sciences*, vol. 1, no. 1, pp. 43–85, 2019, Accessed: Sep. 25, 2023. [Online]. Available: <https://dergipark.org.tr/tr/pub/usbed/issue/48285/607430>
- [17] İ. D. Bulut and E. Gultekin Tarla, "Examining Consumer Behavior From Behavioral Economics Perspective: A Comparison of Online and Traditional Shopping," *Journal of Economics and Administrative Sciences*, vol. 7, no. 1, pp. 9–30, Jun. 2023, doi: 10.33399/biibfad.1192583.
- [18] D. A. Garvin, "What does "Product Quality" Really Mean? ," *Sloan Manage Rev*, vol. 26, no. 1, pp. 25–43, 1984, Accessed: Mar. 10, 2024. [Online]. Available: http://www.oqrm.org/English/What_does_product_quality_really_means.pdf
- [19] A. C. Burns and R. F. Bush, *Marketing Research*, 7th ed. Ankara, 2015.
- [20] W. G. Cochran, *Sampling Techniques*, 3rd ed. New York: John Wiley & Sons, 1977.
- [21] E. S. Thomson, A. W. Laing, and L. McKee, "Family Purchase Decision Making: Exploring Child Influence Behaviour," *Journal of Consumer Behaviour*, vol. 6, no. 4, pp. 182–202, Jul. 2007, doi: 10.1002/cb.220.
- [22] C. Arora and S. P. Diwan, "Children Influence on Family Purchase Decisions Across Product Categories," *SN Business & Economics*, vol. 2, no. 7, p. 67, Jul. 2022, doi: 10.1007/s43546-022-00238-x.
- [23] S. D. Senevirathna, P. Wachissara Thero, and P. O. De. Silva, "A Study of Children's Influence in Family Purchasing Decisions: Parents' Perspective," *Asian Journal of Marketing Management*, vol. 1, no. 01, Jan. 2022, doi: 10.31357/ajmm.v1i01.5467.
- [24] M. Uysal, "Coefficient of Acceptability for Joints on Furniture Frame Analysis under Cyclic Loads," *Journal of Innovative Science and Engineering (JISE)*, vol. 7, no. 01, Feb. 2023, doi: 10.38088/jise.1183127.

Microencapsulation of Black Carrot Anthocyanins for Enhanced Thermal Stability

Elif Baysal ¹ , Aslihan Kazan ^{1*} 

¹ Department of Bioengineering, Bursa Technical University, 16310 Bursa, Turkey

Abstract

Pigments obtained from plants and algae are utilized as colour additives in food and pharmaceutical formulations due to the advantages of being non-toxic and possessing several biological activities. However, the low stability limits the utilization of natural pigments and therefore strategies such as chemical modification or encapsulation are required. This study aimed to improve the thermal stability of black carrot anthocyanins by microencapsulation. For this purpose, anthocyanin-rich black carrot extracts were obtained by ultrasound-assisted extraction and four different solvent systems were compared regarding extraction yield. The effect of parameters such as concentration and flow rate of alginate solution, stirring rate and temperature of CaCl₂ solution and needle diameter on the average size, polydispersity (PDI), and sphericity of alginate microparticles were examined. Optimum conditions were elicited as 2% concentration and 1 ml/min flow rate for alginate solution, 40 rpm stirring rate of CaCl₂ solution at 4°C and 0.45 mm of needle size resulting in 462.4 µm of particle size. Heat treatment was also applied and the retention efficiencies were determined as 96.92% and 75.82% for encapsulated and free anthocyanins, respectively. In addition, the half-life of anthocyanin-rich extract has been shown to increase from 7.5 h to 66.5 h by microencapsulation. These findings indicated the ability of alginate microparticles for the protection of black carrot anthocyanins from thermal degradation and improvement of storage stability.

Keywords: Alginate microparticles, Anthocyanin, Black carrot, Encapsulation, Thermal stability.

Cite this paper as:

Baysal, E., Kazan, A., (2024).
Microencapsulation of Black Carrot Anthocyanins for Enhanced Thermal Stability. Journal of Innovative Science and Engineering. 8(1): 92-102

*Corresponding author: Aslihan Kazan
E-mail: aslihan.kazan@btu.edu.tr

Received Date: 12/02/2024

Accepted Date: 22/04/2024

© Copyright 2024 by
Bursa Technical University. Available
online at <http://jise.btu.edu.tr/>



The works published in Journal of Innovative Science and Engineering (JISE) are licensed under a Creative Commons Attribution-NonCommercial 4.0 International License.

1. Introduction

Colour additives or food colorants have been utilized as an indicator for the freshness of food as well as in non-food applications such as pharmaceutical formulations [1, 2]. These compounds are categorized based on various properties and one of the most popular classifications is the division as natural and synthetic colorants. Synthetic colorants have several advantages over their natural counterparts such as high resistance to degradation by light, heat or oxygen and low cost [3, 4]. However, the use of synthetic colorants as mixtures or high consumption may cause undesirable side effects such as hypersensitivity reactions [1]. Due to these limitations, increasing health concerns and consumer demand, natural colorants are becoming more popular.

The most common natural food colorants are chlorophyll for green, carotenoids for yellow and orange, anthocyanins for red and purple colour and these colorants are obtained from plants or algae by various extraction methods. While the main objective of previous applications was their colouring feature, they attract attention nowadays due to their possible health benefiting effects [5, 6].

Anthocyanins are water-soluble pigments which are responsible for the red, blue and purple colour of fruits and vegetables, and belong to the flavonoid class of phenolic compounds. They display a great number of biological activities and health promoting benefits such as radical scavenging, antimutagenic, anti-inflammatory, antihypertensive activities and reducing the risk of cancer, diabetes, cardiovascular and neurodegenerative disorders. Although anthocyanins possess significant potential as a food colorant, they are known to be instable under heat and light exposure and pH changes, which is a limitation that needs to be overcome [7–11].

The common methods for the stability enhancement of anthocyanins are chemical modification such as acylation and encapsulation [12]. Encapsulation is a viable approach to protect active compounds from harsh environmental conditions, to enable easier handling or to provide a controlled release behaviour [13, 14]. Emulsification, gelation, liposomal encapsulation and spray-drying are widely applied encapsulation strategies that mainly utilize polysaccharides, gums and proteins as encapsulating agents [15]. The ionotropic gelation or ionic cross-linking method is based on the crosslinking of polyelectrolyte polymers such as alginate, chitosan and pectin by counter ions [16]. In particular, sodium alginate is widely utilized in food, biomedical and pharmaceutical applications. It is a linear and anionic polysaccharide composed of α -1,4-l-guluronic acid and β -1,4-d-manuronic acid units and is commercially available from brown algae [17]. It is biodegradable, biocompatible and nontoxic and has the ability to form cross-linked gel structures in the presence of divalent and multivalent cations [18].

The objective of this study was to improve the thermal stability of black carrot anthocyanins by encapsulation. For this purpose, black carrot anthocyanins were obtained by ultrasound-assisted extraction by using water and ethanol at different concentrations. Alginate microparticles were prepared by ionotropic gelation method and the effects of parameters such as alginate concentration, flow rate of alginate solution, stirring rate and temperature of CaCl_2 solution and needle diameter were examined. Heat treatment was also applied to free and encapsulated anthocyanins to determine the influence of encapsulation on thermal stability. Thus, the effect of alginate based microencapsulation on the thermal stability of anthocyanin-rich black carrot extracts obtained by ultrasound-assisted extraction was determined.

2. Materials and Methods

2.1. Plant Material

Black carrots were purchased from a local market. They were washed with tap water, sliced into small pieces and stored at -20°C until extraction experiments. Sodium alginate was from Tito. Calcium chloride, potassium chloride, sodium acetate and citric acid were purchased from Merck. Ethanol and methanol were from Honeywell.

2.2. Ultrasound-assisted Extraction of Black Carrot Anthocyanins

Anthocyanin extraction was carried out by ultrasound-assisted extraction method. Ultrasound-assisted extraction is one of the modern extraction techniques which overcome the limitations of laborious and time-consuming conventional extraction approaches and is extensively used in food and pharmaceutical industries. In ultrasound-assisted extraction, mass transfer is enhanced by high shear forces and acoustic-induced cavitation in liquid medium [19, 20]. Consequently, enhanced yield and extract quality, lower energy and solvent consumption and reduced extraction time were obtained compared to conventional extraction techniques. In addition, ultrasound-assisted extraction is favourable for efficient extraction of thermally unstable compounds for which low or unsatisfactory yields are achieved by conventional methods [21–23].

In this study, sliced black carrots were weighed and mixed with extraction solvent (100% (v/v) water, 30% (v/v) ethanol, 70% (v/v) ethanol, 100% (v/v) ethanol) at a constant solid:liquid ratio of 1:20. An ultrasonic bath (Weightlab Instruments, Türkiye) with 40 kHz of frequency and 80 W of ultrasonic power was used and extraction experiments were conducted at 40°C for 40 min of extraction duration. After the extraction, samples were filtered through a filter paper. All experiments were done in triplicate.

2.3. Determination of Anthocyanin Content

The anthocyanin content of extracts was determined by the spectrophotometric pH differential method [24]. This method is based on the reversible transformation of anthocyanin structure at different pH values. Anthocyanin molecules are pigmented at pH 1 while neutralized and become colorless at pH 4.5. The concentration of anthocyanin is proportional to the absorbance difference at $\lambda_{\text{vis-max}}$ (510 nm) and calculated by using the molar extinction coefficient and molecular weight of the major anthocyanin the sample [25, 26]. Briefly, two dilutions of samples were prepared by 0.025 M potassium chloride and 0.4 M sodium acetate solutions for the pH adjustment of samples to pH 1 and pH 4.5, respectively. The absorbance of obtained dilutions was measured at 510 and 700 nm wavelengths and, monomeric and total anthocyanin contents were calculated as cyanidin-3-glucoside equivalent by the following equations:

$$\text{Monomeric anthocyanins } \left(\frac{\text{mg}}{\text{L}} \right) = \frac{A \times MW \times DF \times 1000}{\epsilon \times l} \quad (1)$$

$$A = (A_{510} - A_{700})_{\text{pH}=1} - (A_{510} - A_{700})_{\text{pH}=4.5} \quad (2)$$

$$\text{Total anthocyanins } \left(\frac{\text{mg}}{\text{L}} \right) = \frac{A' \times MW \times DF \times 1000}{\epsilon \times l} \quad (3)$$

$$A' = (A_{510} - A_{700})_{\text{pH}=1} \quad (4)$$

where DF is dilution factor, MW is molecular weight (449.2 g/mol), l is optical path length and ϵ is extinction coefficient for cyanidin-3-glucoside which is equal to $26900 \text{ L mol}^{-1} \text{ cm}^{-1}$.

2.4. Preparation of Alginate Microparticles

Alginate microparticles were prepared by the ionotropic gelation method [27]. Briefly, alginate solutions at two different concentrations (1% and 2%) were prepared by dissolving sodium alginate in distilled water overnight at room temperature. The obtained alginate solution was pumped through a needle by a syringe pump (NE-300, New Era Instruments, USA) into 2% (w/v) CaCl_2 solution and prepared microparticles were kept in CaCl_2 solution for 45 min under continuous stirring. Then, alginate microparticles were removed by filtration, rinsed with distilled water and dried at room temperature for 72 h prior to size measurement. Experiments were carried out to determine the effect of parameters such as alginate concentration, flow rate of alginate solution, temperature and stirring speed of CaCl_2 solution and the needle size on the size, size distribution and sphericity of alginate particles as shown in Table 1. For all experiments, CaCl_2 concentration, dripping distance (5 cm) and volumetric ratio of alginate and CaCl_2 solutions (1:10) were kept constant.

Table 1: Experimental conditions for the preparation of alginate microparticles.

Exp. No	Alginate solution		CaCl_2 Solution		Needle
	Concentration	Flow rate	Stirring rate	Temperature	Size
1	1%	1 ml/min	40 rpm	24°C	0.8 mm
2	1%	1 ml/min	80 rpm	24°C	0.8 mm
3	2%	1 ml/min	40 rpm	24°C	0.8 mm
4	2%	1 ml/min	80 rpm	24°C	0.8 mm
5	1%	3 ml/min	40 rpm	24°C	0.8 mm
6	2%	3 ml/min	40 rpm	24°C	0.8 mm
7	1%	3 ml/min	40 rpm	4°C	0.8 mm
8	2%	3 ml/min	40 rpm	4°C	0.8 mm
9	2%	1 ml/min	40 rpm	4°C	0.45 mm
10	2%	3 ml/min	40 rpm	4°C	0.45 mm

2.5. Measurement of microparticle size, sphericity and polydispersity index

Randomly selected alginate microparticles were examined and images were taken by light microscopy. Average particle size was determined by ImageJ software [28] and polydispersity index (PDI) [29] was calculated by equation (5):

$$PDI = \left(\frac{\sigma}{d}\right)^2 \quad (5)$$

where σ is standard deviation and d is mean particle diameter.

The shape of produced microparticles was characterized by sphericity factor (SF) [30] and sphericity coefficient (SC) [31] as dimensionless shape indicators. The equations (6) and (7) were used to calculate SF and SC, respectively.

$$\text{Sphericity factor} = \frac{(d_{max} - d_{min})}{(d_{max} + d_{min})} \quad (6)$$

$$\text{Sphericity coefficient} = \frac{d_{min}}{d_{max}} \quad (7)$$

In equations (6) and (7), d_{\max} is the maximum (length) and d_{\min} is the minimum (width) diameters of particles. Microparticles with $SF < 0.05$ and SC close to 1 were considered as spheres.

2.6. Encapsulation of Black Carrot Anthocyanins in Alginate Microparticles

Encapsulation of black carrot extract was conducted by two different methods as in situ and post loading. In the first method, black carrot extract was mixed with alginate solution and the obtained mixture was added dropwise to the CaCl_2 solution under optimum conditions determined in the previous step. After the preparation, anthocyanin loaded alginate microparticles were removed by filtration and the pH differential method was applied to the remaining solution to determine the encapsulation efficiency. In the post loading method, encapsulation was carried out by absorption after the preparation of microparticles. Prepared alginate microparticles were immersed in an extract solution and left agitation for 3 h at room temperature. At the end of 3 h, the amount of unloaded anthocyanin was determined by the pH differential method. The following equation was used to calculate encapsulation efficiency [32].

$$\text{Encapsulation efficiency (\%)} = \frac{\text{Initial anthocyanin amount} - \text{Unloaded anthocyanin amount}}{\text{Initial anthocyanin amount}} \times 100 \quad (8)$$

2.7. Comparison of Thermal Stability of Free and Encapsulated Black Carrot Anthocyanins

Free and encapsulated black carrot extracts were immersed in a water bath at 70°C during 3 h and the anthocyanin content of samples was determined by the pH differential method. Free and encapsulated extracts stored at 4°C were used as controls. Thermal stability of black carrot extract was evaluated by calculation of retention efficiency as follows (Equation 9) [33].

$$\text{Retention efficiency (\%)} = \frac{\text{Anthocyanin content after storage at } 70^\circ\text{C}}{\text{Anthocyanin content after storage at } 4^\circ\text{C}} \times 100 \quad (9)$$

To determine the storage behavior, reaction constant (k) and half-life ($t_{1/2}$) were calculated for free and encapsulated black carrot anthocyanins by following equations (Equations 10 and 11) [34]:

$$\ln\left(\frac{C_t}{C_0}\right) = -kt \quad (10)$$

$$t_{1/2} = -\frac{\ln 0.5}{k} \quad (11)$$

where C_0 is the initial anthocyanin content, C_t is the anthocyanin content at the specific time, t is the time and k is the reaction constant.

2.8. Statistical Analysis

The paired Student's t -test was used and the normality of the data was analyzed by the Kolmogorov-Smirnov test. In all tests, significant differences were considered when $p < 0.05$ [35].

3. Results and Discussion

3.1. Ultrasound-assisted Extraction of Black Carrot Anthocyanins

Ultrasound-assisted extraction was applied to black carrot and, anthocyanin content of extracts obtained by four different extraction solvents namely water, ethanol, 30% (v/v) EtOH and 70% (v/v) EtOH were determined by pH differential method. Extraction with 100% (v/v) water yielded the lowest anthocyanin content (46.5 mg/L) which was followed by 100% (v/v) ethanol (47.4 mg/L) with an insignificant difference. As shown in Figure 1, using an ethanol-water mixture as an extraction solvent significantly improved the amount of extracted anthocyanin compared to the experiments in which pure solvents were used. EtOH of 70% (v/v) that yields 112.7 mg/L of anthocyanin content has been chosen as an extraction solvent and black carrot extract obtained by 70% (v/v) EtOH has been used for further encapsulation and thermal stability experiments.

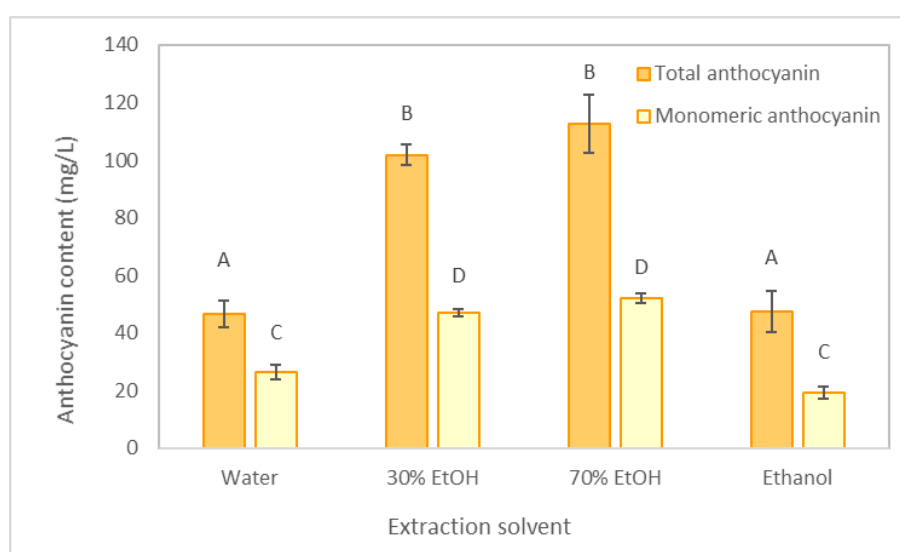


Figure 1. Anthocyanin content of black carrot extracts obtained by different solvents.

3.2. Preparation of Alginate Microparticles

Alginate microparticles were prepared by ionotropic gelation and calculated average microparticle sizes were present in Table 2.

Table 2: Average diameter, polydispersity index (PDI), sphericity factor (SF) and sphericity coefficients (SC) of prepared alginate microparticles.

Exp. No	Diameter (μm)	PDI	SF	SC
1	541.2	0.109	0.178	0.717
2	679.8	0.045	0.168	0.704
3	776.2	0.084	0.075	0.861
4	742.7	0.070	0.299	0.546
5	612.9	0.016	0.177	0.709
6	628.2	0.021	0.131	0.775
7	601.2	0.032	0.384	0.467
8	648.6	0.005	0.150	0.746
9	462.4	0.010	0.094	0.846
10	507.3	0.004	0.150	0.726

The effect of alginate concentration on average particle size, PDI value and sphericity was tested for 1% (w/v) and 2% (w/v) concentrations. For a needle diameter of 0.8 mm, increased alginate concentration resulted in the formation of larger particles probably due to the rise of viscosity by increased polymer concentration which may lead to the formation of larger particles [31]. Stirring of the gelation bath is applied to prevent the aggregation of beads and to obtain a more homogenous cross-linking reaction. However, increased stirring rate creates strong centrifugal forces and may lead to the deformation of particle shape [36]. In accordance with this, lower CaCl_2 stirring rate resulted in the production of microparticles with higher sphericity at constant alginate concentration (Figure 2A and 2B). Therefore, further experiments were conducted at 40 rpm stirring rate of the CaCl_2 bath. At a 40 rpm stirring rate, lower alginate concentration resulted in the production of microparticles with higher PDI value and lower sphericity that indicated the benefit of higher alginate concentration to produce spherical microparticles with narrow size distribution. When the alginate droplet enters the gelation solution, the drag forces acting on the droplet lead to shape deformation. It has been reported that alginate solution with low concentration and viscosity creates droplets less resistant to shape change while higher alginate concentration makes a huge contribution to retaining the spherical shape of the droplets [37]. The flow rate of alginate solution was also found to have a significant impact on sphericity and PDI value rather than average particle size. For 1% (w/v) alginate concentration, an increased flow rate mainly affected the PDI value of produced microparticles (decreasing from 0.109 to 0.016) while at 2% (w/v) alginate concentration, a higher flow rate tended to produce microparticles with less sphericity. To determine the effect of the temperature of the CaCl_2 solution, microparticle production was conducted at 4°C and 24°C. For 2% (w/v) alginate concentration, CaCl_2 solution at 4°C resulted in the production of particles with narrow size distribution while its effect on particle size and sphericity was insignificant. Smrdel et al., prepared alginate beads by ionotropic gelation and the temperature of gelation bath has been shown to be ineffective on particle size while the higher gelation temperature improved particle sphericity [38]. In addition, shape and size distribution of alginate microparticles tended to be irregular with increased stirring rate of CaCl_2 solution. By changing the needle diameter from 0.8 mm to 0.45 mm, a huge decrease was obtained for average particle size while the obtained particles were more spherical in shape and had a lower PDI value (Figure 2C). Since the average particle size, size distribution and sphericity have a significant impact on the release behavior, they are of prime importance for the application of particles. For instance, the reduction of particle size results in an increased surface area to volume ratio and leads to overcoming mass transfer limitations while tear shaped microparticles possess a strong burst release profile for the encapsulated agent. Furthermore, the mechanical and chemical features of microparticles are significantly affected by particle sphericity. Spherical beads have been shown to possess higher mechanical strength compared to non-spherical counterparts [29, 31, 39]. Consequentially, 2% (w/v) concentration and 1 ml/min flow rate for alginate solution, 40 rpm stirring rate of CaCl_2 solution at 4°C and 0.45 mm of needle size were found to be the most appropriate conditions for the production of alginate microparticles with lower size, narrow size distribution and higher sphericity.

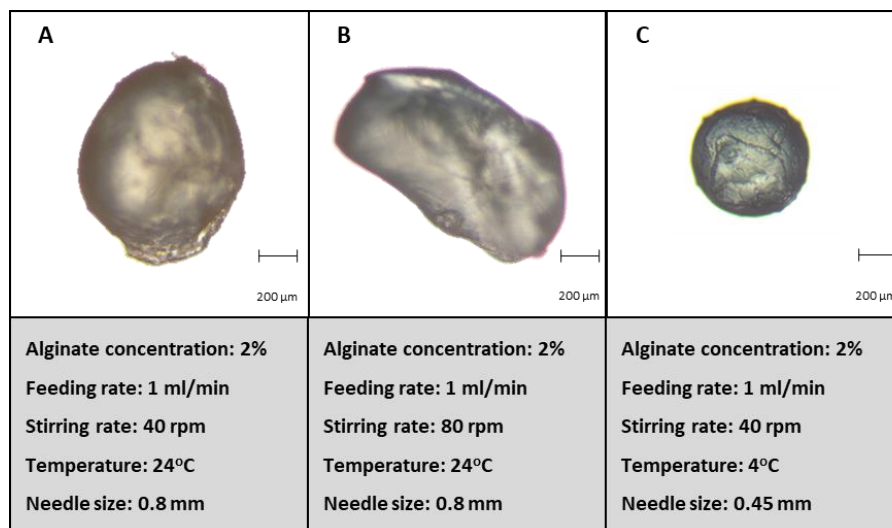


Figure 2. Optical microscope images of randomly selected alginates microparticles prepared at different conditions.

3.3. Encapsulation of Black Carrot Anthocyanins in Alginate Microparticles

Encapsulation of black carrot extract was conducted by two different methods as in situ and post loading, and both approaches were compared in terms of encapsulation efficiency. For the first method, 70.8% of initial anthocyanin was encapsulated during particle formation. However, absorption based encapsulation approach resulted in a significantly higher encapsulation efficiency as 87.7%. In previous studies, anthocyanin-rich extract from haskap berries was encapsulated in calcium-alginate microparticles with an encapsulation efficiency of 68.03% [40] while the encapsulation efficiencies of hibiscus anthocyanins by dripping extrusion were reported to vary between 67.9 and 88.1% [41] which are in agreement with the obtained encapsulation efficiencies in our study. A higher encapsulation efficiency was obtained by post loading method which is probable due the release of extract into the gelation bath during in situ loading. Therefore, post loading was chosen as the encapsulation approach of anthocyanins in alginate microparticles.

3.4. Comparison of Thermal Stability of Free and Encapsulated Black Carrot Anthocyanins

Free and encapsulated black carrot extracts were incubated at 4°C and 70°C and anthocyanin content of samples was compared to control groups to determine the thermal stability. After exposure to 70°C for 3 h, the retention efficiencies were determined as 96.92% and 75.82% and degradation constants were 0.092 h⁻¹ and 0.0104 h⁻¹ for free and encapsulated anthocyanins, respectively. In addition, the half-life of anthocyanin rich extract was improved from 7.5 h to 66.5 h by encapsulation. These results elicited the ability of alginate microparticles for the protection of black carrot anthocyanins from thermal degradation and improvement of storage stability.

4. Conclusion

The color and stability of anthocyanin change during processing and storage of foods and, various encapsulation approaches are applied for the protection of these compounds from harsh environmental conditions. In this study, black carrot anthocyanins were obtained by ultrasonic-assisted extraction and encapsulated to enhance thermal stability. For this purpose, alginate microparticles were produced at different conditions and characterized in terms of average particle size, particle sphericity and PDI values. Optimum conditions for the production of alginate

microparticles with lower size, higher sphericity and narrower size distribution were elicited as 2% (w/v) alginate concentration, 1 ml/min flow rate, 4°C CaCl₂ temperature, 40 rpm stirring rate and 0.45 mm needle diameter resulting in particle size of 462.4 µm, sphericity factor of 0.094 and PDI of 0.01. Thermal stability tests were also conducted and the obtained results revealed that half-life of encapsulated anthocyanins was significantly higher than its free form. In conclusion, this study suggests that encapsulation of black carrot anthocyanins in alginate microparticles improved their thermal stability and possessed a high potential to be utilized as an ingredient for food applications.

References

- [1] Amchova, P., Kotolova, H. and Ruda-Kucerova, J. (2015). Health safety issues of synthetic food colorants. *Regulatory Toxicology and Pharmacology*, 73(3):914–922.
- [2] Sigurdson, G.T., Tang, P. and Giusti, M.M. (2017). Natural Colorants: Food Colorants from Natural Sources. *Annual Review of Food Science and Technology*, 8(1):261–280.
- [3] El-Wahab, H.M.F.A., Moram, G.S.E.-D. (2013). Toxic effects of some synthetic food colorants and/or flavor additives on male rats. *Toxicology and Industrial Health*, 29(2):224–232.
- [4] Bakowska-Barczak, A. (2005). Acylated Anthocyanins as Stable Natural Food Colorants – a Review. *Polish Journal of Food and Nutrition Sciences*, 1455(2):107–116.
- [5] Rodriguez-Amaya, D. B. (2019). Natural Food Pigments and Colorants, Bioactive Molecules in Food, Edited by Jean-Michel Mérillon and Kishan Gopal Ramawat, *Springer International Publishing*, pp. 867–901. ISBN: 978-3-319-78030-6.
- [6] Coultate, T. and Blackburn, R. S. (2018). Food colorants: their past, present and future. *Coloration Technology*, 134(3):165–186.
- [7] Akhtar, S., Rauf, A., Imran, M., Qamar, M., Riaz, M. and Mubarak M. S. (2017). Black carrot (*Daucus carota* L.), dietary and health promoting perspectives of its polyphenols: A review. *Trends Food Science & Technology*, 66:36–47.
- [8] Kong, J.M., Chia, L. S., Goh, N.K., Chia, T.F. and Brouillard R. (2003). Analysis and biological activities of anthocyanins. *Phytochemistry*, 64(5):923–933.
- [9] Netzel, M., Netzel, G., Kammerer, D.R., Schieber, A., Carle, R., Simons, L., Bitsch, I., Bitsch, R. and Konczak, I. (2007). Cancer cell antiproliferation activity and metabolism of black carrot anthocyanins. *Innovative Food Science & Emerging Technologies*, 8(3):365–372.
- [10] Khandare, V., Walia, S., Singh, M. and Kaur, C. (2011). Black carrot (*Daucus carota* ssp. *sativus*) juice: Processing effects on antioxidant composition and color. *Food and Bioprocess Processing*, 89(4):482–486.
- [11] Konczak, I. and Zhang W. (2004). Anthocyanins-More Than Nature's Colours. *Journal of Biomedicine and Biotechnology*, 2004(5):239–240.
- [12] Fang, J.L., Luo, Y., Yuan, K., Guo, Y. and Jin, S.H. (2020). Preparation and evaluation of an encapsulated anthocyanin complex for enhancing the stability of anthocyanin. *LWT*, 117:108543.
- [13] Robert, P. and Fredes, C. (2015). The Encapsulation of Anthocyanins from Berry-Type Fruits. Trends in Foods. *Molecules*, 20(4):5875–5888.
- [14] Yousuf, B., Gul, K., Wani, A. A. and Singh, P. (2016). Health Benefits of Anthocyanins and Their Encapsulation for Potential Use in Food Systems: A Review. *Critical Reviews in Food Science and Nutrition*, 56(13):2223–2230.

- [15] Tan, C., Dadmohammadi, Y., Lee, M. C., & Abbaspourrad, A. (2021). Combination of copigmentation and encapsulation strategies for the synergistic stabilization of anthocyanins. *Comprehensive Reviews in Food Science and Food Safety*, 20(4), 3164-3191.
- [16] Patel, M.A., AbouGhaly, M.H.H., Schryer-Praga, J.V. and Chadwick, K. (2017). The effect of ionotropic gelation residence time on alginate cross-linking and properties. *Carbohydrate Polymers*, 155:362–371.
- [17] Agüero, L., Zaldivar-Silva, D., Peña, L. and Dias, M. (2017). Alginate microparticles as oral colon drug delivery device: A review. *Carbohydrate Polymers*, 168:32–43.
- [18] Łętocha, A., Miastkowska, M. and Sikora, E. (2022). Preparation and Characteristics of Alginate Microparticles for Food. *Pharmaceutical and Cosmetic Applications Polymers*, 14(18):3834.
- [19] Vilku, K., Mawson, R., Simons, L. and Bates, D. (2008). Applications and opportunities for ultrasound assisted extraction in the food industry — A review. *Innovative Food Science & Emerging Technologies*, 9(2):161–169.
- [20] Esclapez, M.D., García-Pérez, J.V., Mulet, A. and Cárcel, J.A. (2011). Ultrasound-Assisted Extraction of Natural Products. *Food Engineering Reviews*, 3(2):108–120.
- [21] Picó, Y. (2013). Ultrasound-assisted extraction for food and environmental samples. *TrAC Trends in Analytical Chemistry*, 43:84–99.
- [22] Rutkowska, M., Namieśnik, J. and Konieczka P. (2017). Ultrasound-Assisted Extraction, The Application of Green Solvents Separation Processes, Edited by Francisco Pena-Pereira and Marek Tobiszewski, *Elsevier*, pp. 301–324. ISBN: 978-0-12-805297-6.
- [23] Chemat, F., Rombaut, N., Sicaire, A.G., Meullemiestre, A., Fabiano-Tixier, A.S. and Abert-Vian, M. (2017). Ultrasound assisted extraction of food and natural products. Mechanisms, techniques, combinations, protocols and applications. A review. *Ultrasonics Sonochemistry*, 34:540–560.
- [24] Kazan, A., Sevimli-Gur, C., Yesil-Celiktas, O. and Dunford, N.T. (2016). Investigating anthocyanin contents and in vitro tumor suppression properties of blueberry extracts prepared by various processes. *European Food Research and Technology*, 242(5):693–701.
- [25] Lee, J., Durst, R.W. and Wrolstad, R.E. (2005). Determination of Total Monomeric Anthocyanin Pigment Content of Fruit Juices, Beverages, Natural Colorants, and Wines by the pH Differential Method: Collaborative Study. *Dietary Supplements*, 88(5):1269-1278.
- [26] Taghavi, T., Patel, H. and Rafie, R. (2021). Comparing pH differential and methanol-based methods for anthocyanin assessments of strawberries. *Food Science and Nutrition*, 10(7):2123-2131.
- [27] Leong, J.Y., Lam, W.H., Ho, K.W., Voo, W.P., Fu-Xiang Lee, M., Lim, H.P., Lim, S.L., Tey, B.T., Poncelet, D. and Chan, E.S. (2016). Advances in fabricating spherical alginate hydrogels with controlled particle designs by ionotropic gelation as encapsulation systems. *Particuology*, 24:44-60.
- [28] Schneider, C.A., Rasband, W.S. and Eliceiri, K.W. (2012). NIH Image to ImageJ: 25 years of image analysis. *Nature Methods*, 9(7):671–675.
- [29] Raval, N., Maheshwari, R., Kalyane, D., Youngren-Ortiz, S.R., Chougule, M.B. and Tekade, R.K. (2018). Importance of physicochemical characterization of nanoparticles in pharmaceutical product development, Basic Fundamentals of Drug Delivery, Edited by Rakesh Kumar Tekade, *Elsevier Inc.*, pp.369-400. ISBN: 9780128179093.
- [30] Alkhatib, H., Doolaanea, A.A., Assadpour, E., Mohamad Sabere, A.S., Mohamed, F. and Jafari, S.M. (2022). Optimizing the encapsulation of black seed oil into alginate beads by ionic gelation. *Journal of Food Engineering*, 328:111065.

- [31] Partovinia, A. and Vatankhah, E. (2019). Experimental investigation into size and sphericity of alginate microbeads produced by electrospraying technique: Operational condition optimization. *Carbohydrate Polymers*, 209:389–399.
- [32] Rashid, F., Albayati, M. and Dodou, K. (2023). Novel Crosslinked HA Hydrogel Films for the Immediate Release of Active Ingredients. *Cosmetics*, 10(1):6.
- [33] Baysal, E. (2022). İyonik Jelasyon Yöntemi ile Kara Havuç Antosiyaninlerinin Mikroenkapsülasyonu, Bachelor Thesis. *Bursa Technical University*, Bursa. 26p.
- [34] Patel, A.S., Kar, A. and Mohapatra, D. (2020). Development of microencapsulated anthocyanin-rich powder using soy protein isolate, jackfruit seed starch and an emulsifier (NBRE-15) as encapsulating materials. *Scientific Reports*, 10(1):10198.
- [35] Kazan, A. and Demirci, F. (2023). Olive leaf extract incorporated chitosan films for active food packaging. *Konya Journal of Engineering Sciences*, 11(4):1061-1072.
- [36] Lee, B.B., Ravindra, P. and Chan, E.S. (2013). Size and shape of calcium alginate beads produced by extrusion dripping. *Chemical Engineering and Technology*, 36(10):1627-1642.
- [37] Lim, G.P., Lee, B.B., Ahmad, M.S., Singh, H. and Ravindra, P. (2016). Influence of process variables and formulation composition on sphericity and diameter of Ca-alginate-chitosan liquid core capsule prepared by extrusion dripping method. *Particulate Science and Technology*, 34(6):681-690.
- [38] Smrdel, P., Bogataj, M. And Mrhar, A. (2008). The influence of selected parameters on the size and shape of alginate beads prepared by ionotropic gelation. *Scientia Pharmaceutica*, 76(1):77-89.
- [39] Zhang, W. and He, X. (2009). Encapsulation of living cells in small (approximately 100 microm) alginate microcapsules by electrostatic spraying: a parametric study. *Journal of Biomechanical Engineering*, 131(7):74515.
- [40] Celli, G.B., Ghanem, A. and Brooks, S.L. (2016). Optimized encapsulation of anthocyanin-rich extract from haskap berries (*Lonicera caerulea* L.) in calcium-alginate microparticles. *Journal of Berry Research*, 6:1–11.
- [41] De Moura, S.C.S.R., Berling, C.L., Germer, S.P.M., Alvim, I.D. and Hubinger, M.D. (2018). Encapsulating anthocyanins from *Hibiscus sabdariffa* L. calyces by ionic gelation: Pigment stability during storage of microparticles. *Food Chemistry*, 241:317-327.

Redox Properties of Poly (aniline boronic acid) in Aqueous Environment with Glucose and Table Sugar Addition

Taha Yasin Eken^{1*} , Deniz Uzunsoy¹ , Omer Yunus Gumus² 

¹ Bursa Technical University, Metallurgical and Materials Engineering, 16310 Bursa, Türkiye

² Bursa Technical University, Polymer Materials Engineering, 16310 Bursa, Türkiye

Cite this paper as:

Eken, T., Y., Uzunsoy, D., Gumus, O., Y., (2024). *Redox Properties of Poly (aniline boronic acid) in Aqueous Environment with Glucose and Table Sugar Addition*. Journal of Innovative Science and Engineering. 8(1): 103-114

*Corresponding author: Taha Yasin Eken
E-mail: yasin.eken@btu.edu.tr

Received Date: 29/12/2023

Accepted Date: 29/03/2024

© Copyright 2024 by

Bursa Technical University. Available
online at <http://jise.btu.edu.tr/>



The works published in Journal of Innovative Science and Engineering (JISE) are licensed under a Creative Commons Attribution-NonCommercial 4.0 International License.

Abstract

Polyaniline boronic acid, a conducting polymer with unique properties, has gained attention for its potential applications in flow batteries, sensors, drug delivery systems, and electrochemical devices. Understanding the redox behavior of this polymer in the presence of sugars is of particular interest due to the potential implications for its functionality in various applications. Cyclic voltammetry is employed to analyze the redox behavior of the polymer in aqueous solutions with glucose and table sugar. Preliminary results suggest that the presence of glucose increase and table sugar decrease the peak values. The diffusion coefficient of the polymer is found as $2.6 \times 10^{-9} \text{ cm}^2/\text{s}$. The choice of supporting electrolyte, exemplified by potassium carbonate and potassium chloride, also exhibited an influence on redox behavior of polyaniline boronic acid, and peak potential and peak values are higher in potassium chloride solutions.

Keywords: Redox, Cyclic voltammetry, Flow batteries, Polyaniline boronic acid, Glucose, Table sugar

1. Introduction

Redox active materials are significant due to their pivotal role in many electrochemical processes, enabling efficient electron exchange and facilitating redox reactions. These materials are essential elements in various applications, such as energy storage systems, catalysis, sensors, and electronic devices [1, 2]. Their ability to undergo reversible changes in oxidation states makes them valuable for storing and releasing energy, enabling the development of high-performance batteries and supercapacitors. Moreover, redox active materials find significance in the design of catalysts for promoting chemical transformations and in the creation of sensors for detecting analytes in various fields. The fundamental redox properties of these materials contribute to their versatility and make them indispensable in advancing technologies that rely on efficient electron transfer mechanisms [3, 4].

The ability of conductive polymers to transfer electrons, driven by their redox properties [5, 6] remains a hot debate among researchers. These materials have a conjugated backbone with alternate single and double bonds. There are many examples of these types of conductive polymers such as polyaniline (PANI), polypyrrole (PPY) and poly(3,4-ethylenedioxythiophene) (PEDOT). It is this group of conductive polymers that can control the surface charge on the basis of their high conductivity. They are used in many applications including redox flow batteries, skin tissue engineering, wound treatment, high-performance supercapacitors besides antibacterial and antioxidant uses. This implies that they have diverse applications where changing the electrical charge on their surfaces is necessary [7].

Polyaniline boronic acid (PABA) is a conductive polymer that exhibits a distinctive blend of electrical conductivity and redox responsiveness [8–10]. This characteristic renders it a highly attractive option for novel technologies and multipurpose devices. PABA has attractive uses in a variety of industries, such as electrochemical devices, drug delivery systems, and sensors. One of PABA's most interesting features is its redox behavior, which is essential to its operation. Gaining insight into PABA's interactions with redox-active species—especially those found in aqueous environments—is essential to realizing its potential in a range of biological and technological applications [7, 11–17].

PABA's potential applications range from glucose biosensors to drug delivery systems for controlled release, highlighting the importance of understanding its redox behavior in the context of these applications [18]. PABA can also serve as electroactive components in energy storage devices, such as supercapacitors and batteries, where their redox processes are instrumental in storing and delivering electrical energy. An in-depth understanding of the redox behavior of PABA can thus have implications beyond the realms of sensors and drug delivery systems, extending into the domain of sustainable energy storage and conversion [19].

In previous studies, electrochemical tests of PABA polymer in various environments were performed [7, 12, 13, 15, 20, 21]. However, since the studies were generally related to sensors, the graphite electrode was coated with PABA, and then their performance was tested with different salt structures in acidic environments [21].

There were no CV tests performed with PABA in aqueous solutions according to the literature. Hence, in this study, it was aimed to prepare the solution of PABA polymer in aqueous media and subject it to CV tests and to guide

future studies based on its behavior. Additionally, in order to increase solubility, the CV behavior of PABA was tested with additives such as glucose and table sugar [19, 21, 22, 16], which were previously used in the literature. It was observed that the solubility of PABA is high in a basic environment and its half-wave peak potential is very low, while in an acidic environment, both solubility and peak potential are low. Therefore, the solution was prepared in a neutral environment.

2. Materials and Methods

2.1. Materials

3-Aminophenylboronic acid monohydrate (98 %) and Potassium Iodate (KIO_3) were obtained from Thermo Fisher Scientific Chemicals. Hydrochloric Acid (37 %, ACS reagent) was obtained from Fluka. Nitrogen gas was obtained from Asalgaz company. All electrodes were obtained from CH Instruments Inc. (Austin, Texas, USA). Glucose powder (chemical grade) was obtained from Sigma Aldrich. Typical market sugar is used as sugar addition. Potassium Carbonate (K_2CO_3) was obtained from AGC chemicals. Potassium chloride was obtained from Sigma Aldrich.

2.2. Electrochemical Studies

The main electrochemical method used to examine the redox characteristics of polyaniline boronic acid (PABA) in an aqueous environment was cyclic voltammetry (CV), with particular focus on how PABA interacts with glucose and table sugar solutions. Three electrode systems were used with a CHI608E model from CH Instruments, and CHI608E Electrochemical Analyzer software was used for the electrochemical tests. A schematic representation of three-electrode system is shown in Figure 1. The EIS and CV methodologies were applied. At scan rates from 5 to 500 mV/s, the electrodes' cyclic voltammetric behaviors were examined in aqueous solutions of 1 M KCl, and 1 M K_2CO_3 to establish the intended ionic environment. Potential range of the cell was between -1.2 to +0.8 V. Ag/AgCl and Platinum electrodes served as the reference and counter electrodes, while glassy carbon electrodes with a surface area of 0.7069 cm^2 served as the working electrodes. The CV testing involved the purging of N_2 gas. We conducted the experiments at room temperature. PABA, glucose, and table sugar were carefully dissolved in high-purity deionized water (DI water) to create solutions. Current-voltage profiles that showed PABA's redox activity in the presence of glucose and sugar solutions were the data gathered during the CV tests. By analyzing these profiles, peak potentials, peak currents, and electrochemical pathways were found, which shed light on how the addition of sugar affected the redox characteristics of PABA.

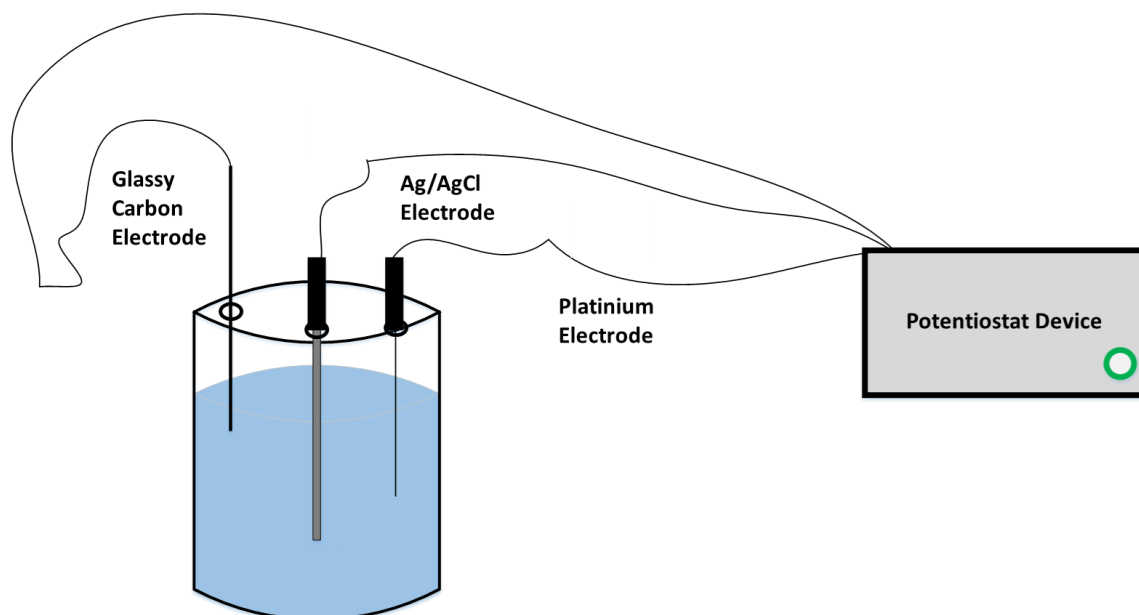


Figure 1. 3-electrode electrochemical cell system setup is schemetically shown. Working electrode is glassy carbon electrode, reference electrode is Ag/AgCl electrode and counter electrode is Platinum electrode.

2.3. Synthesis of PABA

The synthesis procedure utilized in our study had been employed in a prior investigation [23]. KIO_3 was used to start the synthesis of polyaniline boronic acid (PABA). Hydrochloric acid (HCl) was used as the dopant to improve solubility and aid in the polymerization process. A nitrogen atmosphere was used for the polymerization process. The reaction mixture was kept in an ice bath for a full day while the polymerization was taking place. During this time, there was a noticeable shift in color—the solution became a shade of purple. The successful polymerization of ABA into polyaniline boronic acid (PABA) is characterized by this color change. Following the completion of the polymerization procedure, contaminants and unreacted ABA were removed from PABA by precipitation and subsequent filtration. PABA was acquired with a substantial yield of 80% and to eliminate any remaining solvents, the purified PABA was vacuum-dried, producing a high-purity polymer. The chemical structure and purity of the synthesized PABA were verified via analytical technique: Fourier-transform infrared spectroscopy (FTIR). These investigations confirmed that PABA was successfully formed and guaranteed that it would be suitable for further electrochemical experiments.

3. Results

FTIR results for the monomers aniline boronic acid (ABA) and its polymer, PABA, are presented in Figures 2a and 2b. In the FTIR spectrum of PABA, a broad absorption at 3263 cm^{-1} indicates O-H stretching, and a peak at 1180 cm^{-1} suggests C-O stretching. Additionally, absorptions at 3460 cm^{-1} and 3380 cm^{-1} correspond to -NH stretching vibrations of ABA. During polymerization, we see absorption peaks, which move to higher wavenumbers, indicating that PABA has formed as expected, just like previous studies have shown [19, 24, 23].

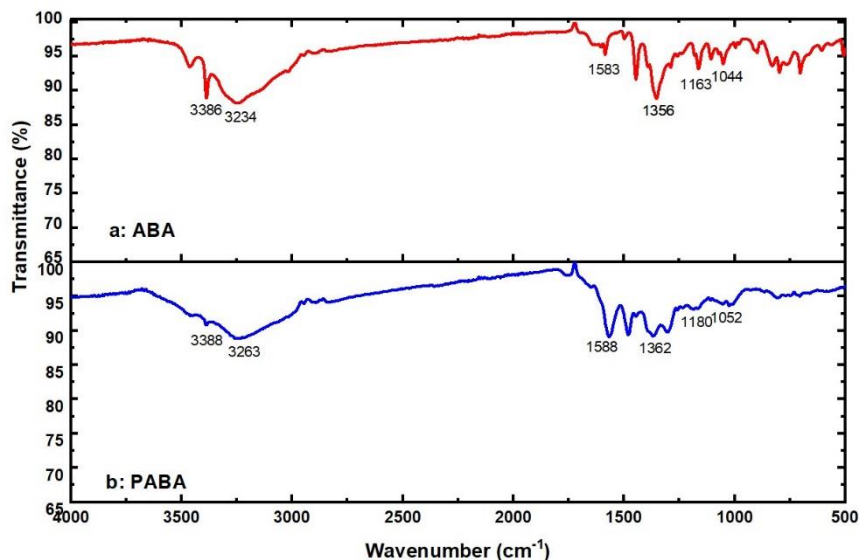


Figure 2. FTIR results of (a) ABA and (b) PABA polymers.

The electrochemical studies conducted to examine the redox characteristics of PABA in an aqueous solution with the addition of glucose, and table sugar solutions offer important insights into how PABA behaves when these redox-active species are present.

The redox activity of PABA was shown by CV experiments. In the absence of glucose and sugar solutions in Figure 3, two redox peaks—which represent the PABA oxidation and reduction processes—were seen in 1 M K_2CO_3 . The standard hydrogen electrode (S.H.E.) is used as a potential parameter in this study. The oxidation peak voltage is -0.112 V, and the reduction peak voltage is -0.625 V for 500 mV/s scanning rate and half-wave potential is -0.368.5 V. The oxidation of PABA (0) to PABA(I) and the reduction of PABA(I) to PABA (0) were represented by the anodic and cathodic peaks that were obtained in the cyclic voltammograms, respectively. In Figure 4, oxidation and reduction peak points of each scan rate (5 mV/s, 20 mV/s, 100 mV/, 250 mV/s, and 500 mV/s) of Figure 3 were used. It shows the CV peak current versus square root of scan rate linear fit graph. According to this graph and using the Randles-Ševčík equation,

$$i_p = (2.69 \times 10^5)n^{3/2}AC(Dv)^{0.5} \quad (1)$$

the peak current (i_p) is determined by various factors, such as the number of moles of electrons transported in the reaction (n), the electrode's surface area (A), the concentration of the analyte in units of mol/cm³ (C), the diffusion coefficient (D), and the scan rate of the applied voltage (v). The n value is taken as 1 for the number of electron transfer, A is taken as 0.07 cm², and concentration is taken as 0.000001 M, and the slope of the reduction side is 0.00217 which is equal to $\frac{i_p}{v^{0.5}}$. After calculations, the diffusion coefficient of 1 mM PABA in 1 M K_2CO_3 is found as 2.6×10^{-9} cm²/s. The observed value appears to be relatively low when compared to other polymers that exhibit good solubility in aqueous environments. For instance, Poly(N-vinylbenzyl phthalimide-co-TEGSt) demonstrates a value of 2.33×10^{-7} cm²/s [25]. Nevertheless, the low diffusible nature of polymers makes PABA a viable candidate for such experiments.

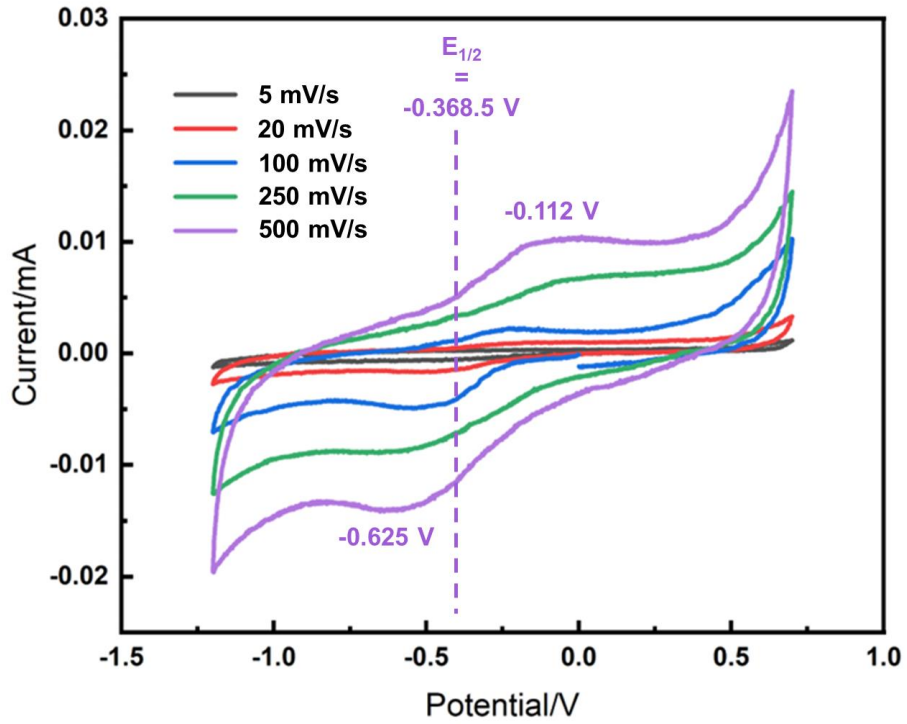


Figure 3. Cyclic voltammetry of 1 mM PABA with 1 M K₂CO₃.

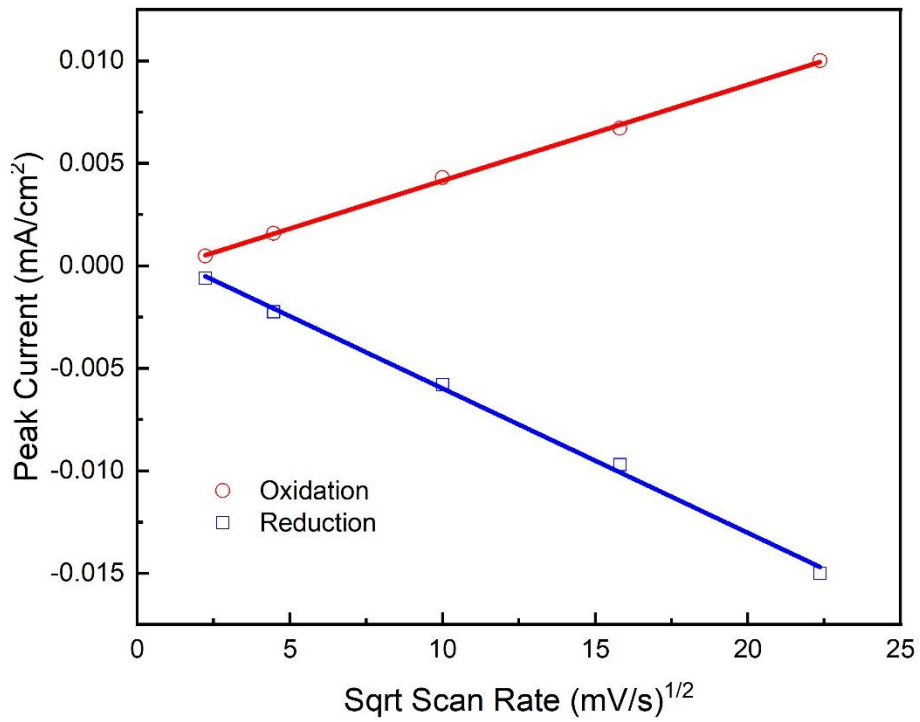


Figure 4. CV peak current versus square root of scan rate linear fit graph for oxidation and reduction peak currents of Figure 3, which shows 1 mM PABA with 1 M K₂CO₃.

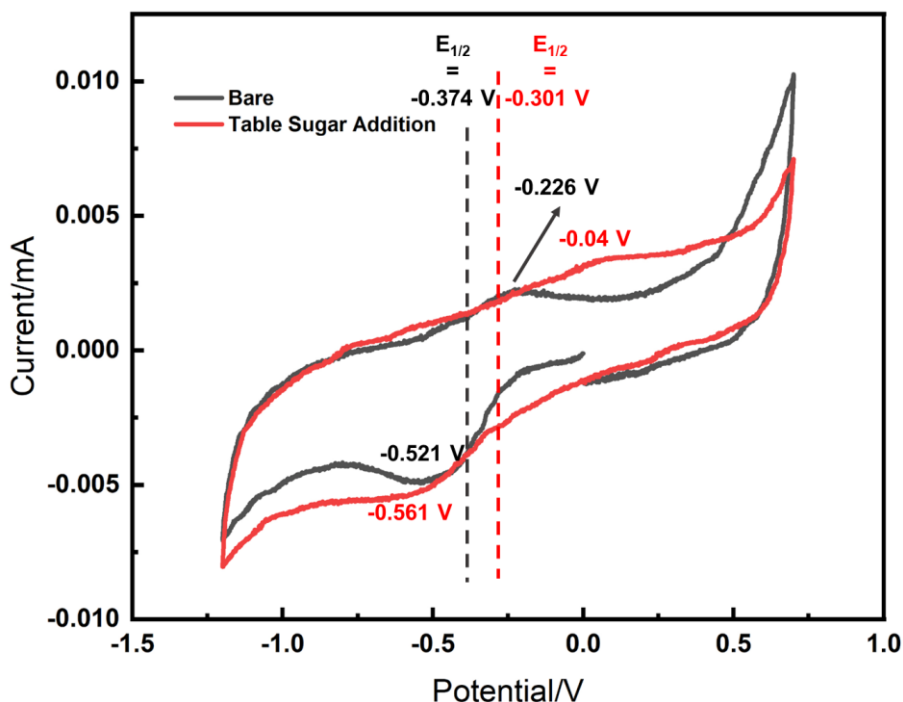


Figure 5. Cyclic voltammetry of 1 mM PABA with 1 M K_2CO_3 with addition of 1 mM table sugar, scan rate is 100 mV/s.

The effect of table sugar is shown in Figure 5. The redox behavior of PABA was negatively affected by the addition of table sugar to the aqueous environment in 1 M K_2CO_3 . The redox peaks become lower, and the half-wave potential decreases after addition. However, the area between the peaks increases, so the area between peaks in a CV curve can be related to the overall capacity. The influence of table sugar on the redox behavior of PABA in a 1 M K_2CO_3 aqueous environment was negative, as evidenced by a reduction in redox peaks and a decrease in the half-wave potential upon addition. Despite these changes, the area between the peaks in a cyclic voltammetry (CV) curve increased, suggesting a potential relationship to the overall capacity.

In some instances, the addition of glucose led to an increase in peak currents and a slight shift in peak potentials (Figure 6(a)). This enhancement in redox activity is attributed to the interaction between glucose and PABA, which can facilitate electron transfer processes and promote the conversion between the leucoemeraldine and emeraldine oxidation states. The degree of enhancement varied with glucose concentration, with higher concentrations generally resulting in more pronounced effects [12, 26, 27].

On the contrary, specific sugar additions, notably sucrose and lactose, demonstrated a contrasting impact by diminishing peak currents and modifying peak potentials. The inclusion of these sugars introduced steric hindrance, influencing the kinetics of electron transfer, and resulting in the suppression of the redox activity of PABA. The extent of this suppression was found to be directly related to the concentration of sugars [28, 29].

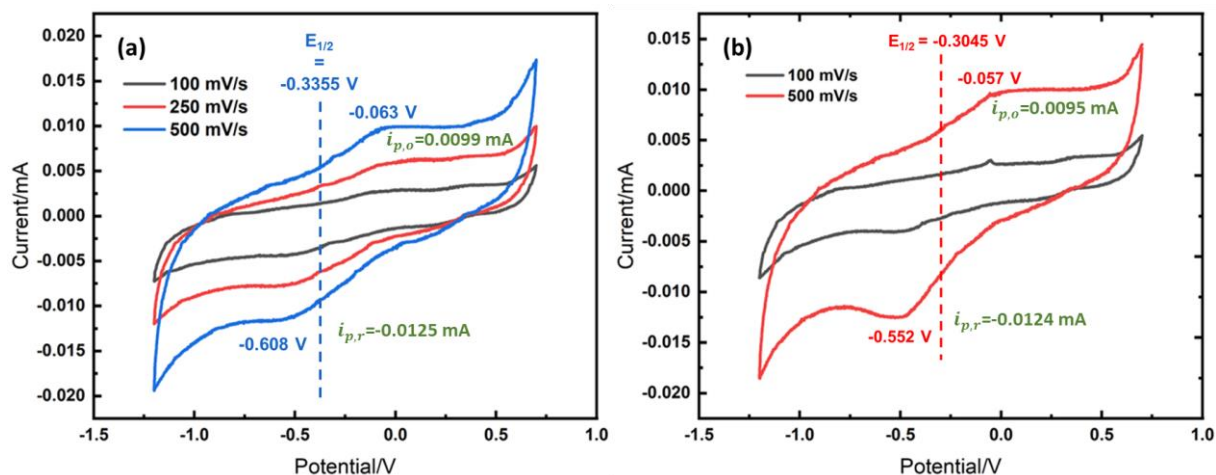


Figure 6. Cyclic voltammetry of 1 mM PABA with (a) 1 M KCl, (b) 1 M KCl and 1 M K_2CO_3 with the addition of 1 mM glucose.

To determine the impact of K_2CO_3 on PABA in comparison to KCl, an investigation was conducted, and the results are presented in Figure 6(b). The solution of Figure 6(b) was carefully prepared by mixing 1 M KCl and 1 M K_2CO_3 in distilled water as the solvent. To observe the clear difference between these solutions, Figure 7 shows the 100 mV/s scan rate CV comparison. PABA polymer can dissolve in basic solutions easily, but the reduction and oxidation points become invisible. Visible peaks can be observed in acidic conditions mostly, but in acidic conditions there were no solubility. Hence, neutral conditions would mostly be ideal for aqueous PABA solutions. In this study, to increase the pH value of KCl solution, 1 M K_2CO_3 solution had been added as drops (2 drops equal to 0.1 mL) to observe the effect of pH. There is a visible drop in both peak voltage and peak current, as evidenced by the significant difference in the half-wave potential. This variation indicates a distinct influence of the choice of supporting electrolyte on the redox behavior of PABA. The shift in peak potential and reduction in peak current suggest altered electrochemical kinetics and charge transfer processes, presenting the sensitivity of PABA to the nature of the supporting electrolyte. Further analyses and comparisons with alternative electrolytes will contribute to a comprehensive understanding of the factors influencing the redox behavior of PABA in different environments, aiding in the design and customization of PABA-based materials for specific electrochemical applications.

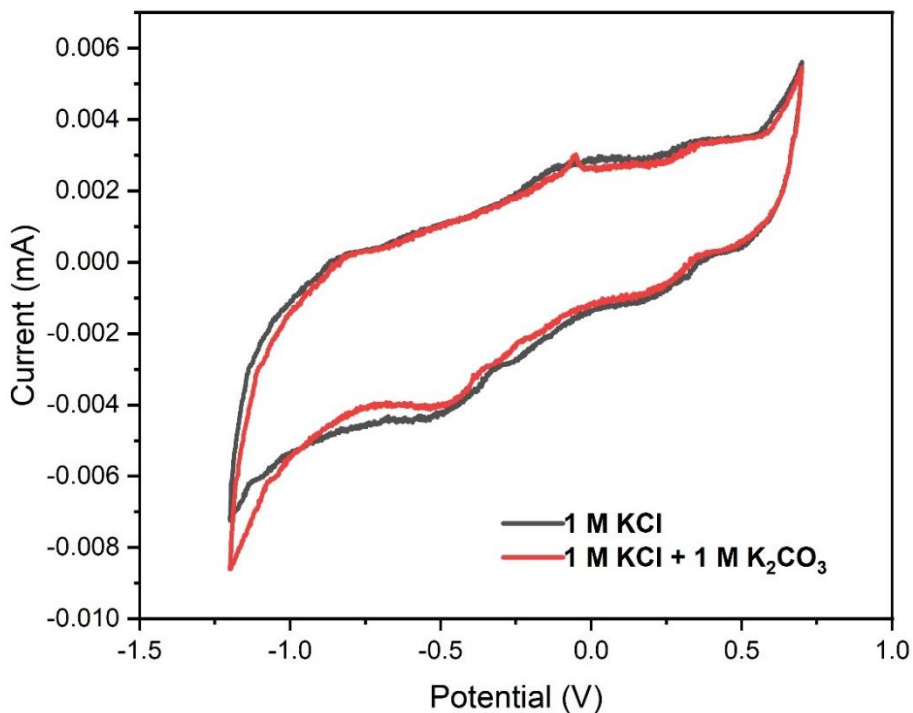


Figure 7. Cyclic voltammetry of 1 mM PABA with 1 M KCl, 1 M KCl and 1 M K_2CO_3 with the addition of 1 mM glucose, scan rate is 100 mV/s.

4. Conclusion

In conclusion, this study investigated the redox properties of polyaniline boronic acid (PABA) in an aqueous environment with a focus on its interaction with glucose and table sugar additions. Cyclic voltammetry experiments provided valuable insights into the electrochemical behavior of PABA, shedding light on its potential applications in batteries, sensors, drug delivery systems, and other electrochemical devices. The research revealed that the redox behavior of PABA was influenced by the addition of sugar species. The presence of glucose led to an enhancement in redox activity, manifested by increased peak currents and a slight shift in peak potentials. This enhancement was attributed to the facilitation of electron transfer processes and the promotion of conversion between the leucoemeraldine and emeraldine oxidation states of PABA. The degree of enhancement varied with glucose concentration, emphasizing the importance of understanding the concentration-dependent effects on PABA's redox behavior.

In contrast, the addition of particular sugars, had an inhibitory impact on the redox activity of PABA. The suppression observed was marked by reduced peak currents and altered peak potentials, which can be attributed to steric hindrance affecting the kinetics of electron transfer. Furthermore, the choice of supporting electrolyte was found to significantly impact the redox behavior of PABA. A notable drop in both peak voltage and peak current was observed when using K_2CO_3 compared to KCl, indicating the sensitivity of PABA to the nature of the supporting electrolyte. These findings provide a foundation for tailoring PABA's redox behavior for specific applications, including biosensors, drug delivery systems, and energy storage devices. Further investigations into the effects of different electrolytes and concentrations will enhance the versatility of PABA-based materials in diverse electrochemical applications.

5. Acknowledgements

This research was facilitated through the support of project code 210D005 from the Bursa Technical University Coordinatorship of Scientific Research Projects. The authors express their appreciation and gratitude.

6. References

- [1] Nguyen, T.; Montemor, M. F. (2017). Redox active materials for metal compound based hybrid electrochemical energy storage: a perspective view, *Applied Surface Science*, Vol. 422, 492–497. doi:10.1016/j.apsusc.2017.06.008
- [2] Lee, S.; Hong, J.; Kang, K. (2020). Redox-Active Organic Compounds for Future Sustainable Energy Storage System, *Advanced Energy Materials*, Vol. 10, No. 30, 2001445. doi:10.1002/aenm.202001445
- [3] Hernández, G.; Işık, M.; Mantione, D.; Pendashteh, A.; Navalpotro, P.; Shanmukaraj, D.; Marcilla, R.; Mecerreyes, D. (2017). Redox-active poly(ionic liquid)s as active materials for energy storage applications, *Journal of Materials Chemistry A*, Vol. 5, No. 31, 16231–16240. doi:10.1039/C6TA10056B
- [4] Burgess, M.; Moore, J. S.; Rodríguez-López, J. (2016). Redox Active Polymers as Soluble Nanomaterials for Energy Storage, *Accounts of Chemical Research*, Vol. 49, No. 11, 2649–2657. doi:10.1021/acs.accounts.6b00341
- [5] Winsberg, J.; Hagemann, T.; Janoschka, T.; Hager, M. D.; Schubert, U. S. (2017). Redox-Flow Batteries: From Metals to Organic Redox-Active Materials, *Angewandte Chemie International Edition*, Vol. 56, No. 3, 686–711. doi:10.1002/anie.201604925
- [6] Lai, Y. Y.; Li, X.; Zhu, Y. (2020). Polymeric Active Materials for Redox Flow Battery Application, *ACS Applied Polymer Materials*, Vol. 2, No. 2, 113–128. doi:10.1021/acsapm.9b00864
- [7] Jayeoye, T. J.; Eze, F. N.; Singh, S.; Olatunde, O. O.; Benjakul, S.; Rujiralai, T. (2021). Synthesis of gold nanoparticles/polyaniline boronic acid/sodium alginate aqueous nanocomposite based on chemical oxidative polymerization for biological applications, *International Journal of Biological Macromolecules*, Vol. 179, 196–205. doi:10.1016/j.ijbiomac.2021.02.199
- [8] Recksiedler, C. L.; Deore, B. A.; Freund, M. S. (2005). Substitution and Condensation Reactions with Poly(anilineboronic acid): Reactivity and Characterization of Thin Films, *Langmuir*, Vol. 21, No. 8, 3670–3674. doi:10.1021/la047195z
- [9] Huang, F.; Zhu, B.; Zhang, H.; Gao, Y.; Ding, C.; Tan, H.; Li, J. (2019). A glassy carbon electrode modified with molecularly imprinted poly(aniline boronic acid) coated onto carbon nanotubes for potentiometric sensing of sialic acid, *Microchimica Acta*, Vol. 186, No. 5, 270. doi:10.1007/s00604-019-3387-8
- [10] Moraes, I. R.; Kalbáč, M.; Dmitrieva, E.; Dunsch, L. (2011). Charging of Self-Doped Poly(Anilineboronic Acid) Films Studied by in Situ ESR/UV/Vis/NIR Spectroelectrochemistry and ex Situ FTIR Spectroscopy, *ChemPhysChem*, Vol. 12, No. 16, 2920–2924. doi:10.1002/cphc.201100567
- [11] Deore, B.; Freund, M. S. (2003). Saccharide imprinting of poly(aniline boronic acid) in the presence of fluoride, *Analyst*, Vol. 128, No. 6, 803–806. doi:10.1039/B300629H
- [12] Deore, B. A.; Hachey, S.; Freund, M. S. (2004). Electroactivity of Electrochemically Synthesized Poly(Aniline Boronic Acid) as a Function of pH: Role of Self-Doping, *Chemistry of Materials*, Vol. 16, No. 8, 1427–1432. doi:10.1021/cm035296x
- [13] Kalkan, Z.; Yence, M.; Turk, F.; Bektas, T. U.; Ozturk, S.; Surdem, S.; Yildirim-Tirgil, N. (2022). Boronic Acid Substituted Polyaniline Based Enzymatic Biosensor System for Catechol Detection, *Electroanalysis*, Vol. 34, No. 1, 33–42. doi:10.1002/elan.202100271

- [14] Yu, I.; Deore, B. A.; Recksiedler, C. L.; Corkery, T. C.; Abd-El-Aziz, A. S.; Freund, M. S. (2005). Thermal Stability of High Molecular Weight Self-Doped Poly(anilineboronic acid), *Macromolecules*, Vol. 38, No. 24, 10022–10026. doi:10.1021/ma0513158
- [15] Zhou, Y.; Dong, H.; Liu, L.; Liu, J.; Xu, M. (2014). A novel potentiometric sensor based on a poly(anilineboronic acid)/graphene modified electrode for probing sialic acid through boronic acid-diol recognition, *Biosensors and Bioelectronics*, Vol. 60, 231–236. doi:10.1016/j.bios.2014.04.012
- [16] Li, G.; Li, Y.; Peng, H.; Chen, K. (2011). Synthesis of Poly(anilineboronic acid) Nanofibers for Electrochemical Detection of Glucose, *Macromolecular Rapid Communications*, Vol. 32, No. 15, 1195–1199. doi:10.1002/marc.201100232
- [17] Li, J.; Zhang, N.; Sun, Q.; Bai, Z.; Zheng, J. (2016). Electrochemical sensor for dopamine based on imprinted silica matrix-poly(aniline boronic acid) hybrid as recognition element, *Talanta*, Vol. 159, 379–386. doi:10.1016/j.talanta.2016.06.048
- [18] Deore, B. A.; Freund, M. S. (2009). Self-Doped Polyaniline Nanoparticle Dispersions Based on Boronic Acid–Phosphate Complexation, *Macromolecules*, Vol. 42, No. 1, 164–168. doi:10.1021/ma8020344
- [19] Shoji, E.; Freund, M. S. (2002). Potentiometric Saccharide Detection Based on the pKa Changes of Poly(aniline boronic acid), *Journal of the American Chemical Society*, Vol. 124, No. 42, 12486–12493. doi:10.1021/ja0267371
- [20] Gu, L.; Jiang, X.; Liang, Y.; Zhou, T.; Shi, G. (2013). Double recognition of dopamine based on a boronic acid functionalized poly(aniline-co-anthranilic acid)–molecularly imprinted polymer composite, *Analyst*, Vol. 138, No. 18, 5461–5469. doi:10.1039/C3AN00845B
- [21] Li, J.; Liu, L.; Wang, P.; Zheng, J. (2014). Potentiometric Detection of Saccharides Based on Highly Ordered Poly(aniline boronic acid) Nanotubes, *Electrochimica Acta*, Vol. 121, 369–375. doi:10.1016/j.electacta.2013.12.162
- [22] Ma, Y.; Li, N.; Yang, C.; Yang, X. (2005). One-step synthesis of water-soluble gold nanoparticles/polyaniline composite and its application in glucose sensing, *Colloids and Surfaces A: Physicochemical and Engineering Aspects*, Vol. 269, No. 1, 1–6. doi:10.1016/j.colsurfa.2005.04.030
- [23] Gumus, O. Y.; Ozkan, S.; Unal, H. I. (2016). A Comparative Study on Electrokinetic Properties of Boronic Acid Derivative Polymers in Aqueous and Nonaqueous Media, *Macromolecular Chemistry and Physics*, Vol. 217, No. 12, 1411–1421. doi:10.1002/macp.201500524
- [24] Zhou, W.; Yao, N.; Yao, G.; Deng, C.; Zhang, X.; Yang, P. (2008). Facile synthesis of aminophenylboronic acid-functionalized magnetic nanoparticles for selective separation of glycopeptides and glycoproteins, *Chemical Communications*, No. 43, 5577–5579. doi:10.1039/B808800D
- [25] Winsberg, J.; Benndorf, S.; Wild, A.; Hager, M. D.; Schubert, U. S. (2018). Synthesis and Characterization of a Phthalimide-Containing Redox-Active Polymer for High-Voltage Polymer-Based Redox-Flow Batteries, *Macromolecular Chemistry and Physics*, Vol. 219, No. 4, 1700267. doi:10.1002/macp.201700267
- [26] Patil, R. C.; Patil, S. F.; Mulla, I. S.; Vijayamohan, K. (2000). Effect of protonation media on chemically and electrochemically synthesized polyaniline, *Polymer International*, Vol. 49, No. 2, 189–196. doi:10.1002/(SICI)1097-0126(200002)49:2<189::AID-PI325>3.0.CO;2-9
- [27] Komkova, M. A.; Valeev, R. G.; Kolyagin, Y. G.; Andreev, E. A.; Beltukov, A. N.; Nikitina, V. N.; Yatsimirsky, A. K.; Karyakin, A. A.; Eliseev, A. A. (2022). Solid-state survey of boronate-substituted polyaniline: on the mechanism of conductivity, electroactivity, and interactions with polyols, *Materials Today Chemistry*, Vol. 26, 101070. doi:10.1016/j.mtchem.2022.101070

- [28] Aytaç, S.; Kuralay, F.; Boyacı, İ. H.; Unaleroglu, C. (2011). A novel polypyrrole–phenylboronic acid based electrochemical saccharide sensor, *Sensors and Actuators B: Chemical*, Vol. 160, No. 1, 405–411. doi:10.1016/j.snb.2011.07.069
- [29] Brooks, W. L. A.; Sumerlin, B. S. (2016). Synthesis and Applications of Boronic Acid-Containing Polymers: From Materials to Medicine, *Chemical Reviews*, Vol. 116, No. 3, 1375–1397. doi:10.1021/acs.chemrev.5b00300